Miniaturized Low-Power and Energy-Efficient RF Wireless Communication and Sensing Systems

by

Li-Xuan Chuo

A dissertation submitted in partial fulfillment
of the requirements for the degree of
Doctor of Philosophy
(Electrical and Computer Engineering)
in The University of Michigan
2019

Doctoral Committee:

Professor David Blaauw, Co-Chair
Assistant Professor Hun-Seok Kim, Co-Chair
Associate Professor Alanson Sample
Associate Professor David Wentzloff

Li-Xuan Chuo
lxchuo@umich.edu
ORCID iD: 0000-0002-9340-392X
© Li-Xuan Chuo 2019
All Rights Reserved

To my family and all the lovely people in my life

TABLE OF CONTENTS

DEDICATION ii

LIST OF FIGURES vi

LIST OF TABLES xi

ABSTRACT xii

CHAPTER

I. Introduction 1

1.1 Emerging Computing Devices 1
1.2 Advances on Miniaturized System and Wireless Sensing . . . 3
1.2.1 Millimeter-Scale Computers 3
1.2.2 Wireless Sensing for Location-Based Service 6
1.3 Design Considerations of RF Wireless Systems for IoT 7
1.3.1 Communication Scheme 8
1.3.2 Narrow Band IoT Communication 10
1.3.3 Bandwidth Effect on Wireless Sensing 11
1.3.4 Energy and Power Constraint 12
1.4 Dissertation Outline 13

II. Asymmetric 3x3x3 mm^3 Crystal-Less Radio System Using a Q-Enhanced Amplifier Optimized for Indoor Communication 16

2.1 Introduction 16
2.1.1 Energy efficient sparse modulation 19
2.1.2 Miniaturized 3D antenna 19
2.1.3 Q-enhanced amplifier 19
2.1.4 Asymmetric communication protocol 20
2.2 Overview of the System 21
2.2.1 System Architecture 22
2.2.2 Sparse M-PPM Modulation Scheme 22

2.3 Antenna-Circuit Co-design 24
2.3.1 Frequency Planning 24
2.3.2 Electrically Small Antenna 25
2.3.3 Transmitter Design 26
2.3.4 Receiver Design 27
2.4 Communication Protocol 28
2.4.1 Sensor Initiation Communication 29
2.4.2 Gateway Implementation 30
2.5 Measurement Results 33
2.5.1 System Integration 33
2.5.2 Sensor Node Transmitter Performance 35
2.5.3 Sensor Node Receiver Performance 36
2.5.4 System Measurement 38

III. A 4x4x4 mm^3 Fully Integrated Sensor-to-Sensor Radio using Carrier Frequency Interlocking IF Receiver with -94 dBm Sensitivity 41

3.1 Introduction 41
3.2 Carrier Frequency Interlocking IF Receiver 43
3.3 Link Budget Analysis and Antenna Simulation 45
3.3.1 Path Loss and Antenna Efficiency Analysis 45
3.3.2 Antenna & PCB Simulation 48
3.4 Transceiver Circuits Implementation 48
3.4.1 Transceiver Overview and System Timing 48
3.4.2 DCPO Front-End Design and Operation 49
3.4.3 Carrier Frequency Interlocking IF Receiver Designs 52
3.5 Chip Measurement and Radio System Evaluation 54
3.6 Summary 56

IV. RF-Echo: A Non-Line-of-Sight Indoor Localization System Using a Low-Power Active RF Reflector ASIC Tag and Neural Network ToF Estimation 59

4.1 Introduction 59
4.2 Background 63
4.3 Proposed System: RF-Echo 65
4.3.1 OFDM based Ranging Waveform 68
4.3.2 Synchronization with Crystal-Less Tags 71
4.3.3 Neural Network based ToF Estimation 72
4.3.4 Symbol Combining 76
4.3.5 Multilateration for 2D / 3D localization 77
4.4 Implementation 78
4.4.1 Anchor Design 80
4.5 Evaluation 81

4.6 Related Work 86
4.7 Conclusion 89

V. Conclusions and Future Directions 91

5.1 Summary of Contributions 91
5.2 Other Works 93
5.3 Future Directions 95

BIBLIOGRAPHY 97

LIST OF FIGURES

Figure

1.1 Evolution of computers shows 100x volume reduction of computing devices per decade 3

1.2 Michigan Micro-Mote: a complete millimeter-scale computing platform containing multiple functional layers 4

1.3 Cross technology integration to achieve "More than Moore's law"[106] 5

1.4 The rapid growing users and market in location-based service by Havas media survey 7

1.5 Asymmetrical and symmetrical links shown in general wireless networks 8

1.6 Commercial RF wireless system power breakdown 9

1.7 Semiconductor technology improves by 300x in 20 years but battery energy density improves only 4x [65] 12

2.1 IoT trends on the number of devices and the size ofminiature nodes 17

2.2 Challenges for the mm-scale sensor: (a) mm-scalebattery (b) Electrically small antenna 18

2.3 The proposed fully integrated system with the processor, radio, PV cell, battery, and printed antenna 20

2.4 The proposed radio system with a miniaturized antenna (top-left), RF transceiver on the sensor node (top-center), and the SDR based gateway (bottom-left). Sensor node RF transceiver signal timing is shown in bottom-right 21

2.5 Modulation and recharging scheme 23

2.6 (a) Link loss in LOS and NLOS at 1 meter distance (b) Overall antenna efficiency 24

2.7 The printed 3D magnetic dipole antenna 25

2.8 Transceiver circuits utilizing re-configurable cross-coupled pair as a power oscillator in transmit mode and a Q-enhanced amplifier in receive mode 26

2.9 Q-enhanced amplifier (a) Half-circuit analysis (b) Simulation gain result of QEA 28

2.10 Adaptive sensor-initiation synchronization communication protocol . 29

2.11 DSP datapath implemented on the gateway FPGA 31

2.12 2-D FFT map for sensor node CFO and baseband clock frequency evaluation 32

2.13 Radio system integration includes four boards, two 2Ah thin-film batteries, AlGaAs mm-scale solar cell, processor, decap, and radio chip 33

2.14 Radio die photo in 180 nm CMOS 34

2.15 Other chips in the system 34

2.16 The transmitter performance (a) Tuning range (b)EIRP versus bias current 35

2.17 Carrier frequency drift with temperature in different antenna material (normalized to 25 degree Celsius) 36

2.18 Sensitivity at 10^{-3} BER versus bias current of QEA 37

2.19 Blocker tolerance at different frequency offset 37

2.20 Indoor NLOS testing setup of the system 38

2.21 Sensor node-gateway communication channel monitoring 39

2.22 Transceiver control signal and received return packet (0xBEEF in hex) on sensor node 39

2.23 A 20 MHz bandwidth spectrogram snapshot of the channel 40

3.1 Sensor-to-sensor communication scheme 42

3.2 The proposed receiver architecture and comparison to other works . 44

3.3 Simulated radiation efficiency for electrically-small loop antenna . . 46

3.4 Link budget analysis based on 4x4x4 mm^3 antenna 47

3.5 Antenna and other electronics simulation setup in HFSS 47

3.6 Simulated radiation pattern 48

3.7 Details of the transceiver circuits 49

3.8 Calibration loop timing and the radio sensor node multiple access scheme 50

3.9 Transmitter frequency-locked loop using 32-kHz system real-time-clock 51

3.10 TX FLL measured results, showing it can lock the frequency within 0.1% error from chip-to-chip 52

3.11 Reuse the RX chain with lower gain setting for RO tuning loop . . . 53

3.12 Dual-mode IF amplifier and RO locking measurement results 54

3.13 Testing setup in anechoic chamber 55

3.14 Measured transceiver chip (w/ antenna) EIRP and sensitivity 55

3.15 Measured time domain sensor-to-sensor communication waveform using the fully integrated radio system and the transceiver chip micrograph 56

3.16 The fully integrated radio system including transceiver, processor, PMU, antenna, XTAL, and decaps 57

4.1 RF-Echo: The tag ASIC fabricated in 180nm CMOS (top), and the USRP based anchor (bottom) 60

4.2 Operating principle of the FMCW radar. The time of flight (ToF) is proportional to the beat frequency f_B 65

4.3 The overall RF-Echo system diagram. The anchor broadcasts ≤80MHz OFDM signals at the 2.4GHz carrier frequency and the active reflector IC echoes the OFDM signal in a full duplex fashion. 67

4.4 The OFDM based ToF estimation datapath 68

4.5 The proposed feedforward neural network structure 72

4.6 The proposed bootstrap aggregating method 74

4.7 Ranging accuracy simulated in Matlab with 50ns delay spread multipath channels: (a) Probability density function (PDF) of errors; (b) Cumulative density function (CDF) of errors; (c) Standard deviation of errors from multiple symbol combining and bootstrap aggregation 75

4.8 The active reflector ASIC (a) LNA and mixer circuit schematic; (b) VGA and PA circuit schematic; (c) Chip die photo (fabricated in 180nm CMOS technology) 79

4.9 ASIC tag performance: (a) Impedance matching; (b) Different gain mode setting; (c) Frequency response; (d) Noise figure 82

4.10 The anchor reconstructed channel impulse response and the neural network output confidence. For x-axis, time is converted to distance using $d/c = t$; (a) a LOS channel response; (b) a NLOS channel response 83

4.11 NLOS testing setups and the 1D LOS/NLOS ranging test results in various environments including Atrium, Office, and Hallway. The OFDM symbol length is 20 μs 84

4.12 The 1D ranging error PDF and CDF for data points in Figure 4.11: (a) The error PDF with one or ten confidence-weighted OFDM symbols combining. Each symbol is 20μs long; (b) The CDF for same scenarios 84

4.13 Error standard deviation as a function of the number of OFDM symbols combined 85

4.14 The 2D localization map in a 30×20 m^2 university building (a) Only $A_1 - A_4$ anchors are used to localize $T_1 - T_{15}$ along the blue trajectory. Only $A_4 - A_6$ are used to localize the NLOS positions ($T_{15} - T_{17}$); (b) The CDF of the 2D localization error 86

5.1 RF transceiver with on-chip loop antenna 93

5.2 Top and side view of the system with radio chip, processor, decap, and mm-scale battery 94

5.3 Top and side view of the proposed back-scatter system with radio chip, antenna, processor, solar cell, decap, and mm-scale battery . . 94

LIST OF TABLES

Table

1.1 NB-IoT standards for long-distance communication 10

2.1 Comparison with recent work in millimeter-scale radio 40

3.1 Comparison with prior work 58

4.1 Comparison of accuracy, dimension of field trial environment, tag power, update rate, and energy consumption per localization for a representative sampling of recently published indoor RF localization systems. 90

ABSTRACT

This dissertation focuses on the miniaturized design and implementation of low-power energy-efficient wireless communication and radio frequency (RF) sensing systems, broadening the use case of smart home devices and Internet of Things (IoT). There are several challenges in miniaturizing wireless systems with an integrated antenna into a centimeter or even millimeter-scale. First, millimeter-sized antennae in RF are electrically-small, resulting in low radiation efficiency as well as difficulties to match the impedance. Second, the energy source is limited due to a small form factor battery. Third, bulky off-chip components, such as a high frequency crystal are unavailable due to reduced system dimension and low power consumption. In this dissertation, these challenges are analyzed and tackled by proposing new circuit architecture and system design techniques as well as new algorithms. Three prototypes of the proposed systems were implemented for evaluation and verification. The first one is a crystal-less 3x3x3 mm^3 915MHz asymmetric radio system optimized for non line-of-sight (NLOS) communication. The second work is a fully integrated 4x4x4 mm^3 radio with newly proposed carrier frequency interlocking intermediate frequency (IF) transceiver architecture, enabling a symmetric sensor-to-sensor communication. Last, an energy-efficient and rapidly deployable RF localization system with crystal-less custom-designed tag was proposed together with a neural network time-of-flight estimation algorithm. The prototypes presented in this dissertation prove the feasibility of low-power and energy-efficient miniaturized designs to expand applications of wireless sensor nodes and improve the connectivity of devices in the IoT era.

CHAPTER I

Introduction

1.1 Emerging Computing Devices

Computing devices have changed our lives significantly in recent decades. According to Bell's Law [9], a new class of computers occurs roughly every decade, resulting in new applications and new industries. Since the invention of transistors in 1947, continuous technology scaling has allowed us to pack huge computational power into an incredibly small volume. This has been leveraged to create very small yet highly capable systems as well as new multi-core and networking technologies that push the upper limits of modern computing performance. Thanks to the technology scaling predicted by Moore's law[71], the volume of computing devices has been reduced 100x per decade since the mainframe computers of the 1960s, as shown in Figure 1.1. This miniaturization of computing devices aligns well with Bell's Law. According to this trend, the next generation of computing devices will be millimeter-scale in terms of system volume and able to perform functions in diverse emerging applications.

The concept of millimeter-scale computing devices has been advocated since early 2000 [6]. Such devices, also known as smart dusts or smart motes, are very tiny in volume and manufactured at almost no-cost. As a result, they can be widely deployed in large quantities. More importantly, when such sensors are equipped with wireless connectivity, they can form a powerful and city-wise wireless sensor network

[60]. Such smart dust or swarm devices bridge the gap between smart phones and the concept of the Internet of Things (IoT) [7], moving us one step forward to the Internet of Everything (IoE) [38] and a new era of computing.

The potential applications of millimeter-scale computing systems are appealing and powerful. With their light weight and tiny form factor, these devices can be easily deployed in environments with tight space or weight constraints, such as pervasive agricultural monitoring, healthcare, and bio-sensing applications. Recent examples include the following: 1) Google announced its smart contact lens projects in 2014 for diabetes sensing with small electronics on the lens; 2) a miniaturized sensing system with energy harvesting capability has been demonstrated that can be implanted in the inner ear, powering itself and helping with the diagnosis of hearing loss or other disorders [69]; 3) a small and lightweight(< 30 mg) sensor node that can be attached to insects can aid bio-research and give mobility to IoT devices [48]; and 4) a millimeter-scale implanted neural sensor with wireless communication enables a long-term and more robust brain-machine interface [72]. In addition to these size-constrained applications, a low-cost millimeter-scale sensor could bring benefits to daily life and change the current data-oriented business model with its capability to collect huge amounts of data. For example, a small tag that has tracking capability can be used in shipping or smart warehouse storage [56]. An easily distributed wireless sensor can be used to monitor bridge or road conditions without much labor overhead. A tiny sensor node with motion detection can be used in museum inventory protection. The Boston Consulting Group (BCG) has predicted that by 2020, the IoT market will be worth $300 billion and more than 25 billion connected devices will be in use [15]. Such possibilities open up and motivate new research fields in the development of millimeter-scale sensing and computing devices from various perspectives (systems, circuits, devices, antennas, etc.).

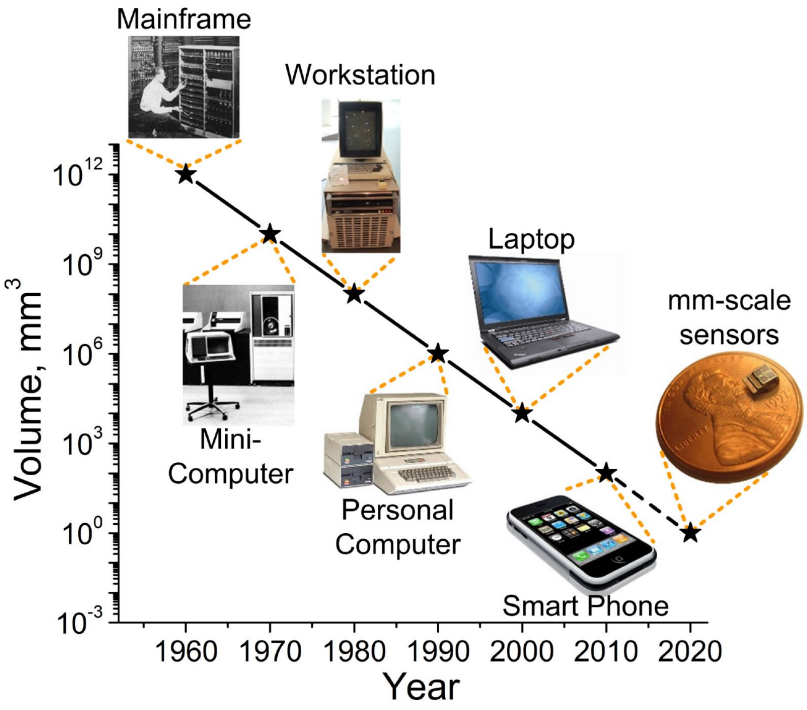


Figure 1.1: Evolution of computers shows 100x volume reduction of computing devices per decade

1.2 Advances on Miniaturized System and Wireless Sensing

1.2.1 Millimeter-Scale Computers

Starting from early 2000, scholars from UC Berkeley proposed the concept of smart dusts, also known as tiny form factor computing devices [6] [104]. They pictured a city-wise sensing network to connect everything together. Since then, the world began embracing the entire IoT industry and big data era. However, the true breakthrough was made in recent years by researchers from the University of Michigan, where complete and systematic studies on millimeter-scale computers were conducted [39] [25] [26] [63]. The resulting computing platform is called the Michigan Micro Mote (M^3), which is the world´s smallest computer and has been exhibited in the Computer History Museum in California for several years. Besides M^3, there have been additional works presented by other universities and research institutes [105] [94] [45].

There has been continuous research focused on developing the techniques required

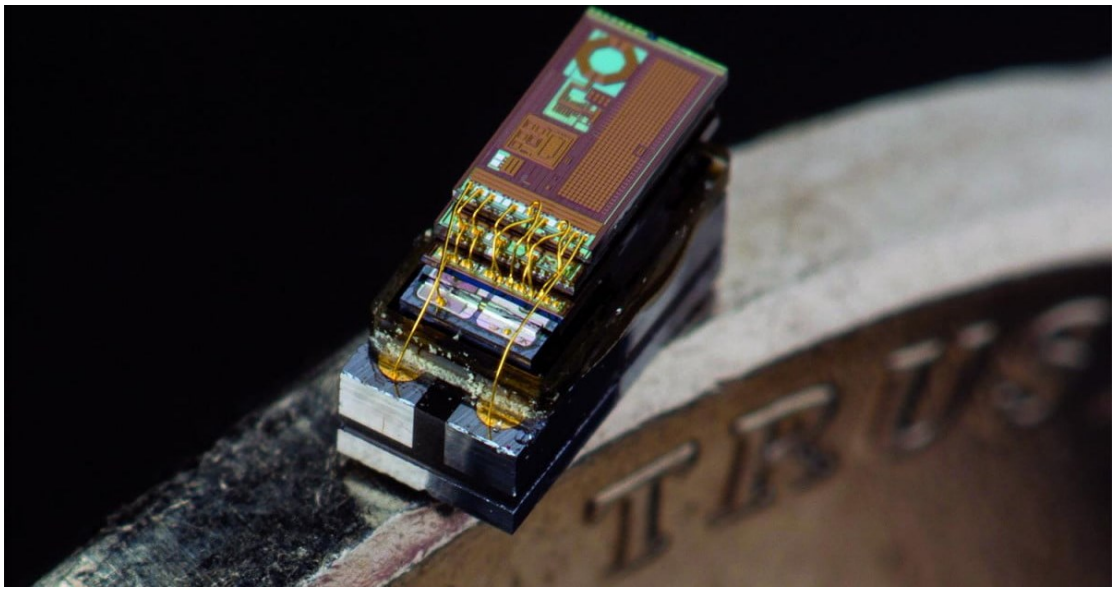


Figure 1.2: Michigan Micro-Mote: a complete millimeter-scale computing platform containing multiple functional layers

for creating such tiny form factor devices including the design of ultra-low-power, energy-efficient integrated circuits and systems using state-of-the-art semiconductor technologies [8] [62] [74] [58] [49] [108] [50]. The M^3 platform introduced a new modular design concept, which is very different from the system-on-chip (SoC) design currently used. Each module (layer) is a stand-alone chip (less than 1 mm x 2 mm in size) with its own function, such as a processor, power management unit, energy harvester, solar cell, radio, etc. The advantage of such a modular design is that each layer can be designed using its optimal semiconductor technologies. Each layer is then stacked and connected together via wire bonding as shown in Figure 1.2. The cross technology integration is called "More than Moore" [106], which has become a very popular concept since Moore's law has reached its limitation as shown in Figure 1.3.

Among the modular layers in a millimeter-scale computing device, the radio frequency (RF) layer for wireless communication is one of the key components since it is hard to collect those tiny devices and make wire connections. The capabil-

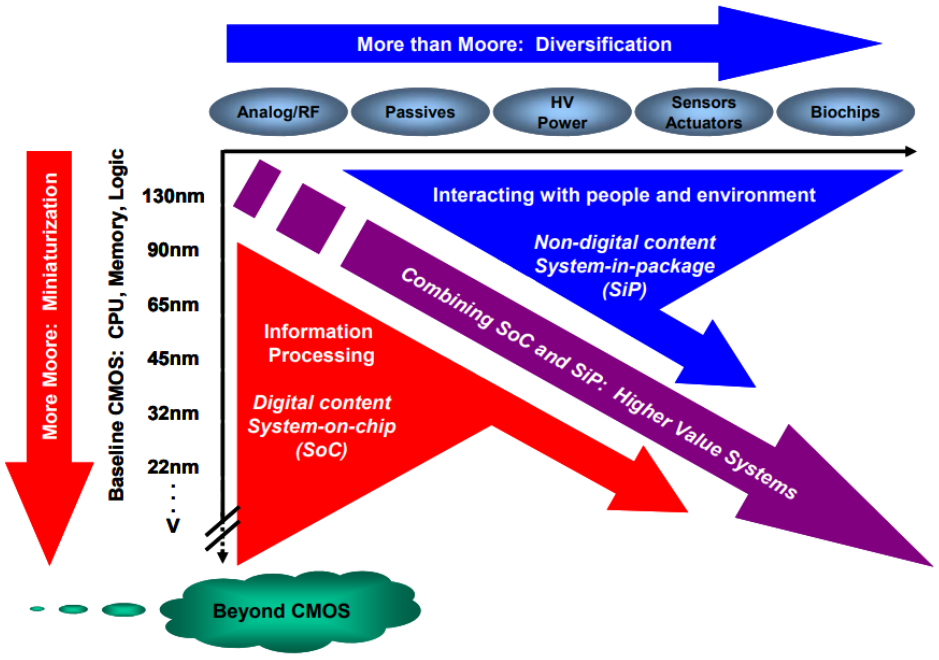


Figure 1.3: Cross technology integration to achieve "More than Moore's law"[106]

ity of retrieving (or sending) data wirelessly from (to) those sensor nodes is critical for real-world applications. The communication distance directly determines the use cases of computing devices, and obviously a longer distance is desired. However, achieving long distance communication for a millimeter-scale device is challenging due to the large energy consumption and high accuracy of frequency/timing synchronization needed. The power budget of such small devices is very limited because millimeter-scale batteries have a low energy capacity and high internal resistance. The small-sized solar cell also cannot provide enough energy for continuous wireless communication. Therefore, a low-power and energy-efficient radio layer design can significantly improve the sensor node lifetime and its use cases.

1.2.2 Wireless Sensing for Location-Based Service

Researchers have been brainstorming about using wireless signals not only for communication but also for sensing purposes. As early as 1886, Heinrich Hertz, who showed that radio waves could be reflected from solid objects, opened up a new research area focused on using radio waves to sense the environment. During World War II, radar techniques were widely adopted in many countries to detect objects kilometers away. By calculating the radar signal round trip traveling time (time-of-flight), we can easily and precisely locate an object. In 1973, the Global Positioning System (GPS) project was started by the US government with the goal of using satellite signals to obtain the geolocation and time information anywhere on or near the Earth. A method of providing knowledge of an object's physical location has been a hot topic in both research and business.

With the popularity of smart phone devices nowadays, an emerging location-based service has grown quickly, with more than 2000 million users in 2016, as shown in Figure 1.4. A wide variety of applications such as intelligent shopping malls and warehouses and public safety tracking are becoming realities. Similar to the search engine on the Internet, the localization system is a search engine for the physical world.

There are lots of commercial localization systems on the market, but they are either too power-hungry or not suitable for indoor usage. The GPS system has very good service coverage; however, it has poor indoor accuracy. Most of the indoor localization systems now on the market, such as WiFi or BLE, are Received Signal Strength Indicator based. Their typical accuracy is on the order of meters, and the coverage is not large. An ultra-wide band (UWB) system has been an attractive solution for indoor localization. It has good accuracy and is immune to the multi-path effect. However, its maximum transmit power and distance are limited by FCC regulations due to the large bandwidth(>GHz). In order to achieve a certain SNR

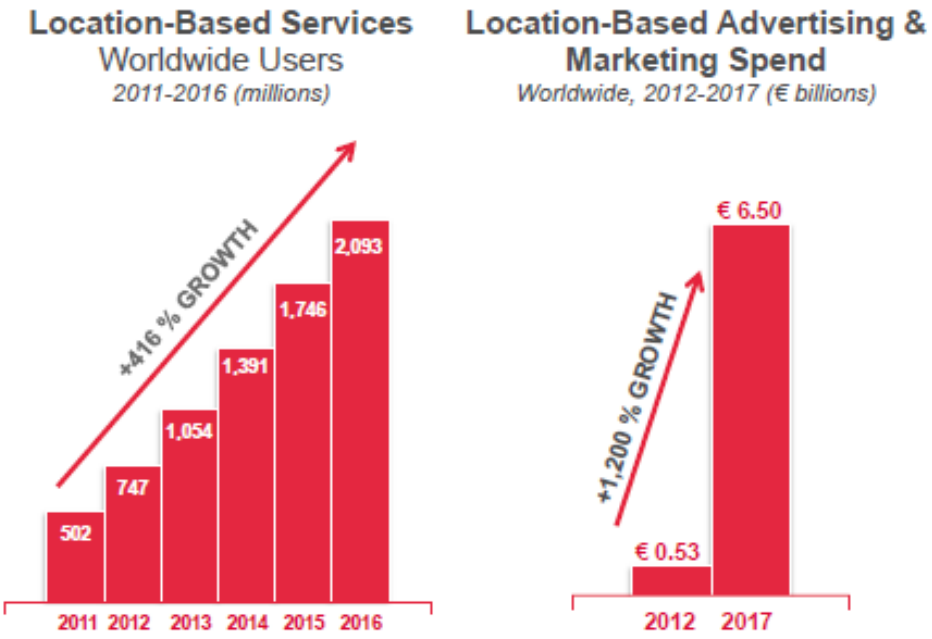


Figure 1.4: The rapid growing users and market in location-based service by Havas media survey

and timing synchronization, a UWB system normally requires a long integration time; thus, the complexity and energy consumption is high. As a result, a ubiquitous energy-efficient indoor localization system is needed to enable more location-based services and applications.

1.3 Design Considerations of RF Wireless Systems for IoT

This dissertation focuses on designing a low-power energy-efficient RF wireless system that is sufficiently miniaturized to fit onto a millimeter-scale computing platform. To integrate into such a small form factor, the circuits and systems need to be re-designed and the communication protocol must be optimized. This poses unique challenges and special design considerations.

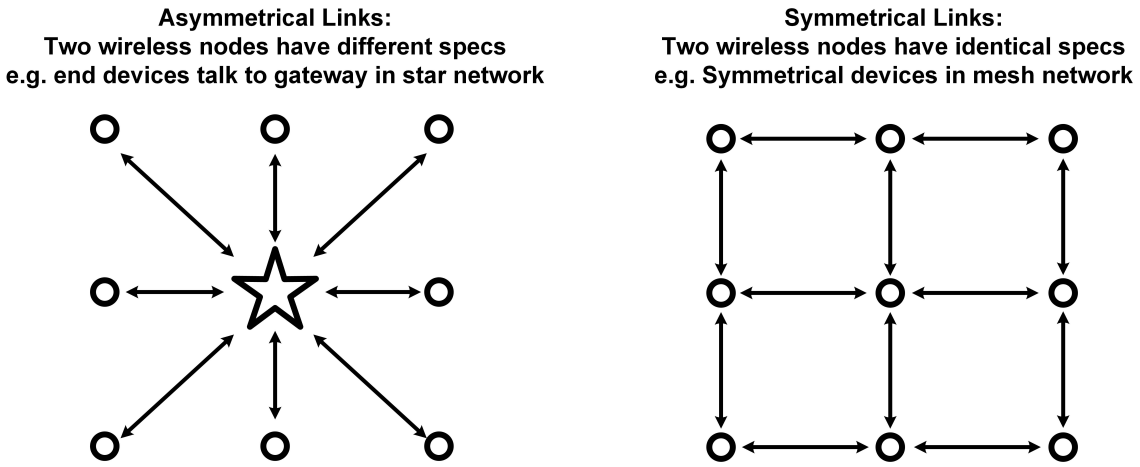


Figure 1.5: Asymmetrical and symmetrical links shown in general wireless networks

1.3.1 Communication Scheme

As shown in Figure 1.5, a wireless link can be categorized as asymmetric or symmetric communication. In asymmetric communication, there is a centralized gateway device that has high computational power and resources that can be used to communicate with other distributed end devices. The distributed end devices usually have limited computational resources and can only be connected to the gateway device. Most of the recent IoT communication protocols, such as Bluetooth Low-Energy (BLE), ZigBee, and cellular, use such a topology. Signal relays are accomplished by an intermediate device that has better hardware. The advantage of asymmetric communication is obviously in shifting all the heavy signal processing and the power-hungry system to the gateway device, resulting in a simple, low-cost, low-power end device. The millimeter-scale wireless sensor node is a perfect candidate for using this type of communication scheme due to its limited energy resource. However, the number of gateway devices determines the coverage of the sensor network.

On the other hand, in a symmetric communication link, all of the sensor nodes will have the same hardware and can connect to each other to form a mesh network. The advantage of this scheme is that it avoids a centralized potentially high-cost gateway

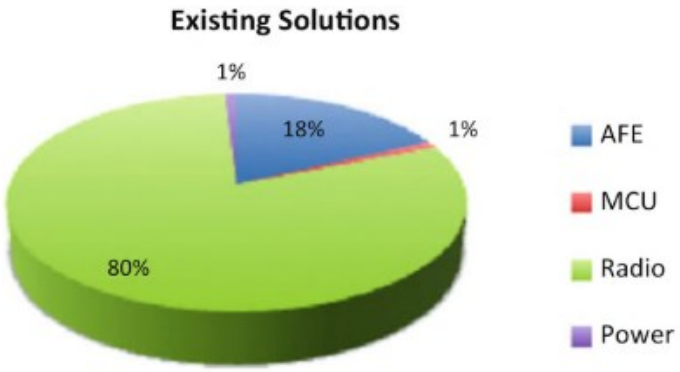


Figure 1.6: Commercial RF wireless system power breakdown

device. The signal can be relayed by other nearby sensor nodes. With a large number of sensor nodes deployed, a powerful and complicated mesh network can be formed easily, making new IoT applications possible. There are several challenges associated with this communication scheme, making it an active research focus for both academia and industry. First, the trade-off between synchronization and duty cycle in the sensor node must be considered. A heavier duty cycle scheme can save energy, but it will make the synchronization harder (drift more) each time the node wakes up. Second, a low-power RF transceiver front-end design is required. As shown in Figure 1.6 [68] [36], the radio usually dominates the power consumption of the entire wireless sensor node. This will get worse in the symmetric communication link since with the absence of a powerful gateway, the sensor node needs to have a good transceiver to achieve a reasonable link distance.

This dissertation will first discuss the radio system design trade-off using an asymmetric link, and finally a low-power RF transceiver architecture will be discussed that uses symmetric link communication.

1.3.2 Narrow Band IoT Communication

A communication protocol defines the radio's physical layer specifications, packet organization, and synchronization scheme between wireless nodes in a network. Most of the IoT sensing devices do not require a high data rate; instead, they typically require wider wireless connectivity coverage. As a result, there are increasing developments in low-power narrow-band/ultra-narrow band communication for long distance IoT applications (NB-IoT) such as Sigfox, Neul, and LoRaWAN. The targeted communication distance is a few kilometers to 10s of kilometera in an open area. Those protocols usually use sub-GHz ISM frequency band for better signal propagation in either a line-of-sight or non-line-of-sight scenario, and the data rate is a few to 100k bps. Table 1.1 summarizes some recent popular NB-IoT standards.

	Frequency (MHz)	Data Rate (bps)	Target Range
Sigfox	900 (ISM)	10 - 1000	30-50km (rural) 3-10km (urban)
Neul	900 / 470-790 (TV White Space)	Few - 100k	10km
LoRaWAN	900 (ISM)	300 - 50k	15km (rural) 2-5km (urban)

Table 1.1: NB-IoT standards for long-distance communication

In addition to the existing standards, custom-designed protocols are also possible and desirable when we want to reduce the system form factor down to millimeter-scale and the energy resource is stringently limited. However, the choice of carrier frequency and radiation power must be compliant with the Federal Communications Commission (FCC) requirements [33]. The most popular frequency bands for custom protocols are located at the free ISM bands, especially at 915 MHz and 2400 MHz. In this dissertation, a custom-designed narrow band sensor initiation communication protocol is proposed to achieve millimeter-scale radio system design.

1.3.3 Bandwidth Effect on Wireless Sensing

One of the conventional approaches used to perform RF signal based ranging is to utilize a received signal strength indicator (RSSI) [113][10][87][10]. The pathloss expression of RF signal propagation directly maps the RSSI to a distance using an inverse-square law. Due to the simplicity of measuring the RSSI, it has been widely adopted in WiFi and Bluetooth for ranging. Unfortunately, in non-LOS and multi-path rich environments, signal fading results in large deviations in RSSI from the theoretical pathloss equation. It is known that the RSSI follows a Rayleigh or log-normal distribution statistically in many practical multipath scenarios, which indicates large errors ($>$ a few meters) in ranging. Another approach that has been widely used is an impulse radio (IR) ultra-wide bandwidth (UWB) system where very short width pulses are transmitted and the arrival time of each pulse is estimated at the receiver to obtain the time-of-flight of the transmitted signal [40][102][114][64]. The bandwidth of an UWB signal is inversely proportional to the pulse width, and narrower pulses are preferred to obtain finer time resolution in ToF estimation. Frequency Modulated Continuous Wave (FMCW) radar is also a popular ranging approach in current vehicle collision avoidance systems.

To achieve accurate sensing, the signal bandwidth is often inversely proportional to the resolution as shown in Equation1.1. Large bandwidth means higher hardware costs, power-hungry systems, and shorter distances due to 1) high sampling speed (GHz) ADC for accurate sampling; 2) high power RF front-end design due to the bandwidth requirement; and 3) limited peak transmit power due to FCC regulations on large bandwidth transmissions. All of the above reasons make it difficult to miniaturize the RF wireless sensing system. In this dissertation, we will explore and discuss a novel way of designing a low-cost energy-efficient wireless sensing system that enables miniaturization and long distance localization.

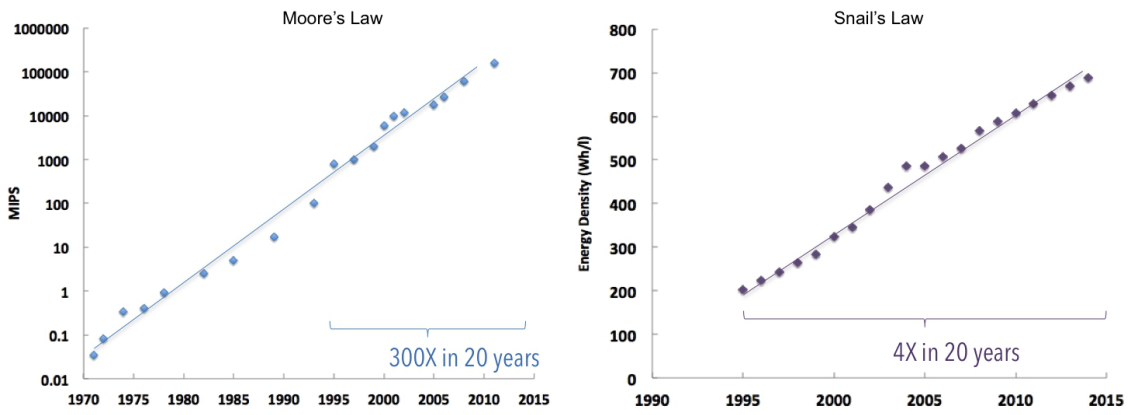


Figure 1.7: Semiconductor technology improves by 300x in 20 years but battery energy density improves only 4x [65]

$$Resolution \propto \frac{1}{Bandwidth} \tag{1.1}$$

1.3.4 Energy and Power Constraint

Another challenge is the extreme energy and power constraints imposed on millimeter-scale systems. As shown in Figure1.7, the battery technology follows Snail's law, which predicts a relatively slow improvement over time compared to Moore's law as it relates to semiconductors. A millimeter-scale lithium battery typically has < 10 μAh capacity with high internal resistance ($\sim$10 kΩ), preventing it from supplying high peak power to the system. Second, a millimeter-scale solar cell also harvests energy slowly (100s nW/mm^2), and it heavily depends on the light conditions[98]. These limitations present a challenge in designing radio systems due to energy sourcing limitations. Several circuits and system design techniques such as the use of an energy reservoir, power management, and duty-cycling were employed and analyzed in this dissertation. Fortunately, the battery dimension does not have a linear relationship with the capacity. For example, a coin cell battery with a diameter of 4.8 mm has 1 mAh capacity and < 100 Ω internal resistance, which can be used in a

bigger system with a greater performance requirement.

1.4 Dissertation Outline

This work contributes to the development and miniaturization of low-power and energy-efficient wireless systems that tackle the challenges described in Section 1.3. We also investigate a neural network resolution enhancement technique. Combining these techniques, we are able to demonstrate low-power energy-efficient RF systems.

In Chapter II, a 915 MHz asymmetric communication system for an ultra-small wireless sensor node fully integrated within a 3×3×3 mm^3 form factor is presented. The system integrates multiple stacked layers including a PLL-less RF transceiver, ultra-low power (ULP) processor, photovoltaic (PV) energy harvester, and a 3D magnetic dipole antenna. Real-time, end-to-end communication between a custom designed gateway and the mm-scale sensor node is demonstrated via a novel sensor-initiating communication protocol. The transceiver front-end circuit is co-designed with the printed 3D magnetic dipole antenna to form a power oscillator for the transmitter (TX) as well as a Q-enhanced amplifier (QEA) for the receiver (RX). In TX mode, the average packet transmission consumes 60.6 μW at 7.3 kbps data rate using 4 μs pulse width, 128 μs recharging time, and a binary PPM coding rate of 1. During RX mode, the cross-coupled pair is reused in the non-oscillating region, enhancing the quality factor (Q) of the resonant tank from 110 to 300 and resulting in -93 dBm sensitivity with 1.85 mW power consumption. The 3×3×3 mm^3 fully integrated, standalone sensor node is demonstrated to obtain bi-directional real-time wireless communication to an FPGA-implemented gateway over a distance of 20 meters in challenging non-line-of-sight (NLOS) indoor scenarios and >30 m in line-of-sight (LOS) conditions.

In Chapter III, an ultra-low power mm-scale symmetrical communication IoT platform is presented that enables newly emerging applications such as pervasive

agricultural monitoring and bio-sensing. We introduce a 4×4×4 mm^3 fully integrated radio system that integrates a transceiver chip, antenna, power management unit, and baseband processor for sensor-to-sensor bi-directional mesh networks. The proposed system uses a low power 32 kHz crystal reference frequency and a novel carrier frequency interlocking IF receiver to achieve low power consumption. It achieves -94 dBm sensitivity with 97 μW power consumption and -12.6 dBm EIRP for sensor-to-sensor mesh network communication.

Long-range low-power localization is a key technology that enables a host of new applications of wireless sensor nodes. In Chapter IV, we present *RF-Echo*, a new low-power RF localization solution that achieves decimeter accuracy in long-range indoor non-line-of-sight (NLOS) scenarios. RF-Echo introduces a custom-designed active RF reflector ASIC (application specific integrated circuit) fabricated in a 180-nm CMOS process that echoes a frequency-shifted orthogonal frequency division multiplexing (OFDM) signal originally generated from an anchor. The proposed technique is based on time-of-flight (ToF) estimation in the frequency domain that effectively eliminates inter-carrier and inter-symbol interference in multipath-rich indoor NLOS channels. RF-Echo uses a relatively narrow bandwidth of $\leq$80 MHz, which does not require an expensive very high sampling rate analog-to-digital converter (ADC). Unlike ultra-wideband (UWB) systems, the active reflection scheme is designed to operate at a relatively low carrier frequency that can penetrate building walls and other blocking objects for challenging NLOS scenarios. Since the bandwidth at lower frequencies (2.4 GHz and sub-1 GHz) is severely limited, we propose novel signal processing algorithms as well as machine learning techniques to significantly enhance the localization resolution given the bandwidth constraint of the proposed system. The newly fabricated tag IC consumes 62.8 mW active power. The software-defined radio-(SDR)-based anchor prototype is rapidly deployable without the need for accurate synchronization among anchors and tags. Field trials conducted in a university build-

ing confirm up to 85 m operation with decimeter accuracy for robust 2D localization.

Future work and directions are stated in Chapter V. A new mesh communication protocol for low-power wireless sensor node is needed. The protocol has to consider multiple hardware design challenges in order to have a holistic system optimization. There is still no good transmitter and energy harvesting topology for millimeter-scale wireless sensor node applications. This is critical in order to push the smart dust or smart city into real world usage. Furthermore, as the advances in AI technology development, there should be a better algorithm to improve the wireless sensing resolution without sacrificing the limited bandwidth.

CHAPTER II

Asymmetric 3x3x3 mm^3 Crystal-Less Radio System Using a Q-Enhanced Amplifier Optimized for Indoor Communication

2.1 Introduction

The number of connected smart devices is fast growing towards the highly anticipated vision of the ubiquitous Internet-of-Things (IoT). Along the trend of explosive growth of connected IoT devices, shown in Figure 2.1, the sensor node's form-factor has recently scaled down to centimeter, or more aggressively to millimeter scales [24] [93]. Making the wireless sensing system smaller, lower-power and more affordable has become an important problem for both industry and academic research. A mm-scale distributed sensor node enables novel applications such as industrial ubiquitous sensors, smart cities [59], agricultural monitoring [46], implantable bio-medical devices and unobtrusive surveillance systems. There are two main challenges for these applications to thrive, cost and performance. As a result, the communication solution for these IoT applications needs to cover a long (10's of meter) distance while maintaining the ultra-small (mm-scale) form-factor including the antenna.

There are numerous challenges for radio systems when fully integrated within a mm-scale form-factor. First, the extremely limited system dimension constrains

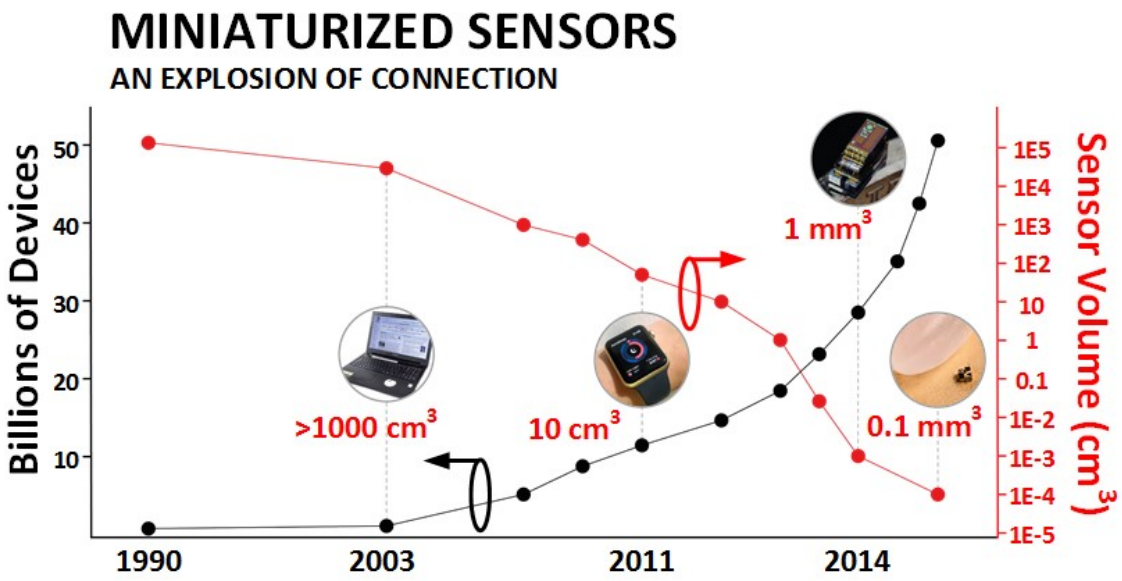


Figure 2.1: IoT trends on the number of devices and the size ofminiature nodes

the usage of off-chip components. Even the smallest crystal oscillator is considered to be excessively large for the target system dimension. Second, the system needs to be powered by mm-scale thin-film batteries shown in Figure 2.2(a), which have extremely small capacity ($<10\mu$Ah) and high internal resistance (10 – 30 kΩ) that limits the peak current of the battery to be $< 100\mu W$. Third, as these batteries cannot be easily replaced, the system needs to be energy-autonomous, recharging the battery via harvested ambient energy. Lastly, an electrically-small mm-scale antenna typically results in very poor antenna efficiency especially at a relatively lower frequency (sub-GHz) which is preferred for better wall penetration in non-line-of-sight (NLOS) scenarios. For example, the 3×3×2 mm^3 printed antenna shown in Fig. 2.2(b) has 0.46% efficiency at 915 MHz although it was carefully designed for the maximum efficiency given the area constraint.

While there are many existing international standards for IoT connectivity such as Bluetooth Low-Energy (BLE)[1] and ZigBee [4], their relatively high carrier frequency, complexity, and power consumption limit their NLOS communication distance and/or

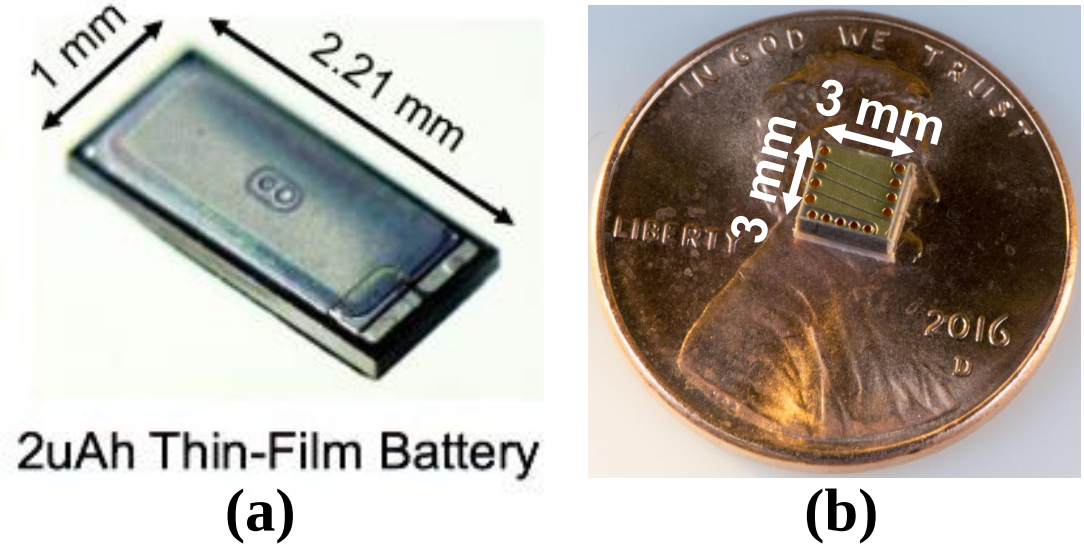


Figure 2.2: Challenges for the mm-scale sensor: (a) mm-scalebattery (b) Electrically small antenna

applicability to mm-scale sensor nodes. Z-wave [3] targets the longer distance indoor environment by using a lower carrier frequency (sub-GHz). But all of the existing systems impose a stringent specification for the frequency accuracy, timing stability, and quality of the continuous waveform that are unattainable in a mm-scale energy-autonomous wireless node. Active research is on-going in the area of the ultra-low power (ULP) wireless communication solutions [93] [14] [84] [83]. However, they typically focus on low-power transceiver front-end designs and do not address system integration challenges or power management issues that are unique and critical to the mm-scale IoT systems.

In this work, we propose an energy-autonomous radio system fully integrated within a 3×3×3 mm^3 form-factor operating in the 915MHz ISM band for indoor NLOS communications. The system is constructed from several layers (chips) that are stacked, connected through wire bonding [61] and placed on one side of a miniaturized printed antenna. Our system is crystal-less and solely powered by the energy

harvested from a mm-scale PV cell. We have employed the following major techniques to achieve an ultra-low power, crystal-less mm-scale system for indoor bidirectional communication to a gateway [31]:

2.1.1 Energy efficient sparse modulation

To increase the instantaneous transmit power, our radio system draws the power from a charge reservoir capacitor. This buffered energy scheme results in an impulse-like transmit signal that is sparse in the time domain. We encode multi-bit information in the position of sparse pulses to achieve higher TX energy efficiency.

2.1.2 Miniaturized 3D antenna

We investigate and quantify the performance of two types (magnetic and electric) of electrically small dipole antennas co-designed with the transceiver circuit for NLOS indoor operating scenarios. We tightly integrate a highly custom-designed $3\times3\times2$ mm^3 3D magnetic dipole antenna into the system to resonate with off-chip lumped components without conventional antenna impedance matching.

2.1.3 Q-enhanced amplifier

The mm-scale magnetic dipole antenna and ULP RF circuits are co-designed to maximize the RX and TX efficiency. We utilize a cross-coupled driver to resonate the magnetic dipole antenna at the carrier frequency with a quality factor (Q) of > 100 in order to achieve the ULP transmitter power consumption of 60μW during transmission. In receive mode, we achieve a very aggressive RX sensitivity level of -93 dBm at the input of the -21.34 dBi gain of mm-scale antenna (available power is -114 dBm) by reusing the cross-coupled driver in a non-oscillating mode to raise the Q of the resonant tank to achieve > 49 dB voltage gain at 40μW, replacing a power-hungry LNA and bulky off-chip filter all together.

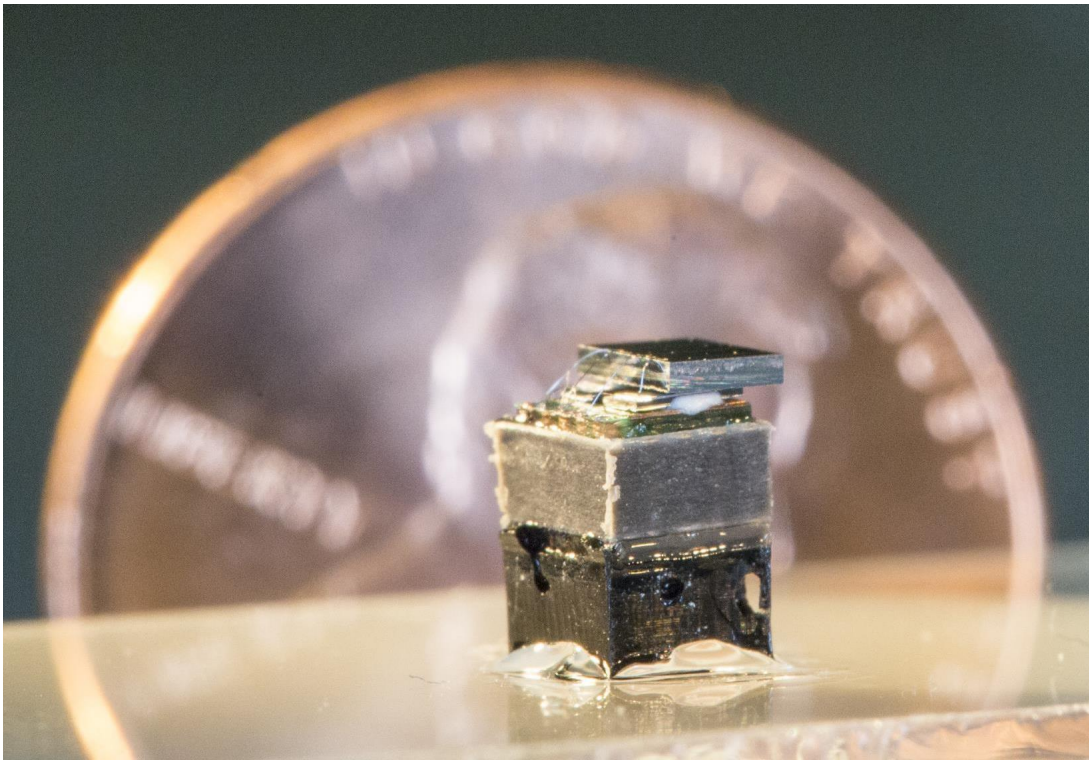


Figure 2.3: The proposed fully integrated system with the processor, radio, PV cell, battery, and printed antenna

2.1.4 Asymmetric communication protocol

A novel synchronization protocol is employed to improve the sensor node receiver energy efficiency and to allow crystal-free PLL-less operation of the mm-scale sensor node by utilizing accurate timing and frequency offset estimation capability implemented on the gateway.

Combining these techniques, we demonstrate a fully functional standalone bidirectional communication system between the mm-scale energy-autonomous sensor node and a real-time gateway. It achieves up to 20 m in challenging NLOS environment. The complete system has a 3×3×3 mm^3 form factor including the processor, radio transceiver, baseband controller, antenna, thin-film battery, and the PV cell as shown in Figure 2.3.

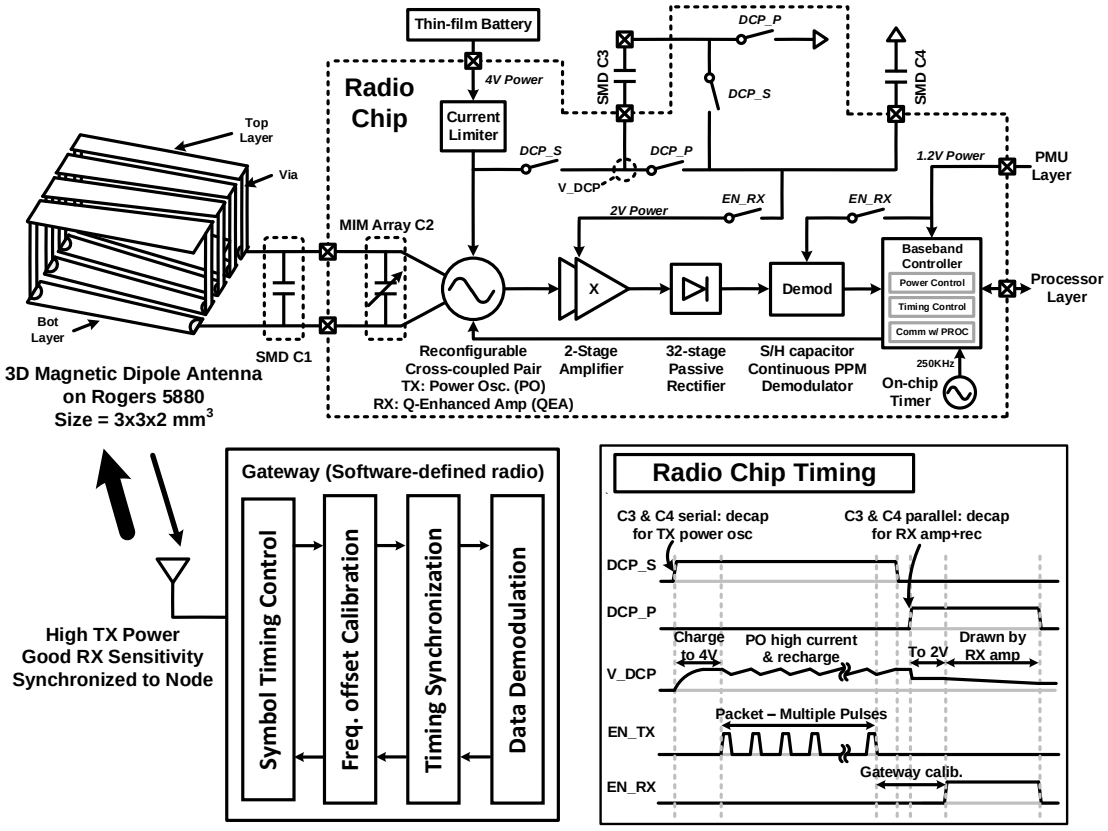


Figure 2.4: The proposed radio system with a miniaturized antenna (top-left), RF transceiver on the sensor node (top-center), and the SDR based gateway (bottom-left). Sensor node RF transceiver signal timing is shown in bottom-right

2.2 Overview of the System

While a crystal-free PLL-less radio is necessary to enable ultra-small system integration and to lower power consumption, it inevitably sacrifices frequency stability. To address this, the system employs a gateway assisted synchronization protocol that is initiated by sensor node transmission. In this protocol, the sensor node always initiates a communication session by transmitting a packet first. The gateway estimates and tracks the timing/frequency offset of the sensor node via a computationally efficient 2D-FFT based correlation (discussed in 2.4), and then it sends a customized packet that *pre-compensates* the timing / frequency offset of the sensor node. This

gateway-assisted synchronization not only allows crystal-free sensor node implementation but also eliminates the need for a power-demanding synchronization/correlation process at the mm-scale sensor node. The gateway protocol and real-time baseband signal processing are implemented on the FPGA of the USRP X310 [100] software defined radio platform.

2.2.1 System Architecture

Figure 2.4 shows the system block diagram and timing of the radio chip of the sensor node. The chip consists of the RF front-end, power management, and baseband controller circuitry with a low-power on-chip timer [30]. The baseband controller directly modulates the transmitter bias current to generate RF modulated pulses. The receiver performs energy detection with a Q-enhanced amplifier followed by additional amplifiers and a 32-stage passive rectifier. Because the transmitter and receiver operate at different voltage domains, the transceiver uses two off-chip energy buffer capacitors to generate two different voltages across either parallel- or series-configured capacitors (Figure 2.4 top). As shown in Figure 2.4 timing diagram, two capacitors are in series in the TX mode and charged to 4V through the current limiter. In RX mode, on the other hand, capacitors are configured in parallel to generate 2V supply.

2.2.2 Sparse M-PPM Modulation Scheme

A major issue of the mm-scale battery is its high internal resistance, which prevents drawing large peak current (mA range) to transmit RF signals. We tackle this issue by powering the transceiver with a trickle charged energy buffer/reservoir capacitor. Instead of pulling current directly from the battery, the transmitter pulls high instantaneous current from the capacitor to generate RF pulses as shown in Fig. 2.5. The battery is continuously recharged through the mm-scale PV cell with variable harvested energy depending on the ambient light condition, ranging from a few nW

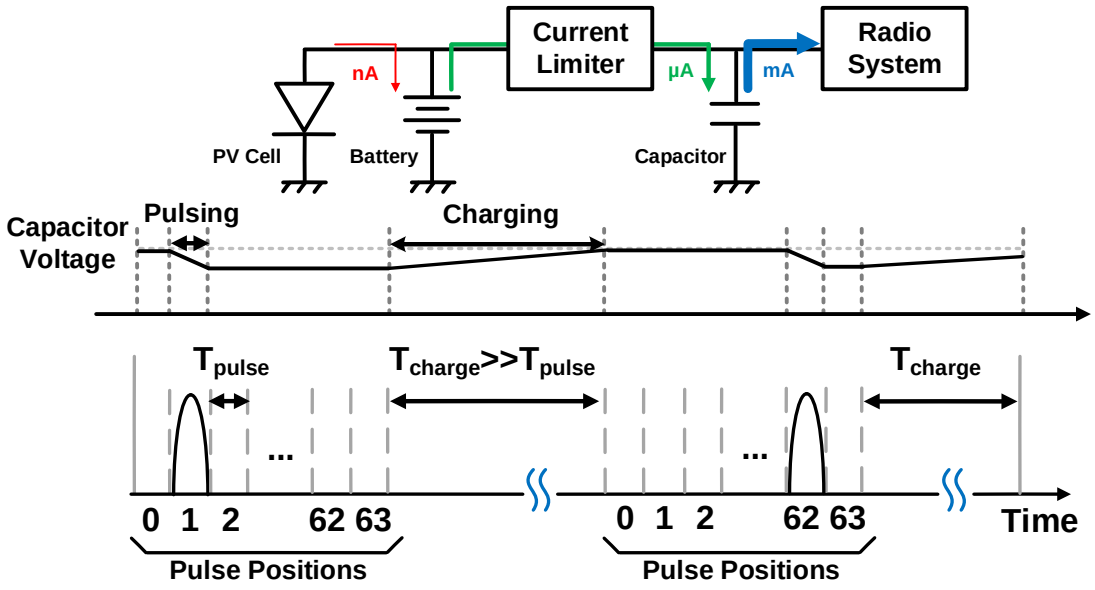


Figure 2.5: Modulation and recharging scheme

in a dimmed indoor room to tens of μW under outdoor sunlight. After each pulse transmission, the battery trickle charges the capacitor to its nominal voltage. Since the recharging time is much longer than the pulse duration, the transmitted pulses are inevitably sparse in time domain. The proposed system exploits this sparsity to realize an energy efficient M-ary pulse position modulation (M-PPM) scheme, where each pulse can convey more than one information or coded bits. Unlike conventional M-PPM, the symbol duration is dominated by the recharging time, not by M pulse position slots. Hence the pulse rate degradation from the long recharging time is amortized by using a relatively large M. The transmitter supports a wide range of $M = 2, 4, 8, ..., 64$ to send up to 6 bits per pulse as shown in Fig. 2.5 for the improved energy efficiency of the pulse based modulation.

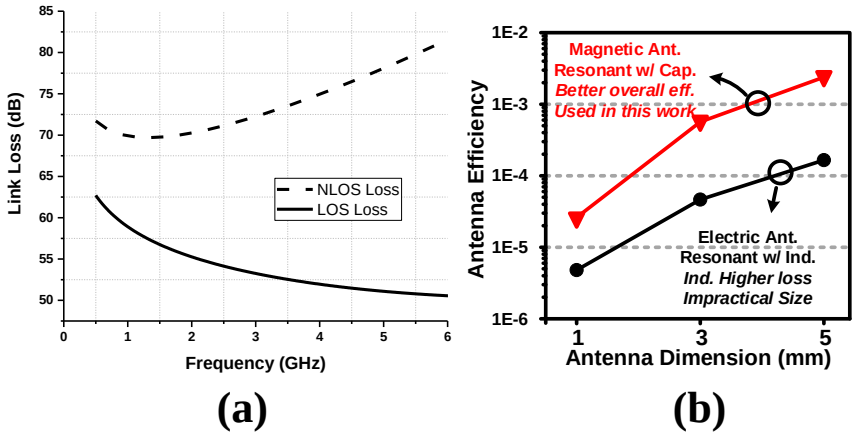


Figure 2.6: (a) Link loss in LOS and NLOS at 1 meter distance (b) Overall antenna efficiency

2.3 Antenna-Circuit Co-design

2.3.1 Frequency Planning

To find the optimal carrier frequency for the mm-scale system, we evaluate the impact of carrier frequency based on a modified ITU indoor path loss model [47]. The floor penetration loss for NLOS communication is modeled by fitting the real measurement data [29]. In Figure 2.6(a), we show link loss versus frequency, including the path loss at 1 meter distance, antenna efficiency, and the wall penetration loss.

Figure 2.6(a) shows that, in LOS, the link loss monotonically decreases as the carrier frequency increases to 6 GHz. This is due to the improved antenna efficiency at higher frequency given $3\times3\times2$ mm^3 antenna dimension (Figure 2.6(b)). For the same reason, mm-Wave has been a typical choice for prior mm-scale radio systems [23], [93]. However, the link loss analysis changes significantly if the wall penetration loss in NLOS conditions is considered. Floor or wall penetration incurs additional frequency-dependent signal attenuation [70], [97], which offsets the better antenna efficiency at higher frequencies given $3\times3\times2$ mm^3 antenna dimension. Including the frequency dependent floor/wall penetration loss reveals the optimal frequency of approximately

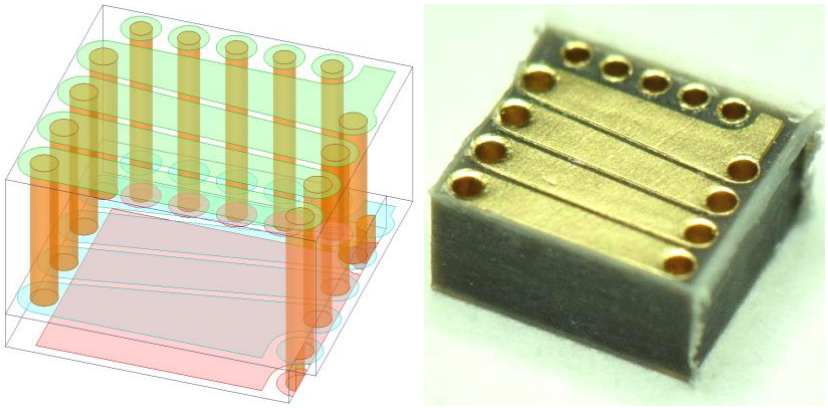


Figure 2.7: The printed 3D magnetic dipole antenna

1 GHz for the minimum link loss in NLOS operations for our target system. Based on this analysis, we select the 915 MHz ISM band as our system carrier frequency. This frequency selection can give us: 1) Better link loss in a NLOS environment, 2) Less interference compared to a more crowed ISM band such as 2.4 GHz, and 3) Lower power consumption for a relatively low carrier frequency generation.

2.3.2 Electrically Small Antenna

Compared to the wavelength of the 915 MHz carrier frequency, the $3\times3\times2$ mm^3 antenna dimension is small [11]. The antenna operates at an off-resonance point with very low radiation efficiency. We investigate two categories of electrically small antennas. One is an electric dipole with capacitive impedance, and the other is a magnetic dipole with inductive impedance. The standalone electric dipole has better efficiency than the magnetic dipole given the mm-scale antenna dimension. However, in a practical antenna-circuit co-designed system, we need to resonate (impedance match) the antenna at 915 MHz to generate the carrier frequency. The electric dipole needs hundreds of nH inductance for matching, which will be lossy and bulky. In contrast, the magnetic dipole requires only a few pF capacitance to match. A pF

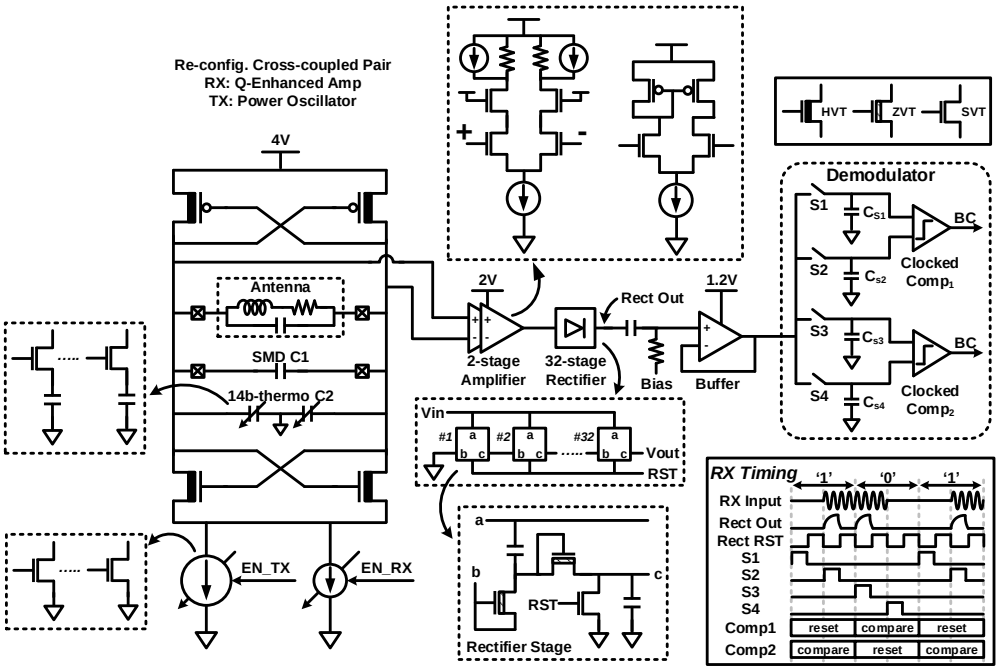


Figure 2.8: Transceiver circuits utilizing re-configurable cross-coupled pair as a power oscillator in transmit mode and a Q-enhanced amplifier in receive mode

capacitor is available on-chip and typically realizable with a high Q. A fair comparison between electric and magnetic dipole antennas including the quality factor of resonant (matching) components is shown Figure 2.6(b). When co-designed and matched with circuits for frequency generation, the magnetic dipole has higher efficiency for our target mm-scale dimension. In addition, the magnetic dipole antenna allows us to put electronics on the top or bottom side of the antenna without significantly affecting the radiation efficiency. This is particularly useful to enable more compact integration of the mm-scale system. The proposed system uses a $3\times3\times2$ mm^3 magnetic dipole antenna printed on a low-loss Rogers 5880 material as shown in Figure 2.7. The antenna exhibits a 0.46% efficiency at 915 MHz from HFSS simulation.

2.3.3 Transmitter Design

Figure 2.8 shows the transceiver front-end circuits and timing details. In transmit mode, the baseband controller directly modulates the EN_TX signal to transmit

M-PPM modulated RF pulses. The transmitter has a power oscillator structure that uses the antenna as the resonant inductive component with 4V supply to maximize the output power. It transmits the signal through parallel amplification of the current flows through the antenna coil. This structure does not require an additional carrier frequency generation (local oscillator) circuitry, which typically consumes a significant portion of the transmitter power. The intrinsically high-Q antenna lowers the power consumption of oscillation, and the transmitter exhibits a measured efficiency of 14.8%. In order to maximize the Q of the oscillation tank, we use a high-Q off-chip SMD capacitor as the coarse frequency tuning component in addition to two on-chip capacitor banks for finer frequency tuning. One major challenge of this free-running oscillator approach is the RF carrier frequency offset (CFO) and drift. In Section IV, we discuss an efficient 2D-FFT based real-time carrier frequency offset mitigation technique performed on the gateway.

2.3.4 Receiver Design

In receive mode, we employ a Q-enhanced amplifier (QEA) in the front-end followed by a 2-stage amplifier and a 32-stage rectifier, which serves as an envelope detector (ED). Unlike the adaptive sparse M-PPM uplink signals, the downlink signal from the gateway is always binary PPM modulated without a long (recharge) interval between symbols. For demodulation of the binary PPM, the receiver compares the energy at two consecutive pulse positions. This scheme eliminates the need for a carefully-tuned threshold voltage for the comparator in conventional on-off keying (OOK) receivers. The proposed relative energy comparison approach for binary PPM also results in better interference tolerance compared to OOK. The RX demodulation timing is shown in Figure 2.8. For the QEA, the transceiver disconnects the cross-coupled pair and taps out the Vout point as shown in Figure 2.9(a). This configuration is different from the parallel resonant circuit formed in the transmit mode.

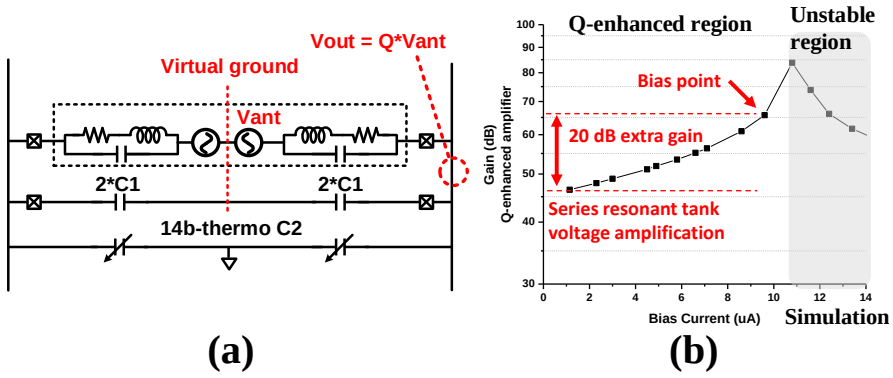


Figure 2.9: Q-enhanced amplifier (a) Half-circuit analysis (b) Simulation gain result of QEA

The antenna and the tuning capacitor form a series resonant circuit so that the received voltage is amplified by the factor of Q. Figure 2.9(b) shows the Q-enhanced amplifier gain versus the bias current plot. We set the bias current with a sufficient back-off margin to ensure its stability. The boosted-Q provides additional 20 dB gain at RF with very low power consumption (40 μW). In addition, the high-Q tank enables a highly band-selective front-end filter, which increases the receiver blocker tolerance and eliminates the need for an off-chip channel selection filter. Unlike super-regenerative receivers [14], the proposed Q-enhanced amplifier does not have the oscillation period or the re-radiation issue. This allows safely co-designing the QEA with the antenna without an isolation amplifier, which is typically required in the super-regenerative receiver [14].

2.4 Communication Protocol

The proposed system uses an asymmetric link between the gateway and distributed sensor nodes as the gateway has much relaxed constraints on power, complexity, and form-factor dimension. The proposed system is based on a star network topology, where every sensor node is individually linked to a nearby gateway. The

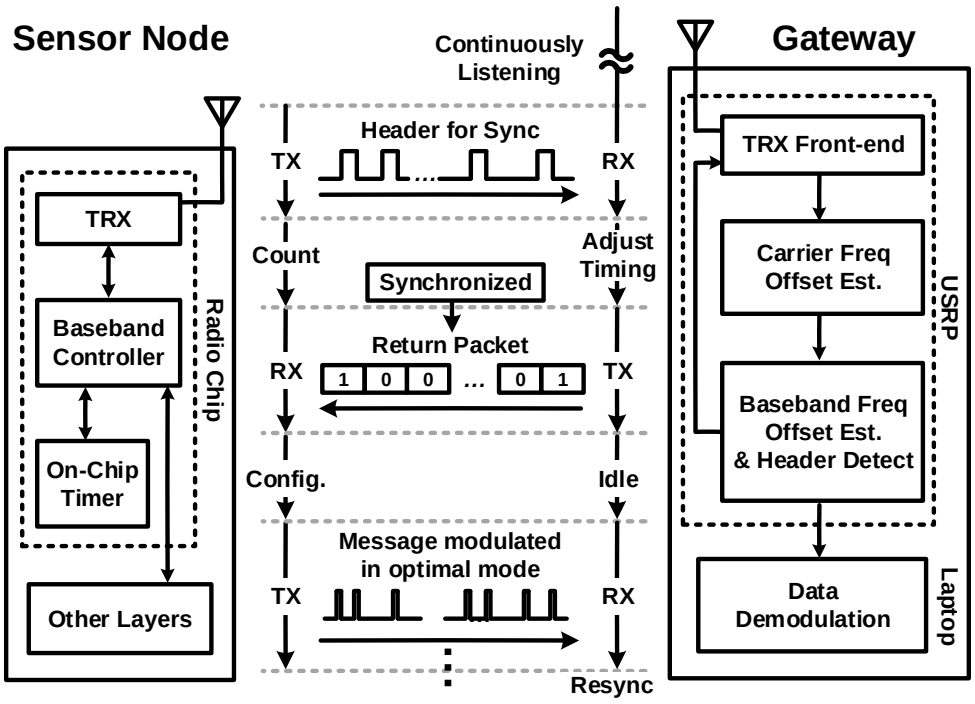


Figure 2.10: Adaptive sensor-initiation synchronization communication protocol

real-time gateway realized on the USRP [100] platform has excellent receiver sensitivity, high transmitter power, and abundant FPGA resources for digital signal processing. In the proposed sensor initiating protocol, the sensor node is mostly in sleep in order to save energy, while the gateway receiver is always listening to the channel to find connection messages initiated by nearby sensor nodes. Extending the concept originally proposed in [90], we demonstrate *real-time bi-directional communication* between mm-scale sensor nodes and an USRP based gateway.

2.4.1 Sensor Initiation Communication

Synchronization between the mm-scale sensor node and the gateway is entirely performed on the gateway. It is gateway's responsibility to track and adapt to the baseband and carrier frequency offset of each sensor node. The gateway analyzes the channel quality and send configuration commands to the sensor node with optimal

modulation settings, enabling dynamic *link adaptation*. Figure 2.10 shows the timing diagram of the protocol.

The sensor node transmitter supports convolutional codes with variable coding rates of 4, 3, 2, 1, 1/2, 1/3, and 1/4. The coding rate is equivalent to the number of information bits conveyed by a single pulse. Adaptive modulation parameters supported by the system include the pulse width (4 μs – 1 ms), coding rate, and the recharging time interval (0 – 32 ms).

The sensor node first initiates the communication by sending a header. The gateway is continuously listening to the channel until it finds a valid header. After the header is received, the gateway starts analyzing and calculating the carrier and baseband sampling frequency offset. The sensor node that initiated the communication enters the receive mode after a pre-defined waiting time measured by a ultra-low power timer in the sensor node. During this turn-around time, the gateway estimates and adjusts its baseband timing and carrier frequency to compensate the offset estimated from the sensor node packet. Hence the return packet is synchronized to each sensor node's local timer without explicit synchronization or header detection process performed on the sensor node. The demodulation process on the sensor node is greatly simplified as it starts demodulating symbols at a pre-defined time slot measured by the local low-power relaxation oscillator based timer [30].

2.4.2 Gateway Implementation

The main challenge in the gateway design is to identify the frequency and timing offsets with the sensor node in real-time. The TX-RX turn-around time of the sensor node imposes a strict latency constraint on this real-time synchronization process. The sensor node does not have a crystal oscillator. Instead, its baseband sampling clock is generated by a RC relaxation oscillator [30]. Its carrier frequency is determined by the inductance value of the 3D magnetic dipole antenna and the matching

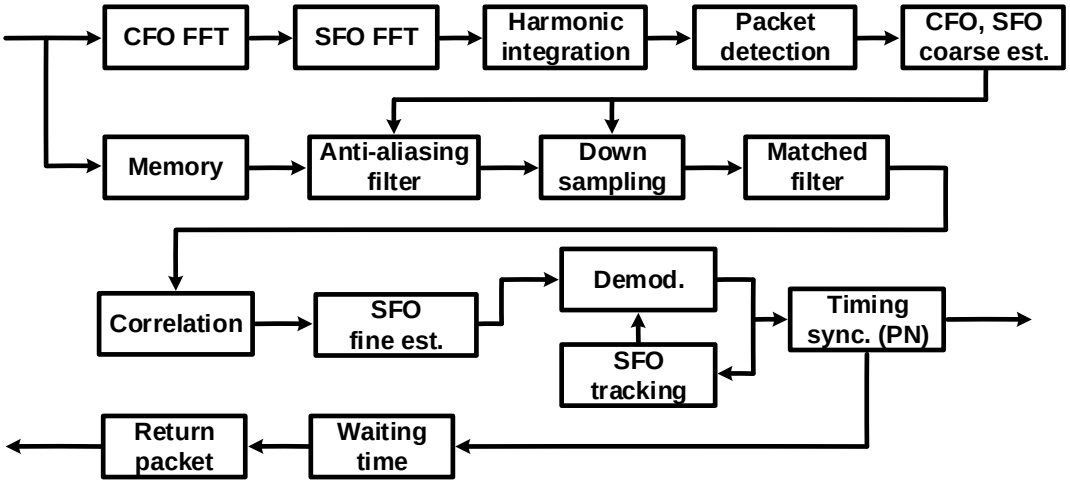


Figure 2.11: DSP datapath implemented on the gateway FPGA

on-/off-chip capacitors without a PLL. Thus, it is inevitable that the sensor node has significant baseband sampling frequency offset (SFO, up to 0.5%) as well as carrier frequency offset (CFO, up to 2%) affected by PVT variations. Calculating accurate SFO / CFO and compensating these offsets for the return packet in real-time is performed on the FPGA of the USRP platform. Figure 2.11 shows the detailed signal processing datapath implemented on the gateway's FPGA. The header from the sensor node always starts with an RF pulse train with a constant pulse interval. Thus, we propose a 2D-FFT based process that identifies the SFO and CFO at the same time. The incoming signal is first divided into multiple time domain signal frames, whose length is equivalent to the half of the pulse width. A 1D-FFT is performed on each signal frame and signal power is computed for each frequency offset bin, which correspond to a specific CFO hypotheses. A second FFT is performed on the sample power of frequency domain samples (output of the first FFT) that belong to that same bin (one specific CFO). This process is repeated for all frequency bins. Each bin of the second FFT output now corresponds to a specific SFO fundamental frequency. To accurately estimate the actual pulse repetition frequency of the header, we add

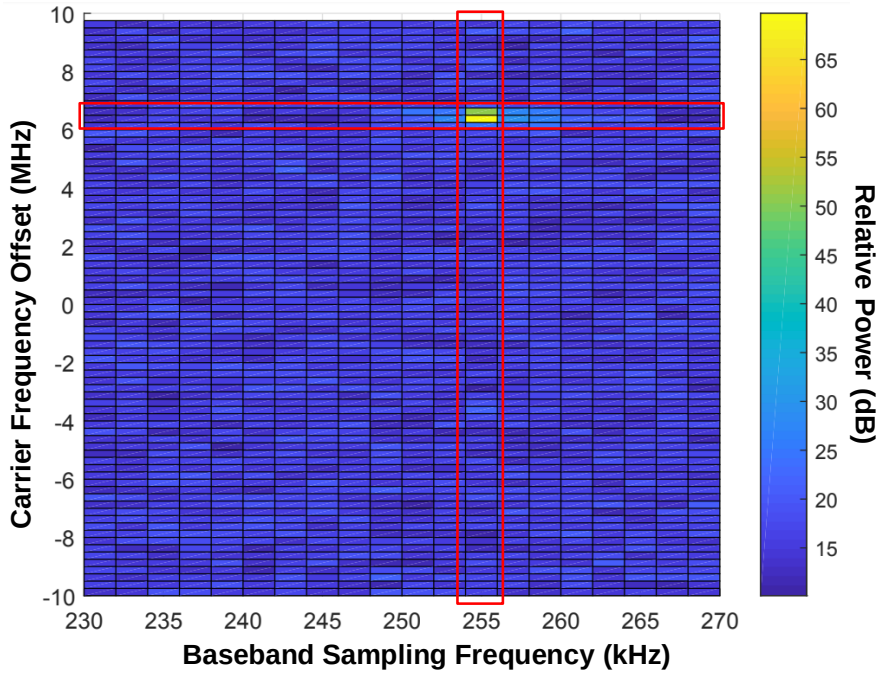


Figure 2.12: 2-D FFT map for sensor node CFO and baseband clock frequency evaluation

the power of all harmonic frequency bins corresponding to a specific fundamental frequency. Figure 2.12 shows an example of the 2D-FFT harmonic integration output from the header processing, where the y-axis corresponds to the CFO bin and x-axis is the SFO fundamental frequency hypothesis. By finding the maximum power from the 2D-FFT result, the gateway identifies the SFO as well as the CFO at the same time. The CFO FFT resolution is inversely proportional to the header pulse width, which is 1–250 kHz in our system. Figure 2.12 is the result for 6.5MHz CFO and 5kHz SFO from the 915MHz and 250kHz ideal carrier and sampling frequencies. After the 2D-FFT process for header detection, the gateway keeps tracking SFO during data payload demodulation to eliminate residual SFO and to mitigate the time-drifting offset. At the end of the payload demodulation, the final SFO is applied to calculate the return packet transmission time and its symbol/sampling rate.

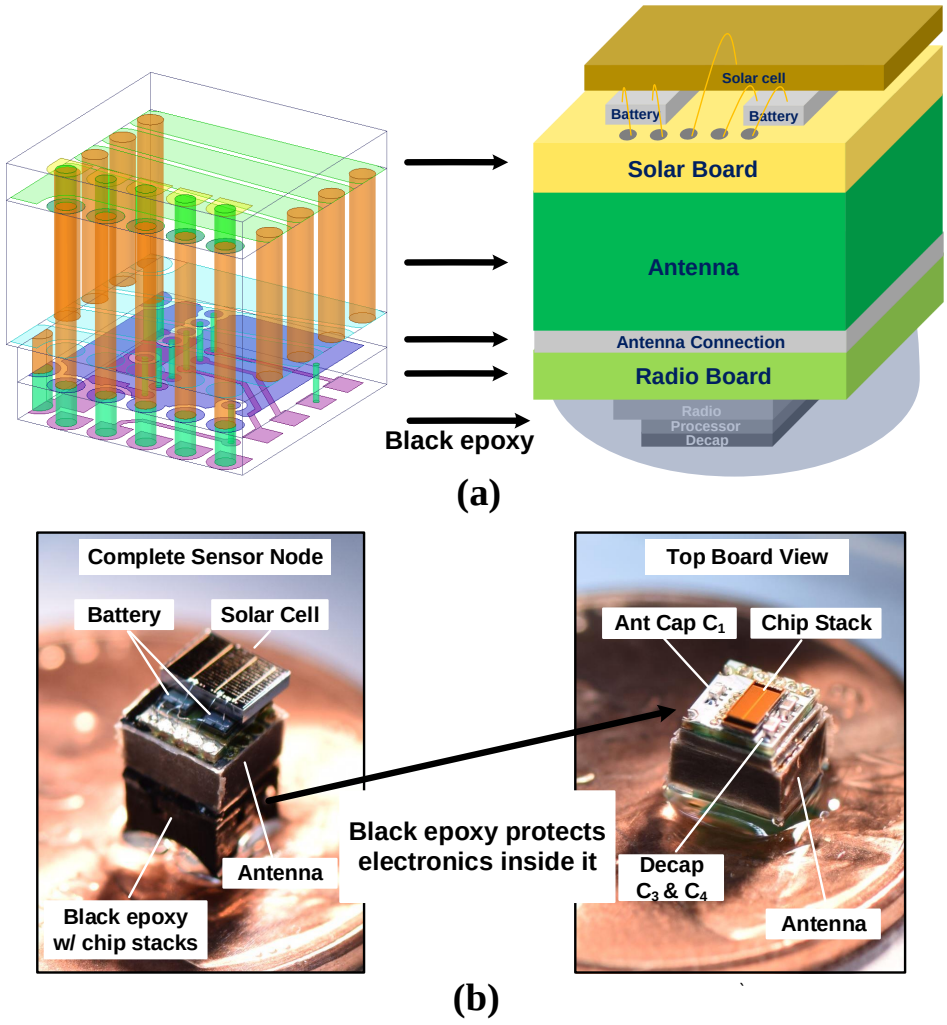


Figure 2.13: Radio system integration includes four boards, two 2Ah thin-film batteries, AlGaAs mm-scale solar cell, processor, decap, and radio chip

2.5 Measurement Results

2.5.1 System Integration

Figure 2.13(a) shows the system integration diagram. The radio system integrates 4 custom boards connected with vias. From the top to the bottom, it shows the solar board, antenna, antenna connection board, and radio board. The solar board is used to mount batteries and the PV cell, which are connected to the radio board with five through-hole vias. The antenna connection board is used to separate the ground plane

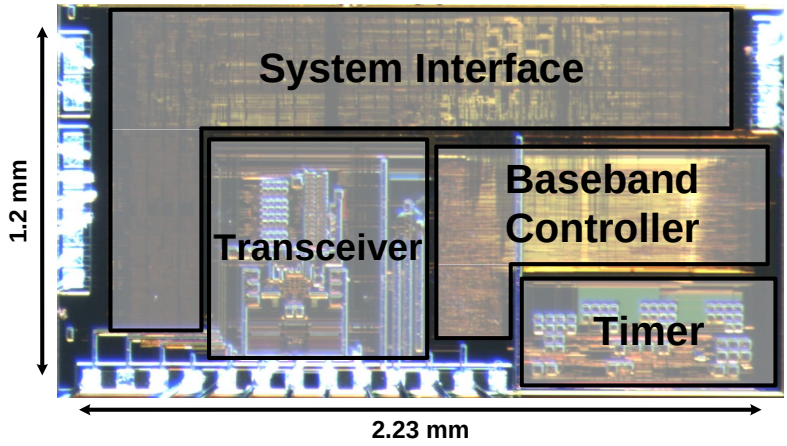


Figure 2.14: Radio die photo in 180 nm CMOS

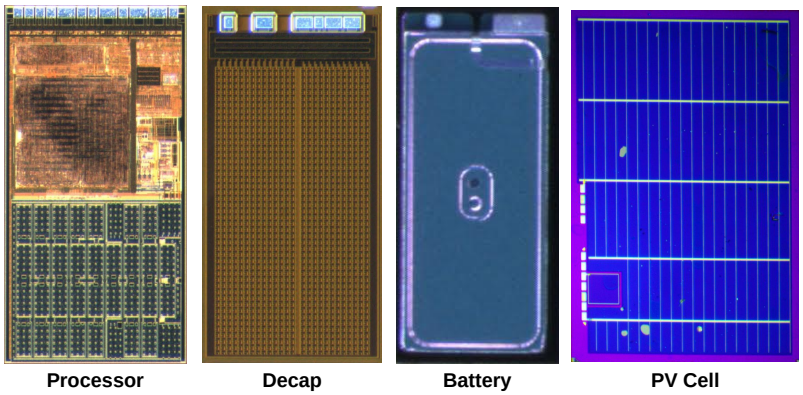


Figure 2.15: Other chips in the system

from the radio board and to avoid radiation efficiency degradation of the 3D antenna. Chips are stacked and mounted to the radio board. The system has a total of three off-chip capacitors: two 1 μF decaps and one antenna tuning cap. As Figure 2.13 shows, electronic components are directly stacked on top of the 3D magnetic dipole antenna. This is a significant advantage over the electric dipole antenna, which usually requires a certain keep out area to maintain radiation performance. We apply black epoxy to cover the chip stack because ultra-low power chips are highly sensitive to light. The final system has two thin-film batteries and one PV cell on the solar board which is clear epoxy coated to allow energy harvesting as shown in Figure 2.13(b).

Figure 2.14 is the die photo of the radio chip taped out in 180 nm CMOS. Fig-

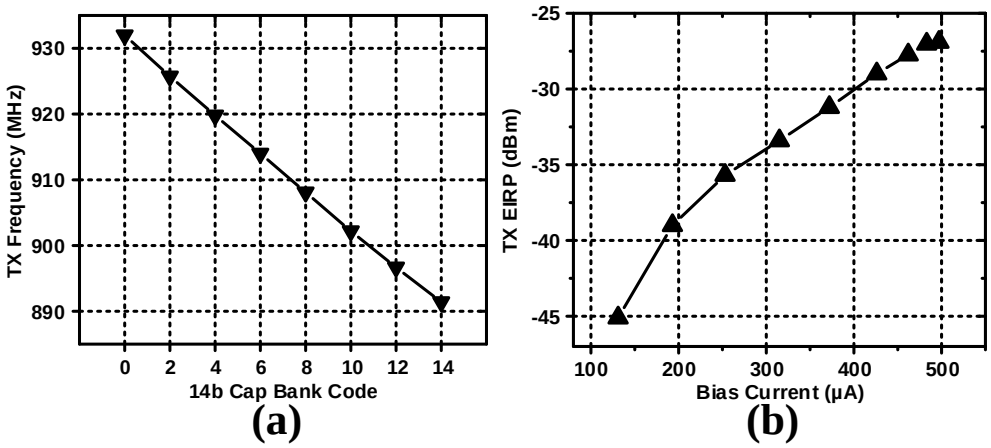


Figure 2.16: The transmitter performance (a) Tuning range (b)EIRP versus bias current

ure 2.15 shows other chips integrated into the system including the processor chip, decap chip, 2 μAh thin-film batteries, and AlGaAs PV cell.

2.5.2 Sensor Node Transmitter Performance

Figure 2.16(a) shows the carrier frequency tuning range of the transmitter. The x-axis is the tuning thermometer code and the y-axis is the carrier frequency. We use on-chip capacitor banks for tuning. It has 14 tuning bits with a 40 MHz tuning range. Figure 2.16(b) is the measured EIRP as a function of the transmitter bias current. The maximum EIRP including the antenna gain was measured at -26.9 dBm with 500μA bias current. The peak instantaneous power consumption for pulse transmission is 2 mW from 4V. The average power consumption for packet transmission is 60.6μW at 7.3kbps data rate using 4 μs pulse width, 128 μs recharging time, and a binary PPM coding rate of 1.

Figure 2.17 shows the carrier frequency drift with temperature from 0 to 60 degree Celsius. We did an experiment with two different antenna PCB materials (Rogers 5880/4003). The main reason for frequency drift is temperature-dependent physical expansion of the antenna that significantly changes the equivalent inductance. The

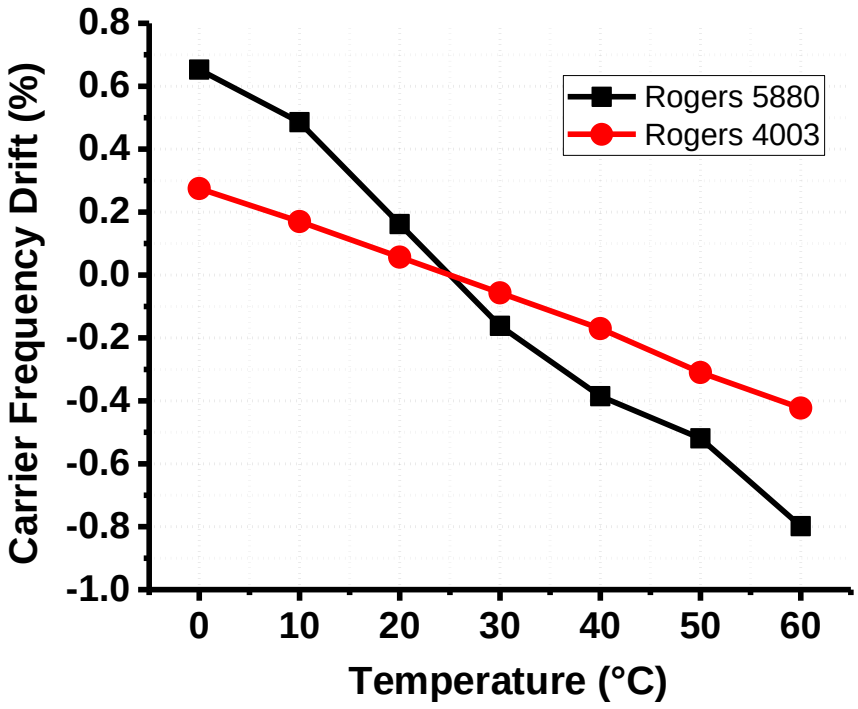


Figure 2.17: Carrier frequency drift with temperature in different antenna material (normalized to 25 degree Celsius)

result shows a <1% frequency drift across temperature, which can be reduced by using a more rigid PCB material such as Rogers 4003. This carrier frequency drift range is rather significant compared to a conventional system with a PLL. However the proposed system can successfully mitigate this issue using the real-time CFO tracking technique implemented on the gateway.

2.5.3 Sensor Node Receiver Performance

Figure 2.18 shows the sensitivity as a function of the Q-enhanced amplifier bias current. Because the front-end is co-designed with the antenna and not impedance-matched to 50Ω, the receiver sensitivity cannot be measured via a wired test. Therefore, we measured sensitivity wirelessly via turn-around communication with the gateway and by measuring the minimum RX signal power level (monitored at a reference antenna next to the sensor node) at which the sensor node fails to demodulate the

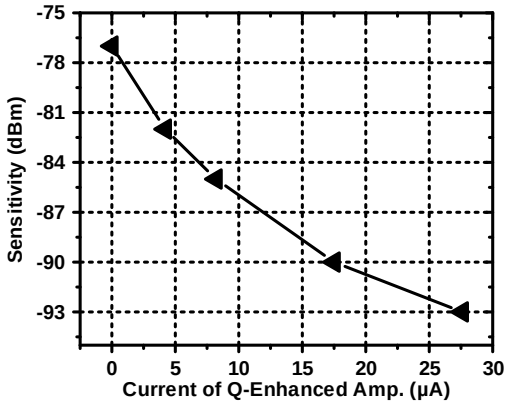


Figure 2.18: Sensitivity at 10^{-3} BER versus bias current of QEA

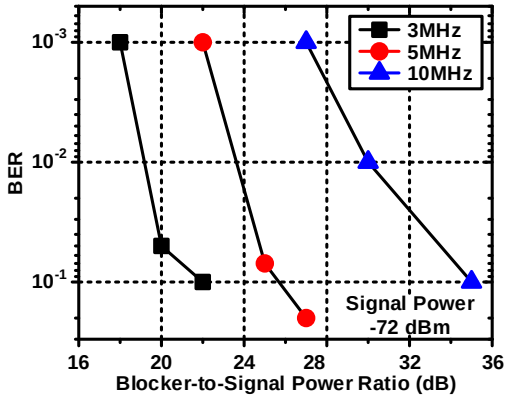


Figure 2.19: Blocker tolerance at different frequency offset

return packet from the gateway. The sensitivity was measured at -93 dBm for 30kbps data rate with 10^{-3} BER.

Because the receiver demodulates the binary PPM by comparing relative power difference between consecutive pulse positions, a single-tone unmodulated blocker does not strongly degrade the receiver performance. Hence an interference test was conducted with a pulse position modulated blocker with carrier frequency offsets of 3MHz, 5MHz and 10MHz as shown in Figure 2.19. The system exhibits good blocker tolerance of at least 20 dB rejection (at 10^{-1} BER) for a modulated blocker that is $\geq$ 3MHz away thanks to the highly band-selective Q-enhanced amplifier.

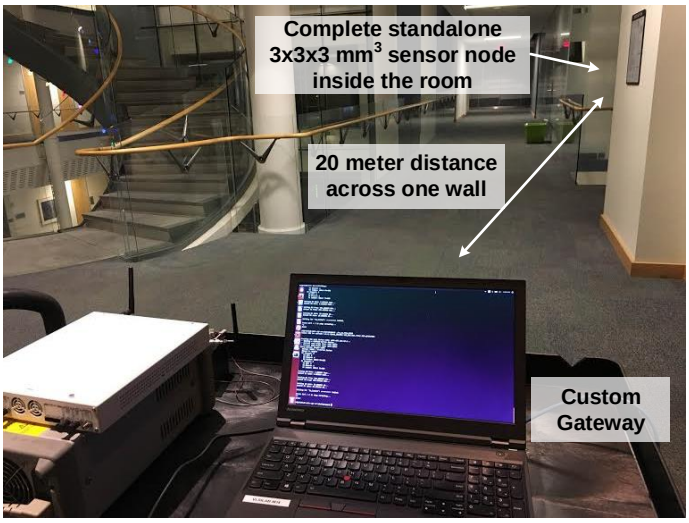


Figure 2.20: Indoor NLOS testing setup of the system

2.5.4 System Measurement

Figure 2.20 shows the system setup for the indoor NLOS communication field trials. The sensor node is inside the room and the communication to the gateway is reliably established at a $\geq$ 20 meter distance in a NLOS condition. The link distance can be increased to >30 m (limited by measurement set up) in LOS conditions.It must be noted that long wires attached to a mm-scale system can act as RF antennas and unintentionally boost the radiated power level. Thus we conducted experiments with completely standalone sensor nodes without any wire attached for the link distance measurement. In Figure 2.21, wireless traffic was captured on an additional USRP device monitoring the channel. Uplink communication is initiated by sparse pulses from the sensor node and the return packet from the gateway is immediately followed by the end of the uplink message.

Figure 2.22 shows an internal sensor node control signal and the rectifier output signal captured on an oscilloscope. From Figure 2.22, it is confirmed that the timing of the sensor node demodulation and the symbols from the gateway are well synchronized. The wireless link distance is limited by the uplink (sensor to gateway) when the

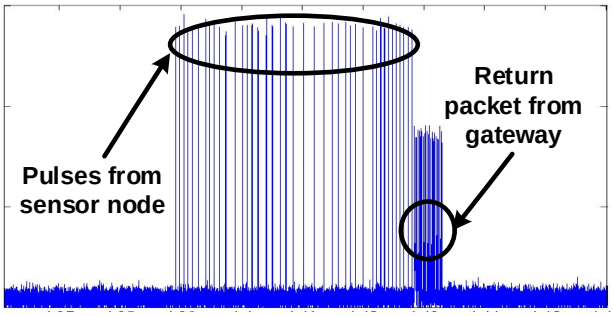


Figure 2.21: Sensor node-gateway communication channel monitoring

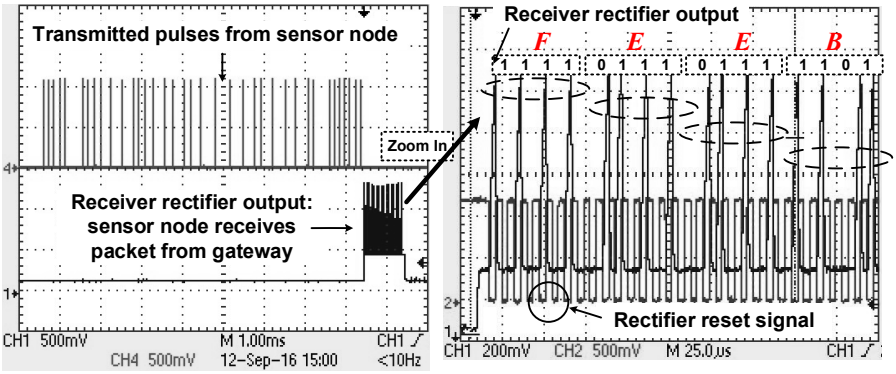


Figure 2.22: Transceiver control signal and received return packet (0xBEEF in hex) on sensor node

gateway is allowed to transmit the downlink message with 30 dBm power. We have validated that the gateway can correctly and reliably demodulate uplink messages from the sensor node in realistic (uncontrolled) channels as shown in Figure 2.23.

To avoid strong interference, the sensor node in Figure 2.23 initiates the uplink communication with frequency-hopping among three channels. The gateway monitors and blocks (or disables) channels where strong interference reside so that the gateway does not miss actual packets from the sensor node while processing false triggers initiated by interference signals. Table 2.1 summarizes the performance of each module in the system and provides a comparison with related prior work. This work is done collaboratively with my colleague Yao Shi, who wrote the finite state machine code in the radio chip.

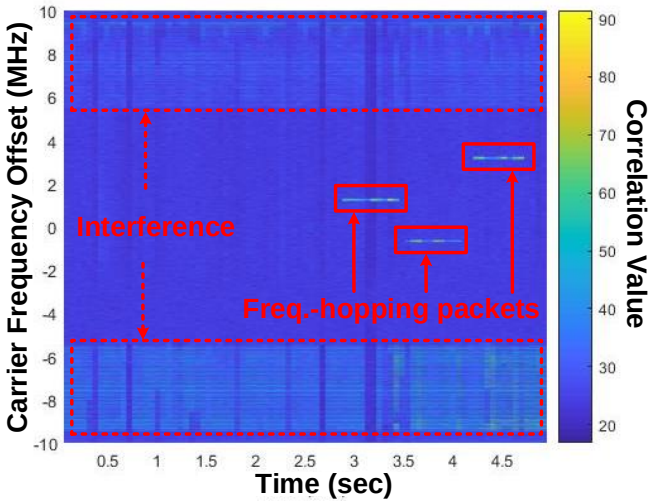


Figure 2.23: A 20 MHz bandwidth spectrogram snapshot of the channel

		This Work	M. Tabesh, JSSC 2015	J. L. Bohorquez, JSSC 2009
Technology		180 nm	65 nm	90 nm
Overall Dimension		3x3x3 mm^3 Complete Sensor Node (incl. Radio Chip + 3D Ant.)	3.7x1.2 mm^2 Radio Chip + Integrated Ant.	2x1 mm^2 Radio Chip (not incl. Loop Ant.)
Antenna		3x3x2 mm^3 3D Magnetic Dipole Antenna	Integrated Antenna	2.3x2.4 cm^2 Loop antenna
Carrier Frequency		915 MHz (TRX)	60GHz (TX) 24GHz (RX)	402-405MHz (TRX)
Measured Range		20m (NLOS) / >30m (LOS)	50 cm	N/A
TX	EIRP (Tone) Testing Method	-26.9 dBm Wireless Testing Incl. 3x3x2 mm^3 Ant.	N/A	-37.4 dBm **** Wireless Testing Incl. 2.3x2.4 cm^2 Ant.
	Peak Power (Tone)	2 mW	11mW **	350 µW
	Efficiency	14.8% *	N/A	N/A
	Modulation	M-ary Pulse-Pos. Mod.	Multi. Pulse-Pos. Mod.	MSK
	Average Power	60.6 µW	N/A	350 µW
	Data Rate	30bps - 30.3kbps	1.2Mbps - 12Mbps	120 kbps
RX	Technique	Q-Enhanced Amplifier	RFID RX	Super-Regnerative
	Modulation	Binary Pulse-Pos. Mod.	Pulse-Pause Mod.	Sync. OOK
	Sensitivity	-93 dBm	-10.5 dBm	-99 dBm
	Testing Method	Wireless Testing Incl. 3x3x2 mm^3 Ant.	Wired Testing Signal Gen. as Input	Wired Testing Signal Gen. as Input
	Power	1.85 mW	1.5 µW ***	400 µW
	Data Rate	7.8kbps - 62.5kbps	6.5 Mbps	40 kbps

* Calculated based on measured results: -26.9dBm EIRP, 2mW TX power, antenna eff. 0.46% and directivity 1.5
** Calculated based on simulated results: 250pC total charge for 3 pulses (width 680ps) from 0.9V supply
*** Calculated based on measured results: -48dBm received power at 20 cm away at 406MHz
**** Measured stand-by power reported

Table 2.1: Comparison with recent work in millimeter-scale radio

CHAPTER III

A 4x4x4 mm^3 Fully Integrated Sensor-to-Sensor Radio using Carrier Frequency Interlocking IF Receiver with -94 dBm Sensitivity

3.1 Introduction

Newly emerging Internet of Things (IoT) applications, such as agricultural monitoring, smart cities and ubiquitous beacon services, require ultra-low power (ULP) platforms of cm- and even mm-scales. Although there is increasing interest in sensor-to-sensor mesh networks, such as the new Bluetooth v5.0 standard, prior work in mm-scale ULP wireless communication systems mostly utilize a sensor-to-gateway topology (star-network) as shown in Section 2.1 and [22]. Millimeter-scale dimensioned systems exacerbate the challenges in sensor-to-sensor transceiver design, including: 1) accurate timing and carrier frequency synchronization among ULP transceiver nodes; 2) extremely stringent link budget stemming from the poor, electrically-small, antenna efficiency; and 3) inadequate battery capacity ($\sim$10 μAh) and instantaneous battery current capacity ($\sim$100 μA) due to mm-scale battery size and constrained by VDD fluctuation.

This work proposes a mm-scale fully self-contained radio system that supports sensor-to-sensor communication, enabling mesh network formation for mm-scale de-

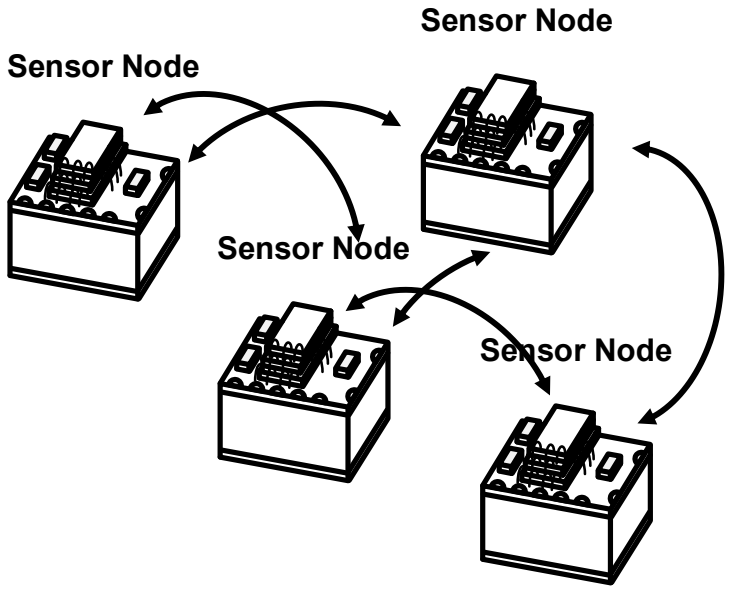


Figure 3.1: Sensor-to-sensor communication scheme

vices as shown in Figure 3.1. Conventional transceivers use a tens of MHz crystal oscillator (XO) as the frequency reference. However, their long start-up time ($\sim$1 ms) and the high power consumption of their crystal oscillator ($\sim$100 μW) and PLL ($\sim$1 mW) [112] make it incompatible with mm-size batteries. Instead, our proposed design uses only a 32.768-kHz real-time clock (RTC) with $<$ 10 nW power consumption to frequency lock a power oscillator merged with a high-Q 3D loop antenna, which doubles as a DCO and operates in open loop after locking. Hence, the proposed design combines the conventional PA and PLL and eliminates the power-hungry high frequency crystal and DCO, enabling a highly energy efficient TX design and reducing off-chip components. The locked power oscillator is then reused at the start of each RX operation to generate a calibration tone. To this tone a free-running ring oscillator (RO) is tuned such that the center of the down-converted RF signal aligns to the passband of the IF amplifier. This achieves TX-RX carrier frequency synchronization, which is critical in narrowband communication. It also eliminates

the need for explicit estimation of the bandpass IF amplifier center frequency, which significantly lowers the RX power consumption and simplifies the design. Combined with the reuse of TX power oscillator as a Q-enhanced amplifier (QEA) [51][32], we achieve good sensitivity of -94 dBm at the input of the -7.8 dBi (estimated from simulation) mm-scale antenna with 97 W power consumption. TX consumes 3.5 mW peak power for 125s pulse duration drawn from decaps and achieves -12.6 dBm EIRP. The complete system, including the proposed transceiver chip, high-Q antenna, 32 kHz crystal, Cortex-M0 processor and power management unit, is integrated within a 444 mm3 sensor platform and communicates at a data rate of 4 kbps.

3.2 Carrier Frequency Interlocking IF Receiver

Figure 3.2 shows our proposed radio architecture and the conventional scheme. Unlike conventional low-power receiver approaches such as direct conversion, low-IF, and uncertain-IF [77][85], the proposed architecture takes advantage of a high-Q antenna and TRX front-end sharing. A direct-conversion scheme is popular for its simplicity but suffers from flicker noise, DC offset, and LO leakage, making it hard to achieve good sensitivity [67]. A low-IF architecture has been widely used to address these issues, but it requires a high quality RF local oscillator (LO), which is very power hungry [78]. Recently, uncertain-IF architectures using a low-power unlocked LO were proposed where uncertain-IF is accommodated by increasing the IF amplifier bandwidth. However, widening the IF amplifier bandwidth to address IF uncertainty increases power and reduces SNR (by incorporating more noise), nullifying the benefit of narrowband communications to achieve superior sensitivity [77].

The proposed architecture instead uses a narrow band RX chain that combines the band-selective (Q$\sim$1000, bandwidth $\sim$2 MHz) QEA and a bandpass IF amplifier to obtain superior SNR than typical uncertain IF architectures while maintaining low power consumption. First the digitally-controlled power oscillator (DCPO) is

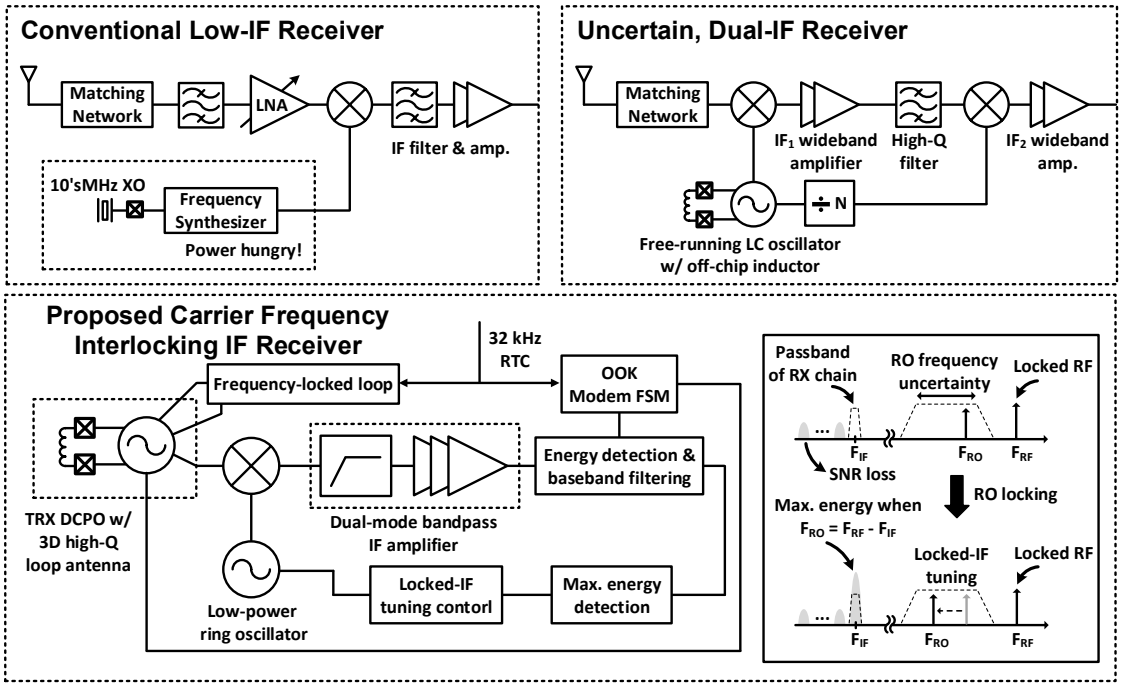


Figure 3.2: The proposed receiver architecture and comparison to other works

frequency-locked using the 32 kHz crystal for TX. The DCPO also serves as the RX front-end by implementing the QEA and provides the RF reference tone for calibration to align the down-converted IF signal to the passband of the IF amplifier in the receive chain. During this calibration, the frequency-locked DCPO signal (F_{RF}) is down-converted to IF (F_{IF}) by the RO frequency (F_{RO}) and passed through dual-mode bandpass IF amplifiers. A maximum energy detection loop then sets F_{RO} such that the bandpass IF amplifier output is maximized which ensures that the RO is tuned and F_{IF} is centered in the IF-amplifiers passband for maximum sensitivity. As a result, the IF amplifier bandwidth can be reduced. The proposed architecture preserves the high sensitivity while using a low-power RO as LO (Figure 3.2 bottom).

3.3 Link Budget Analysis and Antenna Simulation

3.3.1 Path Loss and Antenna Efficiency Analysis

To optimize the communication, link loss includes the proposed 3D magnetic dipole antenna has to be minimized. Unlike section 2.3, the symmetric link between sensor nodes will take double penalty of the antenna efficiency. As a result, the system link budget needs to be reevaluated. According to the indoor path loss model from International Telecommunication Union (ITU) that includes one layer of wall/floor which blocks the LOS between sensor nodes (typical case in indoor environment), the path loss equation can be written by Equation (3.1)[89].

$$L(F_c, d) = 20 \log_{10} \frac{4\pi F_c}{c} + N \log_{10} d + FL(F_c) \tag{3.1}$$

In Equation (3.1), $L(F_c, d)$ is the path loss in dB, F_c is carrier frequency in Hz, d is communication distance in meter, c is light speed, N is the distance power loss coefficient (for indoor environment, $N = 3$) and $FL(F_c)$ is floor loss depending on carrier frequency.

Since the mm-scale form factor antenna in sub-10 GHz is considered as electrically-small antenna, its impedance is mostly reactive (behaves as a capacitor or inductor) and the received electric field should be calculated using Equation (3.2)[12]. To get more insightful information to design the corresponding circuits, the induced received voltage on the antenna can be calculated in Equation (3.3), where l is the antenna dimension.

$$E = \sqrt{\frac{P_{transmit} \times G_{TX} \times 2 \times 377}{4\pi R^2}} \tag{3.2}$$

$$V = E \times k \times l^2, \quad k = \frac{2\pi}{\lambda} \tag{3.3}$$

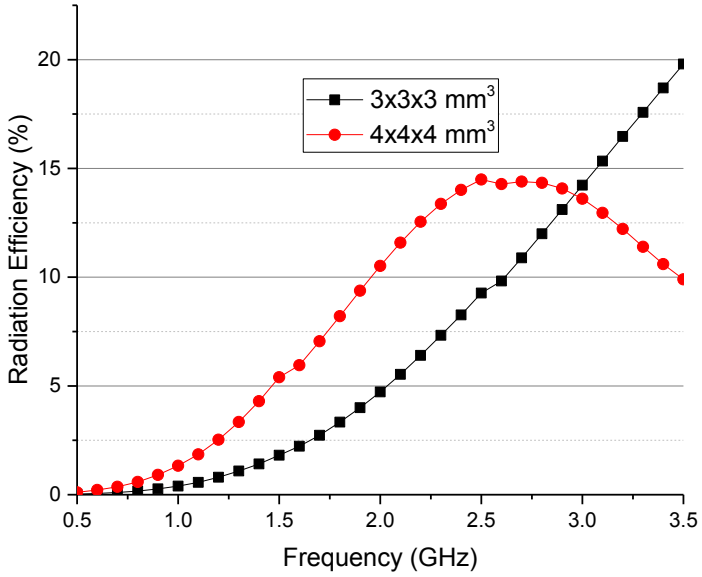


Figure 3.3: Simulated radiation efficiency for electrically-small loop antenna

The simulated radiation efficiency for both 3x3x3 and 4x4x4 mm^3 antennae are shown in Figure 3.3. The simulation result shows that there is a significant efficiency increase from 915 MHz to 2.4 GHz and the 4x4x4 mm^3 antenna can have 10% more efficiency. Since this is a loop structure, the antenna has inductive impedance and has finite self resonant frequency. As shown in Figure 3.3, the 4x4x4 mm^3 antenna has around 2.5 GHz self resonant frequency and the 3x3x3 mm^3 antenna's self resonant frequency is beyond 3.5 GHz. We chose the 4x4x4 mm^3 antenna in this design because we want to stay in 2.4 GHz ISM band.

Figure 3.4 shows the calculated link budget based on the simulated 4x4x4 mm^3 antenna radiation efficiency and Equation (3.2) (3.3). Assume one sensor node transmits at 100 μW (-10 dBm) power and the dipole antenna directivity is 1.5. The induced voltage on the received sensor node antenna at 7 meter distance is $\sim$ 3 μV which can be translated to $\sim$ -100 dBm power on a conventional 50 Ω antenna.

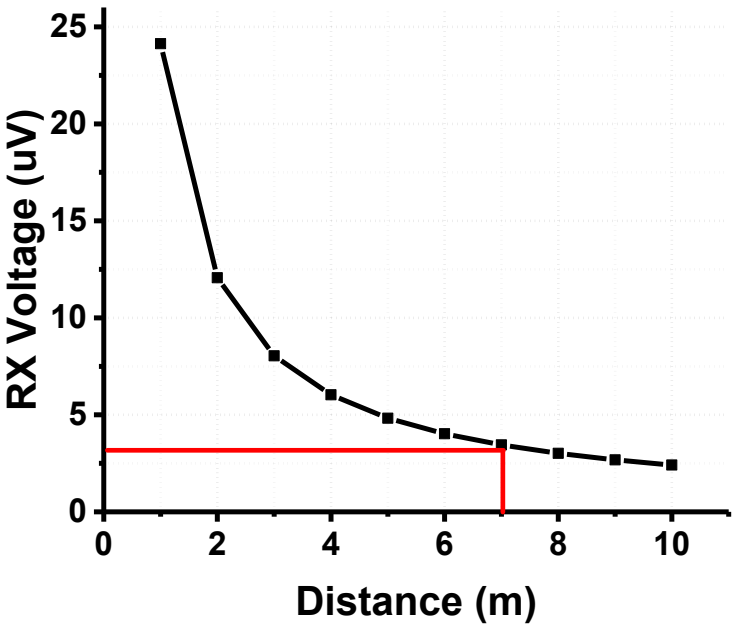


Figure 3.4: Link budget analysis based on 4x4x4 mm^3 antenna

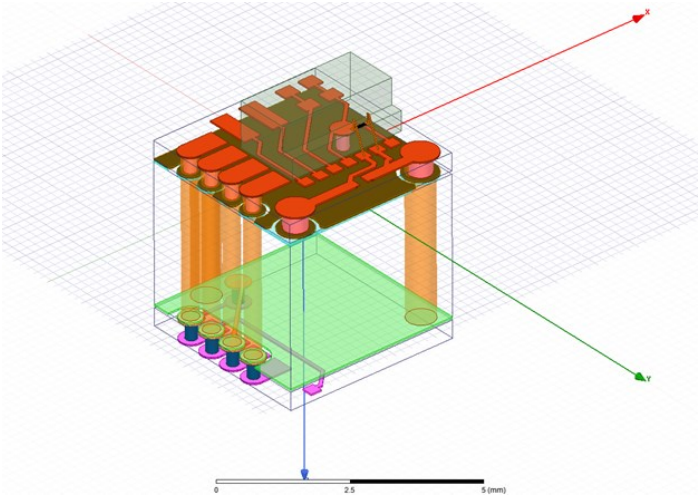


Figure 3.5: Antenna and other electronics simulation setup in HFSS

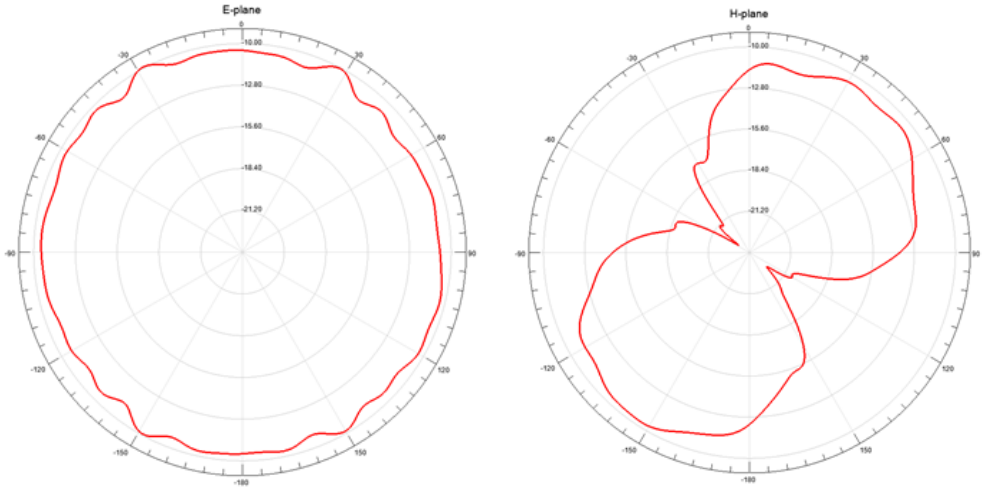


Figure 3.6: Simulated radiation pattern

3.3.2 Antenna & PCB Simulation

Since the antenna will be co-designed and integrated with other PCBs and electronic devices, we need to better understand the effect of other boards and wirebonds to the antenna radiation efficiency/pattern. As shown in Figure 3.5, the antenna is sandwiched between two other boards and we put some dummy electronic devices and wirebonds in the HFSS simulation. The simulated pattern is shown in Figure 3.6 and it indicates the antenna is an omnidirectional magnetic dipole with -10 dBi gain.

3.4 Transceiver Circuits Implementation

3.4.1 Transceiver Overview and System Timing

The DCPO uses a co-designed high-Q 3D loop antenna as the resonant component as explained in previous section 2.3.3, which lowers the power consumption in TX mode and also serves as a highly band-selective filter in RX mode (Figure 3.7). The

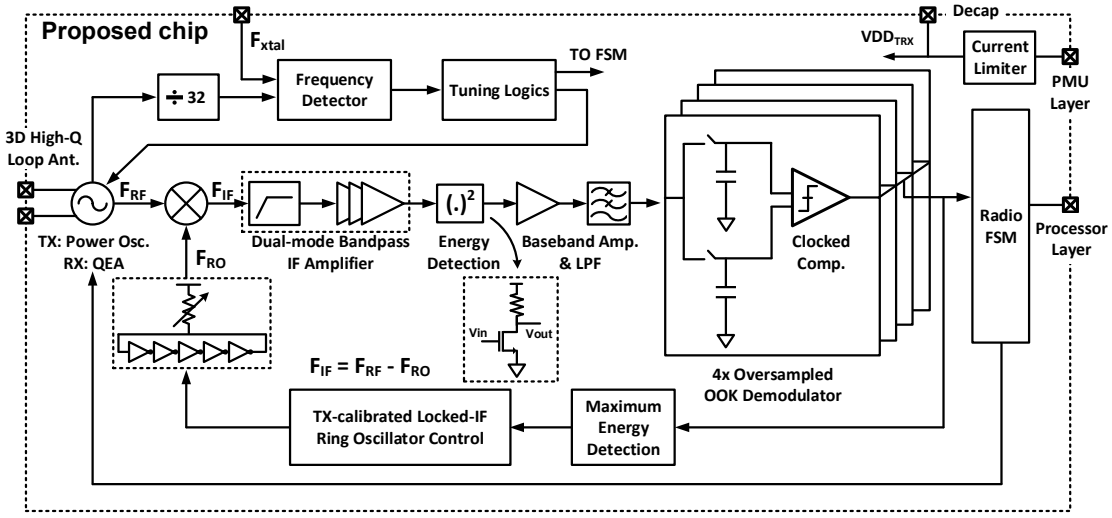


Figure 3.7: Details of the transceiver circuits

TX and RX front-ends share the same circuits with different bias conditions, resulting in naturally similar carrier frequency. Though there is still frequency difference results from non-linearity of capacitors, it was found to be small compared to the RX QEA bandwidth (2 MHz). The TX DCPO frequency calibration is performed first, followed by the RX interlocking IF tuning. Depending on the initial control setting, the TX DCPO frequency-locked loop (FLL) may require a long settling time at first due to the use of 32 kHz reference. However, once the initial calibrated frequency control word is stored in the processor, the radio will only need to fine-tune and update the setting each time before communicating. The self-calibration timing and multiple access scheme are also shown in Figure 3.8.

3.4.2 DCPO Front-End Design and Operation

During TX DCPO frequency locking, the DCPO cross-coupled transistors are biased with high current (∼850 A) to start the oscillation. The FLL is composed of a 32x divider, asynchronous counter, and frequency tuning logic as shown in Figure 3.9. The counter is clocked by a divided RTC (32.768/4 = 8.192 kHz) supplied

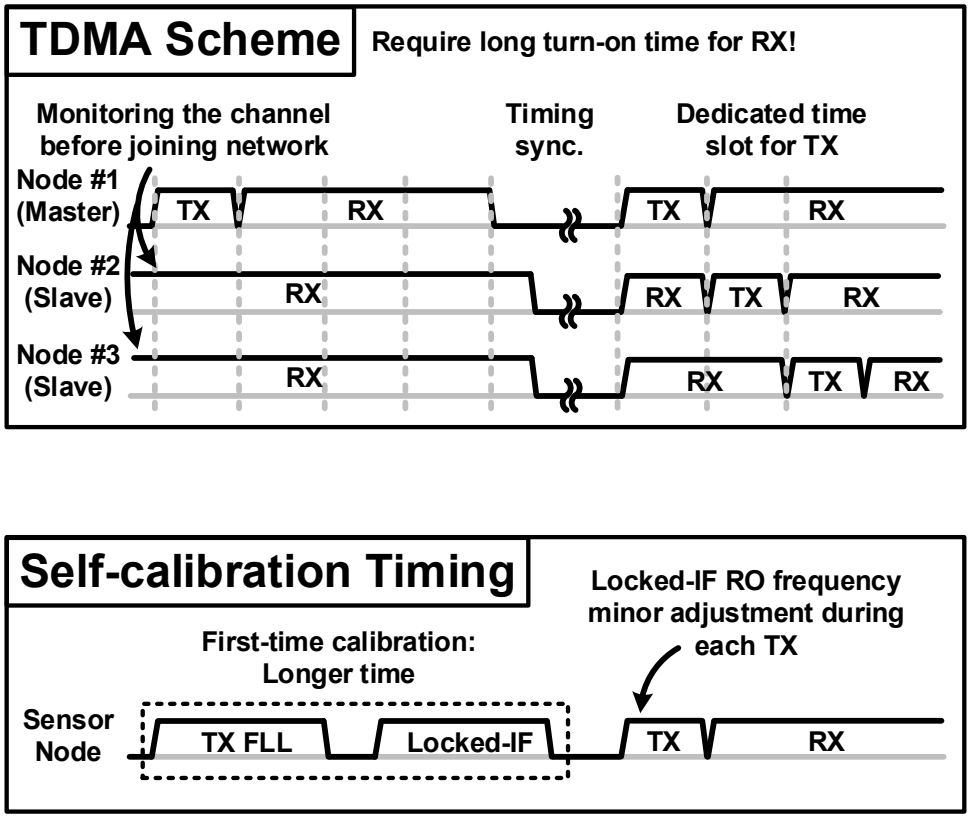


Figure 3.8: Calibration loop timing and the radio sensor node multiple access scheme

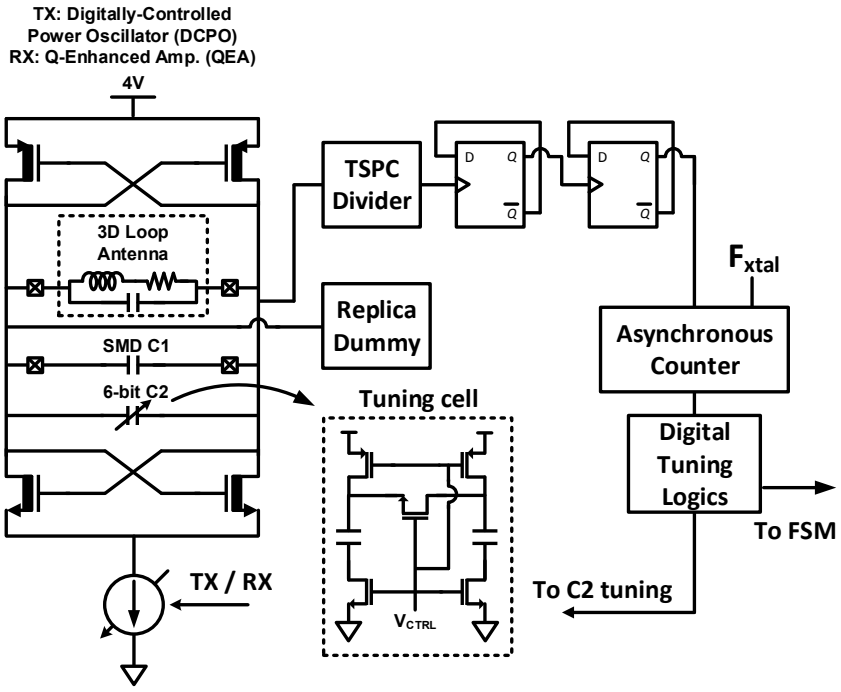


Figure 3.9: Transmitter frequency-locked loop using 32-kHz system real-time-clock

by the processor for high frequency resolution. It counts the number of divided RF signal transitions (∼75 MHz) and locks the frequency accordingly. Since the carrier frequency is set by the 3D loop antenna and the (mostly) off-chip capacitance, it does not have significant VDD dependency. Thus, the FLL is mainly for compensating the antenna and off-chip capacitor variations. In RX mode, the same cross-coupled pair is biased in the Q-enhanced region for boosting the Q value of the loop antenna to have a band-selective filter response and in-band voltage gain (62.7 dB, simulation). The targeted RF front-end filter bandwidth of the receiver chain is 2 MHz (Q $\sim$ 1000), meaning that the TX frequency synchronization should also be within 0.1% (Q $\sim$ 1000). The measured results shown in Figure 3.10 indicates that the FLL calibration can synchronize the carrier frequency to within 0.1% across 5 tested chips.

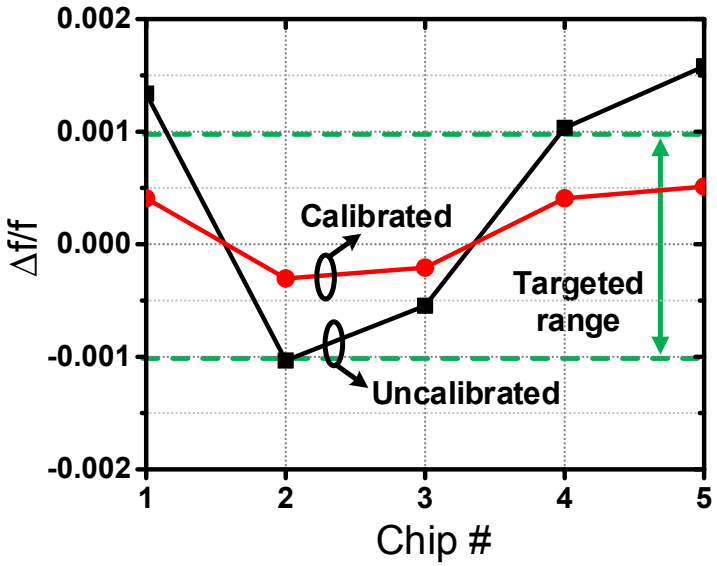


Figure 3.10: TX FLL measured results, showing it can lock the frequency within 0.1% error from chip-to-chip

3.4.3 Carrier Frequency Interlocking IF Receiver Designs

After the carrier frequency is locked, the radio starts IF calibration. The RX chain is turned on during the TX operation with the self-injected attenuated TX signal as shown in Figure 3.11. Because the input RF signal is strong (directly from the DCPO), the IF amplifiers were designed to have a calibration mode with 40dB less gain (Figure 3.12, left). This lowers power consumption during calibration and avoids saturation of the amplifier. The simulated results in Figure 3.12 show that both high and low gain modes have identical bandpass frequency response but different gains. We reuse the remainder of the RX chain (energy detector and comparator) to detect the output signal from the IF amplifiers and tune the RO frequency. The energy detector output is sampled with different RO frequency settings and compared to the prior output by reusing the data-demodulation comparator. This search continues until it finds the maximum output level at which point the amplifier passband is aligned with the RX IF signal down-converted from the DCPO TX signal. In the

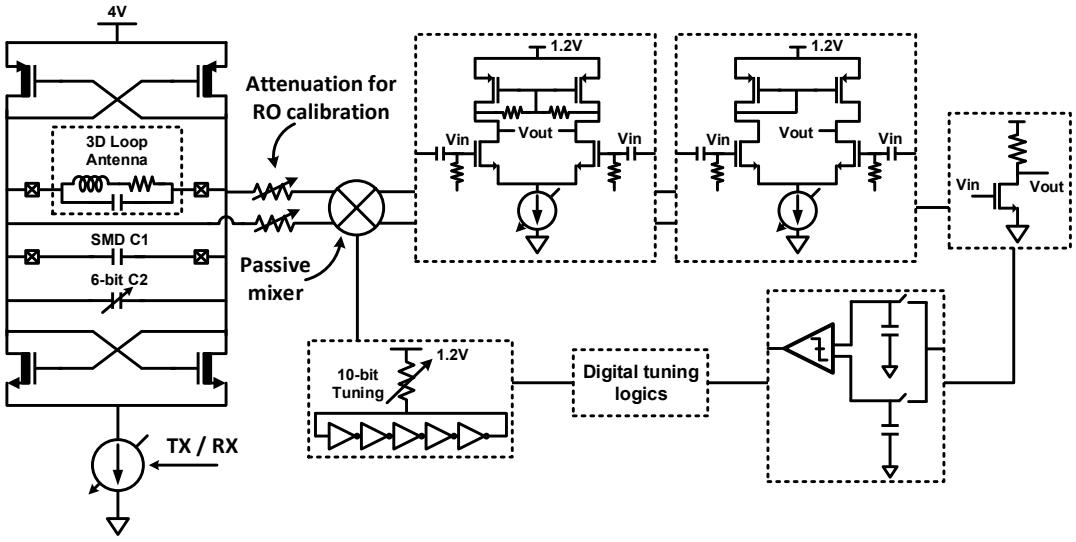


Figure 3.11: Reuse the RX chain with lower gain setting for RO tuning loop

mm-scale sensor node design, the VDD will fluctuate due to the limited battery and decap current and capacity. As a result, it is difficult to achieve a stable low-power RO frequency with a conventional design. Figure 3.12 shows the measured RO across VDD variation with and without the proposed TX-RX interlocking technique. The free-running RO frequency will deviate by more than 20% (100s MHz in GHz) when VDD varies from 1.4 V to 1.0 V. With the proposed locking calibration, the RO frequency is stable within 1% across VDD, meeting the bandwidth of the IF amplifier. When both DCPO and RO are tuned, data communication is performed using binary pulse position modulation (PPM) that compares relative symbol power levels at two different position, eliminating the need of an accurate reference voltage for optimal demodulation. The proposed chip supports time-division multiple access (TDMA) for node-to-node communication as shown in Figure 3.8. Each node is given a programmable time slot (ID) for collision-free transmission.

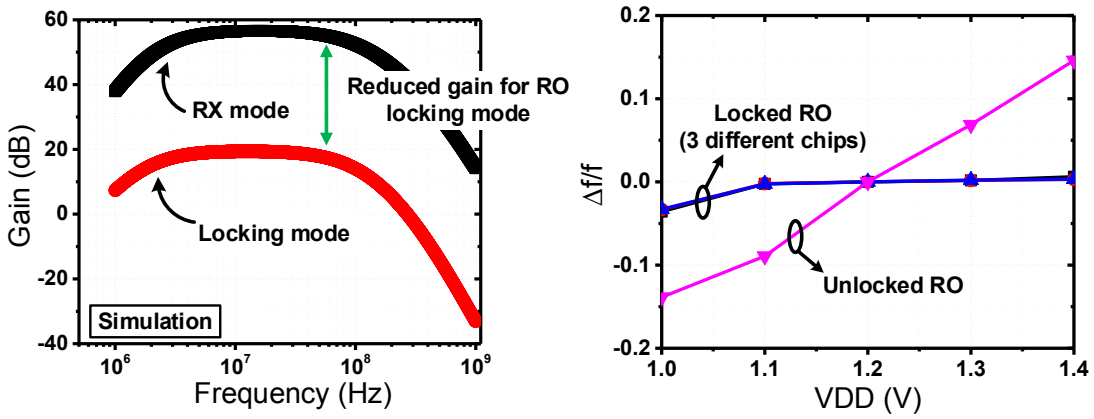


Figure 3.12: Dual-mode IF amplifier and RO locking measurement results

3.5 Chip Measurement and Radio System Evaluation

The transceiver chip was fabricated in MIFS 55-nm DDC CMOS and integrated with a custom designed antenna in 4x4x4 mm^3 form factor. Since this transceiver was co-designed with the antenna and was not matched to 50 ohm, its performance evaluation includes the mm-scale antenna gain (-7.8 dBi). The measurement setup and results are shown in Figure 3.13 and Figure 3.14. In TX mode, the EIRP of the sensor node transmitting a continuous tone was measured using a horn antenna (LB-530-NF) in an anechoic chamber which ranged from -18.9 to -12.6 dBm with 1.7 to 3.5 mW TX power consumption. The receiver has a sensitivity of -94 dBm measured at the input of a -7.8 dBi (simulation) mm-scale antenna for 10^{-3} BER at 4 kbps with 97 μW power consumption.

A measured time-domain waveform of wireless communication between two fully integrated nodes in Figure 3.15 validates TDMA based sensor-to-sensor communication. For measurement in Figure 3.15, the number of TDMA slots are pre-programmed to six. Node #1 (ID=3) transmits at the third time-slot and listens at all other time-slots. The same rule applies to node #2 (ID=6) that uses the sixth time-slot for TX. The zoomed-in plot in Figure 3.15 shows that the two mm-scale

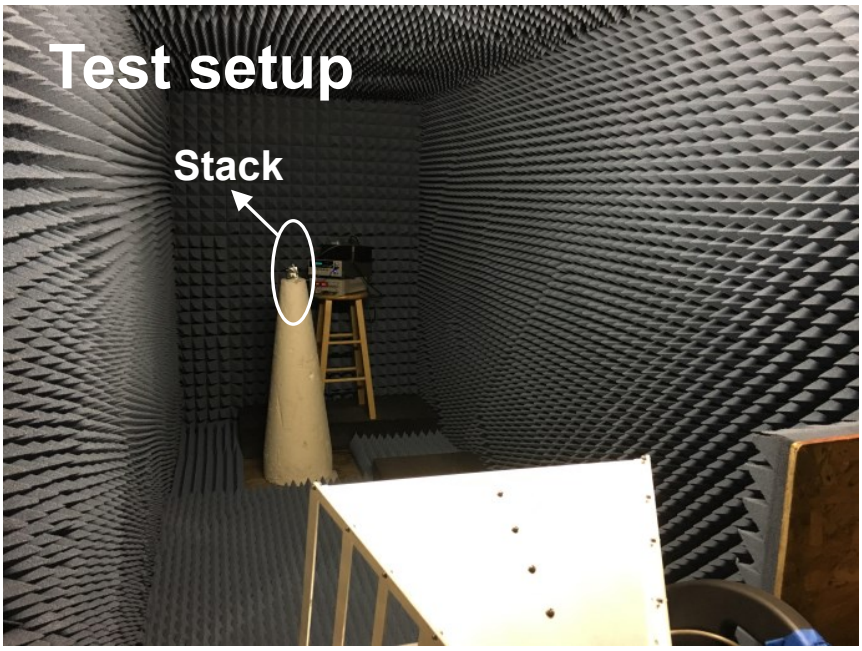


Figure 3.13: Testing setup in anechoic chamber

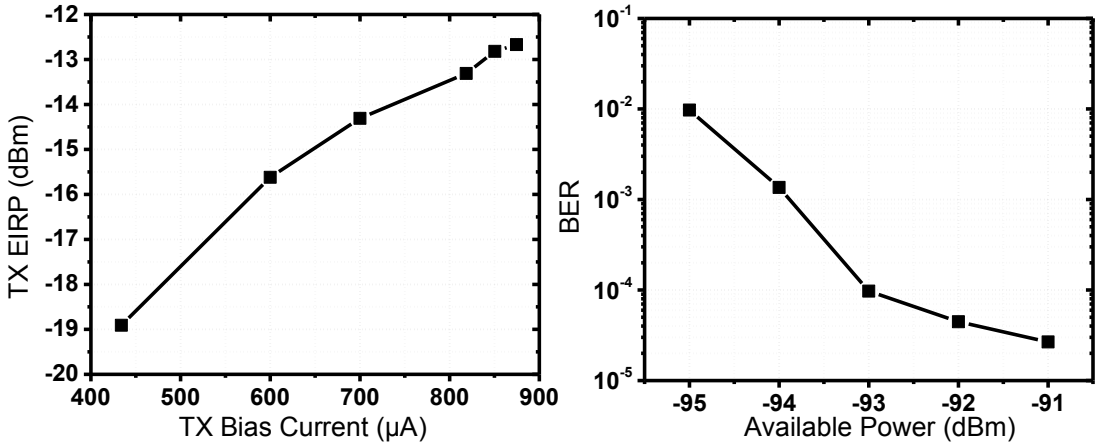


Figure 3.14: Measured transceiver chip (w/ antenna) EIRP and sensitivity

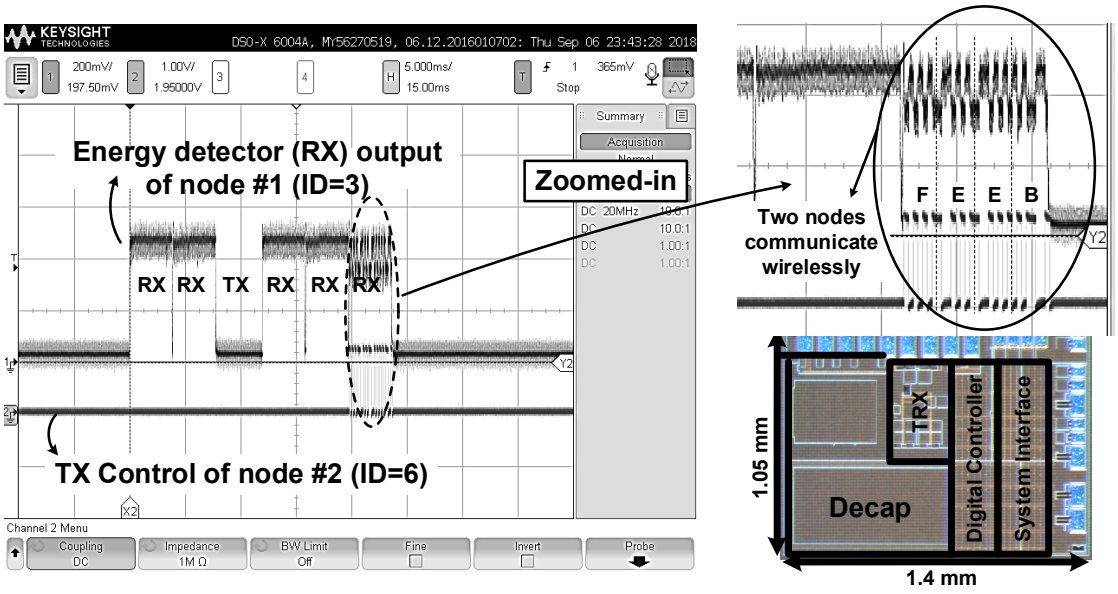


Figure 3.15: Measured time domain sensor-to-sensor communication waveform using the fully integrated radio system and the transceiver chip micrograph

nodes synchronously transmit and receive using proper time slot, thus establishing successful communication links. Figure 3.16 shows the fully integrated system that integrates a transceiver chip, antenna, power management unit, and baseband processor for wireless node-to-node communication measurements.

3.6 Summary

Challenges in mm-scale node-to-node communication includes electrically small antenna (low radiation efficiency, difficult to impedance match), frequency / timing synchronization and stringent power / energy budget (limited peak current and battery capacity). In this chapter, we present a 4x4x4 mm^3 fully stand-alone radio system that integrates a RF transceiver chip, antenna, power management unit and baseband processor with a new carrier frequency interlocking IF receiver architecture for low-power and high sensitivity node-to-node mesh networks. It is shown that when ITU model is utilized for NLOS communication in indoor environment and symmetric link

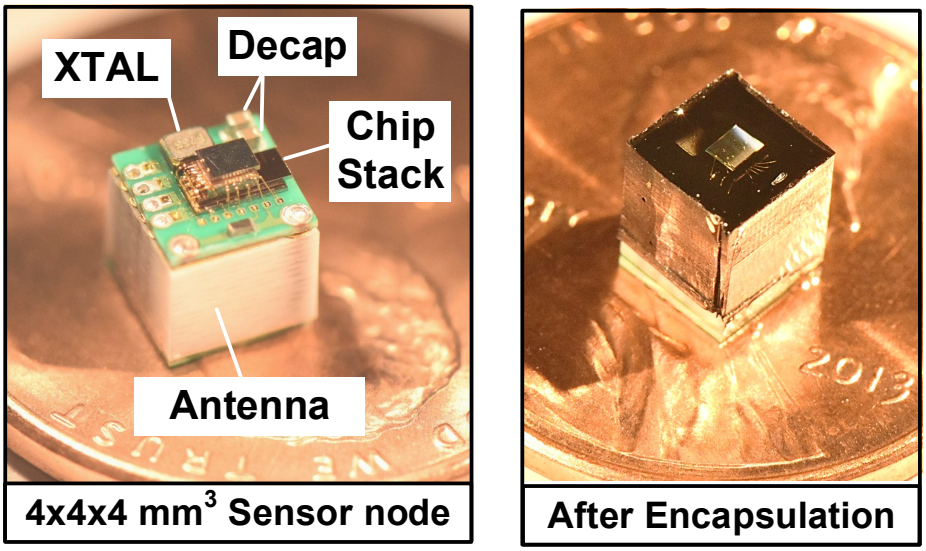


Figure 3.16: The fully integrated radio system including transceiver, processor, PMU, antenna, XTAL, and decaps

is considered, the carrier frequency of 2.4 GHz and larger antenna size are required for a reasonable (few meters) link distance. The proposed mm-scale system demonstrates node-to-node communication with -12.6 dBm EIRP for TX and -94 dBm sensitivity (at the input of a -7.8 dBi antenna) with 97 μW power consumption for RX, enabling the feasibility of sensor-to-sensor mesh networks. Table 3.1 summarizes the overall performance and compares it to other low-power radio systems.

		This work	L-.X Chuo, ISSCC 2017	C. Salazar, ISSCC 2015	J.-S. Lee, ISSCC 2015
Technology		**55 nm**	180 nm	65 nm	65nm
System Form Factor		**4x4x4 mm^3**	3x3x3 mm^3	4.6x4.6 mm^2 Receiver chip only	1.3x0.9 mm^2 Receiver chip only
# of off-chip components		**5 (Antenna, xtal, decaps)**	4 (Antenna, decaps)	11 (Inductors, decaps)	3 (Inductors)
Frequency		**2.4 GHz**	900 MHz	2.4 GHz	2.4 GHz
Sensor-to-Sensor Communication?		**Yes**	No	No	No
RX	Technique	**Carrier Frequency Interlocking IF**	Tuned-RF	Dual Uncertain-IF	RX-based FLL
	Modulation	**Binary PPM**	Binary PPM	OOK	OOK
	Power Consumption	**97 µW (81 µW @ 1V 16 µW @ 4V (QEA))**	1850 µW @ 2V	99 µW @ 0.5V	227 µW @ 0.6V
	Data Rate	**4 kbps**	7.8 kbps – 62.5 kbps	10 kbps	1 Mbps
	Sensitivity*	**-94 dBm (@ input of -7.8 dBi antenna)**	-93 dBm (@ input of -23.4 dBi antenna)	-97 dBm (@ input of AFE)	-83 dBm (@ input of AFE)
TX	Technique	**RTC-FLL**	Free-running	N/A (RX only)	N/A (RX only)
	Max. EIRP	**-12.6 dBm**	-26.9 dBm		
	Power Consumption	**3.5 mW @ 4V**	2 mW @ 4V		
	Data Rate	**4 kbps**	30 bps – 30.3 kbps		

Table 3.1: Comparison with prior work

CHAPTER IV

RF-Echo: A Non-Line-of-Sight Indoor Localization System Using a Low-Power Active RF Reflector ASIC Tag and Neural Network ToF Estimation

4.1 Introduction

Long-range low-power NLOS indoor localization can enable a host of location-aware Internet-of-Things (IoT) applications. Indoor navigation of public safety officials inside a building is a primary example. The localization tag built in wearable devices would significantly enhance the effectiveness of emergency evacuation, search and rescue operations. Intelligent warehouses and factories can be realized by tracking accurate locations of pallets, equipment, robots, and people in real-time to eliminate potential safety hazards while maximizing logistics efficiency. In hospitals, tracking of equipment, patients, and personnel can identify and eliminate infectious vectors, addressing a major health care issue. We envision ubiquitous localization-ready wireless tags to enable real-time tracking and logging of medical personnel / equipment interaction with patients.

A mobile tag for everyday IoT applications must be small, low power, low cost, and rapidly deployable without heavy infrastructure investment. We target a stringent power budget of $<100\mu$W in average (duty-cycled) and <100 mW peak power to fully

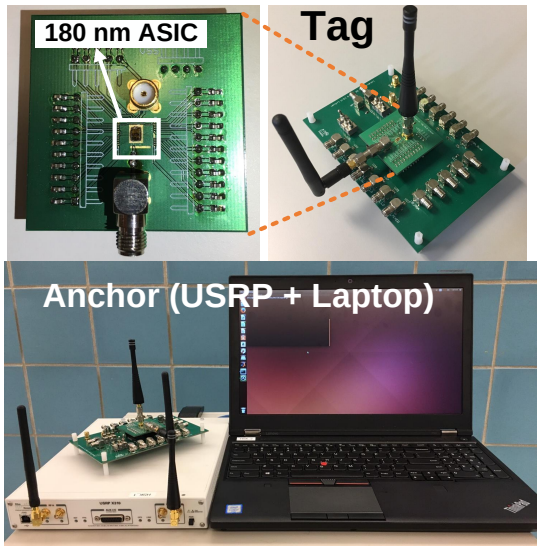


Figure 4.1: RF-Echo: The tag ASIC fabricated in 180nm CMOS (top), and the USRP based anchor (bottom)

integrate the solution in a centimeter-scale wearable tag. The localization accuracy requirement for a wide class of IoT applications is in the decimeter (10 cm) order and it must be functional in large (up to 100 m per dimension) indoor environments where NLOS scenarios are dominant with multipath-rich RF propagation. To date, there are few existing solutions that adequately address this set of challenging specifications which is critical to a wide set of localization based applications. Low-cost global positioning system (GPS) receivers [52], for example, cannot establish enough SNR to achieve better than several meters accuracy in indoor settings. WiFi or Bluetooth based indoor localization solutions are available today but their operating range is quite limited (<20 m) and their accuracy is in the order of a few meters that is insufficient to satisfy stringent public safety localization application requirements.

In this section we introduce *RF-Echo*, a new approach in RF localization that utilizes a frequency-shifting active reflector on the tag that echoes the orthogonal frequency division multiplexing (OFDM) [73] ranging signal generated from an anchor. A frequency conversion based full duplex approach enhances the localization range and accuracy beyond the level achievable by conventional narrowband RF localization

systems. We implemented the low power tag by fabricating a new custom ASIC in a 180nm CMOS technology. The anchor prototype is based on the USRP X310 [100] software defined radio (SDR) platform. Figure 4.1 shows the fabricated tag ASIC, the tag board, and the USRP based anchor. The tag ASIC area is $1.9\times2.7\text{mm}^2$ and its active power consumption at the maximum gain setting is 62.8mW. The proposed system has the following capabilities:

- **Decimeter accuracy with up to 85m localization range:** We propose a frequency domain signal processing technique that combines OFDM and neural network to accurately estimate the RF signal ToF in the frequency domain. Our measurement results show that decimeter accuracy is achievable over a $\leq$85 m operational distance indoor. Neural network training is based on extensive synthesized data, thus it does not require retraining after deploying the system in the field.

- **Low cost, small form factor, and low power for wearable tags:** The active reflector on the tag has a very simple architecture with minimal RF components comprising only a low noise amplifier (LNA), a bandpass filter, a frequency converter, and a power amplifier (PA). The tag does not require power-demanding high accuracy time / frequency references or sophisticated digital signal processing (DSP). The proposed technique eliminates the need for a phase-lock-loop (PLL) [80] or a crystal frequency reference for the tag IC, thus significantly lower the tag manufacturing cost.

- **Operable in NLOS and multipath-rich environments:** We investigate effective bandwidth enhancement techniques such as neural network based timing interpolation. This technique significantly enhances the effective bandwidth to analyze a multipath channel response profile in a finer resolution that is beyond

the limit given in the literature [92][18] for a narrowband system. Operating with a modest bandwidth (≤80 MHz), the proposed technique will provide sufficient resolution to distinguish line-of-sight (LOS) and NLOS paths, thus revealing the direct path distance to the target tag. This low bandwidth requirement is the key to allow RF-Echo to operate in ≤2.4GHz ISM bands. The bandwidth utilization is much lower than that of a conventional UWB system. The lower frequency signal penetrates walls better and experiences less multipath interference than conventional UWB systems.

- **Rapidly deployable, low complexity infrastructure anchors:** The bandwidth of the proposed localization signal can be easily supported by many low cost commercial off-the-shelf (COTS) RF transceivers (e.g., USRP [100]) for anchor prototyping. In addition, we eliminated the need for synchronization among anchors, while many other localization systems (e.g., [54]) require a common frequency and/or time reference among anchors. In the proposed scheme, infrastructure anchors are rapidly deployable by simply pulling them into outlets since ranging between an anchor and a tag can be performed independently without interaction among each other. Time synchronization between a tag and an anchor is also unnecessary for RF-Echo.

This work presents RF-Echo system architecture, algorithm, tag design, anchor implementation, and localization field trial results conducted in a university campus building. The feasibility of a narrowband accurate NLOS indoor localization system is demonstrated with a low-power custom ASIC implementing a low complexity analog-only architecture without a PLL or external reference. A neural network based ToF-enhancement technique is introduced to improve the reliability and accuracy of RF-Echo without an excessive bandwidth requirement. Despite the limited transmit power available at the low-power tag, RF-Echo exhibits up to 85 m and 49 m ranging distance in realistic multipath-rich LOS and NLOS indoor scenarios respectively.

4.2 Background

Before we describe RF-Echo in depth, we first briefly introduce a conventional time-of-flight (ToF) ranging method in this section. The 1-dimensional (1D) distance estimation process between the anchor and the tag is denoted by ranging. Higher dimensional localization is conducted by combining 1D ranging results from multiple anchors through multilateration process discussed in Section **??**.

The ToF or time-of-arrival (ToA) based ranging techniques rely on measurements of signal travel time between an anchor and a tag with a goal to distinguish the shortest direct path arrival time from any subsequent (NLOS) multipaths [54] [40]. When sufficiently wide signal bandwidth is given, the ToF/ToA can be determined with high accuracy and since direct path always precedes the NLOS multipath, the two can be distinguished. One approach is to use an impulse-radio UWB system where very short (order of a nano second or less) pulses are transmitted and the arrival time of each pulse is estimated at the receiver to obtain the ToF of the transmitted signal [40] [102] [114] [64]. The bandwidth of an UWB pulse is inversely proportional to the pulse width and narrower pulses are preferred to obtain finer time resolution in ToF / ToA estimation. Since the RF signal travels at the speed of light, the time of flight directly maps to the distance with the relationship that 1 ns in ToF is equivalent to 30 cm in distance. The distance of the direct path in NLOS multipath-rich environments can be resolved by analyzing the first arrival signal time, not the strongest. One of key challenges to achieve decimeter level accuracy in ToF / ToA based ranging is to realize sub-nano second time resolution. In a conventional approach where the signal is sampled and then processed in the digital domain, this would require an ADC with >1G samples per second. However, such high-speed ADCs are extremely power hungry. Furthermore, as [54] shows, their cost increases exponentially with the sampling rate beyond 10MHz. Operating ADC at or above Nyquist sampling rate (>1GHz for UWB signals) is, therefore, impractical for many low-power low-cost

wireless sensor node localization applications.

While the UWB is beneficial to obtain the pulse arrival time in finer resolution, the wider bandwidth is prone to interference from different frequency bands. Relatively strong interference signals that might be present anywhere in the ultra-wide bandwidth can saturate UWB receiver amplifiers. A highly linear RF circuit for UWB is very power demanding, whereas the limited linearity of the amplifier could constraint the UWB receiver operability in the presence of in-band interferers. Moreover, due to its ultra-wide bandwidth, operating at a higher carrier frequency (typically $>$ 4 GHz) is inevitable where signals experience worse pathloss and wall penetration loss, lowering its signal-to-noise ratio (SNR). According to the free-space Friis equation, 4 GHz carrier suffers 13 dB worse pathloss than a 900MHz carrier, which translates to more than 4$\times$ decrease in distance (6 dB SNR corresponds to 2$\times$ distance).

The frequency-modulated continuous-wave (FMCW) based ranging [92] [18] is a method widely used in radar systems to estimate ToF in the frequency domain. In conventional FMCW systems, the radar (i.e., anchor) transmits frequency-modulated chirp signals. The FMCW radar transmit signal, $s(t)$, is represented by Equation (4.1) where f_c is the carrier frequency, s_f is the frequency chirp slope, and T_{chirp} is the chirp duration. The chirp bandwidth is defined as $BW_{chirp} = s_f T_{chirp}$. The operating principle of the FMCW radar is illustrated in Figure 4.2.

$$s(t) = e^{j2\pi t(f_c + \frac{s_f t}{2})} \tag{4.1}$$

The FMCW radar estimates the distance to an object by analyzing the received signal $r(t)$ that is *passively reflected* by an object. The passively reflected signal $r(t)$ is a time-delayed (due to round-trip ToF) version of the transmitted signal. The $r(t)$ can be denoted by $h(t) * s(t) + n(t)$ where $*$ stands for convolution, $n(t)$ is the noise induced at the receiver and $h(t)$ is the round-trip channel impulse response in time

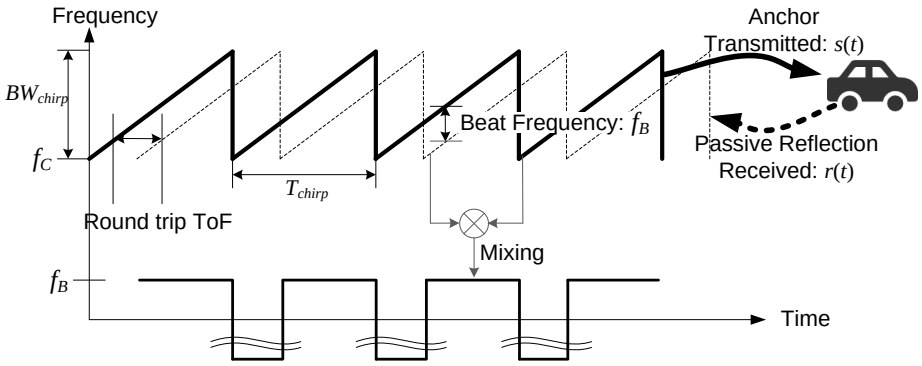


Figure 4.2: Operating principle of the FMCW radar. The time of flight (ToF) is proportional to the beat frequency f_B

domain. Note that the round-trip ToF and the ranging distance have the relationship (4.2), where τ_0 is the one way time-of-flight, c is the speed of light, and d is the distance to an object.

$$Roundtrip \;\; ToF = 2d/c = 2\tau_0 \tag{4.2}$$

For now, let us assume $h(t) = \delta(t - 2\tau_0)$ (i.e., non-multipath channel without delay spread). When the received reflection signal is mixed with the transmitted chirp signal, $r^*(t)s(t)$, a constant *beat* frequency, f_B, is observed in the down-converted (and low-pass filtered) baseband signal as in (4.3) (see Figure 4.2 for illustration). This constant beat frequency indicates the distance d to an object, as it is proportional to the round-trip ToF of the signal.

$$LPF\{r^*(t)s(t)\} = e^{j2\pi f_B t} + \tilde{n}(t), \;\; f_B = s_f d/c\tau_0 \tag{4.3}$$

4.3 Proposed System: RF-Echo

RF-Echo uses a full-duplex active RF reflector to estimate the range based on the round-trip ToF in frequency domain. The anchor transmits a 2.4 GHz carrier

frequency ranging signal to the tag, which concurrently (in a full duplex fashion) relays the ranging signal back to the anchor with carrier frequency down-conversion to 900 MHz. Unlike a conventional RF radar, which relies on passive reflections, this active reflection with the frequency shifting approach allows full-duplex tag design without incurring complexity overhead to cancel the self-interference in the same frequency. Realizing a full-duplex system with the same transmit and receive frequency is technically challenging [13]. We have dramatically reduced the active reflector tag design complexity by intentionally shifting the reflection carrier frequency at the tag for full-duplex operation.

Main advantages of RF-Echo using a new active reflector tag are summarized as follows: 1) Increased range due to signal amplification at the tag IC; 2) Distinction between the tag reflection at 900MHz and non-targets passive reflection at 2.4 GHz; 3) Flexibility of the ranging signal scheme, allowing for application-specific waveform design; 4) Simplicity in the RF and analog tag IC design without discrete time sampling or DSP circuitry, resulting in low power, smaller chip area, low cost, and deterministic delay; 5) Lower signal pathloss and better wall penetration for the returning path from the tag because of the lowered (2.4GHz to 900MHz) carrier frequency.

The carrier frequency selection for the RF-Echo system is based on the trade-off study considering the tag power consumption, signal pathloss, wall penetration characteristic, and FCC regulations for different carrier frequency options. The 2.4 GHz ISM band for anchor transmission allows relatively high TX power over a wide bandwidth (80MHz). The 900 MHz band reflection is selected because of the maximum signal level specified in the FCC regulation which is the highest among sub-GHz bands for the continuous 80MHz bandwidth.

Figure 4.3 shows the RF-Echo system block diagram. The anchor consists of an off-the-shelf USRP SDR [100] that transmits a $\leq$80 MHz bandwidth ranging signal at 2.4 GHz. The tag receives this signal, shifts the carrier frequency to 900 MHz, and

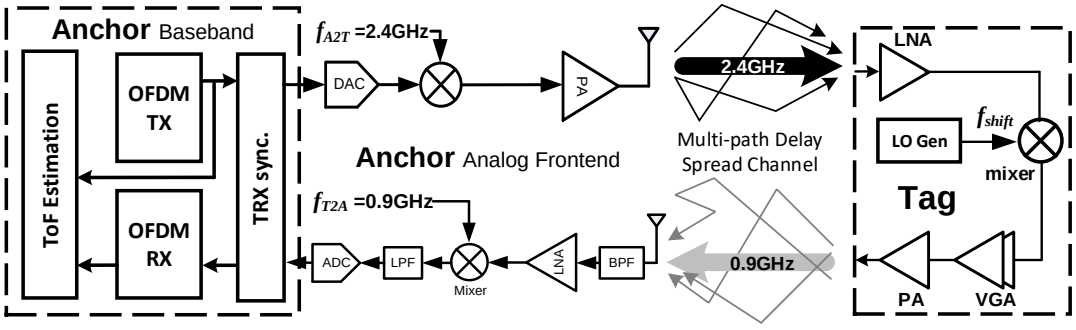


Figure 4.3: The overall RF-Echo system diagram. The anchor broadcasts ≤80MHz OFDM signals at the 2.4GHz carrier frequency and the active reflector IC echoes the OFDM signal in a full duplex fashion.

echoes it with a *deterministic delay*. Transmission and reception occur *concurrently at the anchor and tag*. The 2.4 GHz ISM band operation of the anchor allows up to 4W transmit equivalent isotropically radiated power (EIRP). On the other hand, the returning signal power from the tag is much lower, ≤1mW. This asymmetric power level is because of the FCC regulation (5000μV/m @ 3m at 900 MHz) and the low power constraint at the tag. RF-Echo allows a mechanism to adjust the transmit power from the anchor to limit the reflection power from the tag at 900 MHz to be under the FCC limit. Although the returning signal power is low, the sub-GHz frequency signal penetrates walls better and experiences less multipath interference than higher frequency signals.

Operating with a modest bandwidth of ≤ 80 MHz, the proposed system specification can be easily met by many low cost commercial off-the-shelf (COTS) RF transceivers and SDRs such as USRP [100] for anchor prototyping. In addition, we eliminated the need for synchronization among anchors in our scheme, while many other localization systems (e.g., [54]) require a common (i.e., cabled) frequency and/or time reference among anchors. In our scheme, infrastructure anchors are rapidly de-

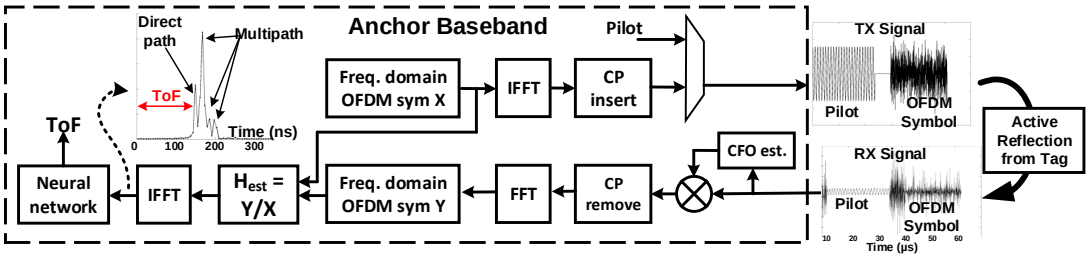


Figure 4.4: The OFDM based ToF estimation datapath

ployable since ranging between an anchor and a tag can be performed independently without interaction among each other. In fact, making anchors rapidly deployable is very crucial in some applications such as fire fighter location tracking. Time synchronization between a tag and an anchor is also unnecessary for RF-Echo.

4.3.1 OFDM based Ranging Waveform

The FMCW waveform discussed in Section 4.2 has a fundamental limit in estimating ToF when the channel has severe multipaths. Each multipath signal has a different arrival time at the anchor, thus unequal beat frequencies of random phase and magnitude multipath signals are mixed together resulting in the inter-carrier interference. Conventional FMCW systems use ultra-wide bandwidth to separate multiple beat frequencies in a high resolution [18]. To efficiently eliminate inter-carrier interference from multipaths without an excessive bandwidth requirement, we propose an OFDM based ranging signal using the datapath shown in Figure 4.4.

The transmitted OFDM symbol in frequency domain is defined by an $N \times 1$ complex valued vector $\mathbf{X} = [X[0], X[1], ..., X[N-1]]$ where $X[n]$ is a complex valued constellation point for the subcarrier n, and N is the number of subcarriers in the signal bandwidth (BW). The IFFT output of $\mathbf{x}$ is an $N \times 1$ complex valued vector $\mathbf{x} = [x[0], x[1], ..., x[N-1]]$, where $x[n]$ is the time domain complex sample at the time index n with Nyquist sampling rate of $1/\text{BW}$ (complex valued signal). To mitigate the

inter-symbol interference (ISI) from the multipath delay spread, a cyclic prefix (CP) guard interval is appended to each OFDM symbol. Note that the CP guard interval must be longer than the worst case delay spread from multipaths. The CP appended signal $\mathbf{x}$ is converted to the continuous time domain signal $x(t)$ and then up-converted to 2.4 GHz for anchor transmission. This 2.4 GHz passband anchor transmit signal is denoted by $x_{A2T}(t) = x(t)e^{j2\pi f_{A2T}t}$, where f_{A2T} =2.4 GHz, as shown in Figure 4.3.

Accurately estimating the distance from the anchor to the tag is the central objective of RF-Echo. When the distance is d, the channel impulse response $h_{A2T}(t)$ from the anchor to the tag can be modeled as (4.4), where L_{A2T} is the number of multipaths, $\tau_0 = d/c$ is the one-way ToF of the RF signal to travel the distance d in the shortest path, and $h_{A2T,0}$ is the corresponding channel gain (complex valued). Other terms $h_{A2T,i}\delta(t - \tau_{A2T,i})$ are from multipath reflections satisfying $\tau_{A2T,i} > \tau_0$ with $i \geq 1$. The shortest path channel gain could be much weaker than those of other multipaths, $|h_{A2T,0}| \ll |h_{A2T,i}|,\ i > 0$, especially in NLOS conditions. Estimating τ_0 is our goal.

$$\begin{aligned} h_{A2T}(t) &= h_{A2T,0}\delta(t - \tau_0) + \sum_{i=1}^{L_{A2T}} h_{A2T,i}\delta(t - \tau_{A2T,i}), \\ h_{T2A}(t) &= h_{T2A,0}\delta(t - \tau_0) + \sum_{i=1}^{L_{T2A}} h_{T2A,i}\delta(t - \tau_{T2A,i}) \end{aligned} \tag{4.4}$$

Using $h_{A2T}(t)$, the received signal at the tag is denoted by $r_{tag}(t) = h_{A2T}(t) * x_{A2T}(t) + n_{tag}(t)$ where $n_{tag}(t)$ is noise added at the tag receiver front-end and the operator $*$ stands for convolution. We propose *active reflection* at the tag, where the received signal is frequency converted to 900 MHz band and sent back to the anchor in a full frequency duplex fashion. The reflected signal can be written as $x_{T2A}(t) = r_{tag}(t)e^{-2\pi f_{shift}t}$ where $f_{shift} = f_{A2T} - f_{T2A}$, and f_{T2A} =900 MHz. Here we ignore the deterministic delay of the tag analog processing, which can be easily calibrated out at the anchor. The $x_{A2T}(t)$ reception and $x_{T2A}(t)$ transmission occur simultaneously

at the tag (and at the anchor too). Unlike conventional digital systems, the active reflection tag employs *all-analog* processing as depicted in Figure 4.3. This approach allows the anchor to estimate the ToF τ_0 without ambiguity associated with the tag processing delay. The reflected signal $x_{T2A}(t)$ from the tag experiences channel impulse response $h_{T2A}(t)$ (4.4), which is different from $h_{A2T}(t)$ because of the carrier frequency difference. However, the shortest path ToF, τ_0, is common for both $h_{A2T}(t)$ and $h_{T2A}(t)$ as indicated in (4.4). The anchor receiver performs frequency mixing by $e^{-j2\pi f_{T2A}t}$ to bring the signal back to baseband. The baseband received signal at the anchor, therefore, can be represented by $y(t) = h_{A2T}(t) * h_{T2A}(t) * x(t) + n_{anchor}(t)$ where $n_{anchor}(t)$ is the equivalent noise at the anchor. In the frequency domain, (4.5) holds where $Y(f)$, $H_{A2T}(f)$, $H_{T2A}(f)$, $X(f)$ and $n_{anchor}(f)$ are Fourier transform representations of $y(t)$, $h_{A2T}(t)$, $h_{T2A}(t)$, $x(t)$, and $n_{anchor}(t)$ respectively. Before further processing, the guard interval is removed from $y(t)$ to mitigate the ISI as in conventional OFDM systems [73].

$$Y(f) = H_{A2T}(f)H_{T2A}(f)X(f) + n_{anchor}(f) \tag{4.5}$$

Note that the baseband signal $x(t)$ and $y(t)$ are sampled *simultaneously using the same local clock* of the anchor. By taking FFT on Nyquist sampled $y(t)$, the frequency domain received OFDM vector symbol $\mathbf{Y} = [Y[0], Y[1], , Y[N-1]]$ is obtained. Based on (4.5), channel estimation $\mathbf{H_{est}}$ in the frequency domain can be computed by (4.6). Unlike conventional FMCW, our method using OFDM does not suffer from inter-subcarrier interference in $\mathbf{H_{est}}$ computation. That is, $\frac{Y[j]}{X[j]}$ can be computed without interference from $i \neq j$ subcarriers because of inherent orthogonality among subcarriers in OFDM signaling [73]. The discrete time domain channel impulse response estimate $\mathbf{h_{est}} = [h[0], h[1], ..., h[N-1]]$ is obtained by taking IFFT on $\mathbf{H_{est}}$. Note that $\mathbf{h_{est}}$ is sampled at the rate of 1/BW. Our proposed system obtains

the ToF τ_0 by analyzing the interpolated signal $h_{est}(t)$ of the discrete time channel impulse response such that $h_{est}(t) = h_{A2T}(t) * h_{T2A}(t) \approx interpolation(\mathbf{h_{est}})$. $h_{est}(t)$ reveals the round-trip ToF $2\tau_0$ as illustrated in Figure 4.4 top-left.

$$\mathbf{H_{est}} = \left[\frac{Y[0]}{X[0]}, \frac{Y[1]}{X[1]}, ..., \frac{Y[N-1]}{X[N-1]}\right] \tag{4.6}$$

4.3.2 Synchronization with Crystal-Less Tags

The proposed active reflector based approach eliminates the need for time synchronization between the anchor and tag. The active reflector in the tag echoes the received signal to the anchor with a deterministic delay. All-analog design of the tag (Section 4.4) does not incur any sampling time ambiguity or sampling frequency offset that are inevitable in all discrete time based signal processing. Eliminating the notion of discretized time during the active reflection at the tag allows a tag design without a reference crystal to lower its manufacturing cost. Moreover, we propose a carrier frequency offset (CFO) self-calibration scheme to eliminate the conventional phase-lock loop (PLL) [80] for carrier frequency generation at the tag to further reduce its power consumption. Thus we demonstrate the feasibility of a *PLL-less and crystal-free* tag design for extremely cost-sensitive low-power tags.

The proposed CFO self-calibration is performed by sending a pilot tone, $p_{A2T}(t) = e^{j2\pi f_{pilot}t}$, before the OFDM signal $x(t)$ transmission (Figure 4.4, right). Any frequency mismatch f_{CFO} in the free-running LC oscillator of the tag will alter the frequency of the received pilot signal (ignoring noise) to $p_{T2A}(t) = e^{j2\pi(f_{pilot}-f_{CFO})t+j\phi}$, where ϕ is the random phase mismatch. The frequency offset is estimated at the anchor by the frequency of the mixed signal; $p_{A2T}(t)p^*_{T2A}(t) = e^{j\phi}e^{j2\pi f_{CFO}t}$. The random phase offset ϕ can be ignored for ToF ranging. To validate this concept, the proposed tag IC (Section 4.4) is fabricated employing a free-running LC-oscillator circuit without a PLL or a reference crystal clock for frequency (f_{shift}) generation.

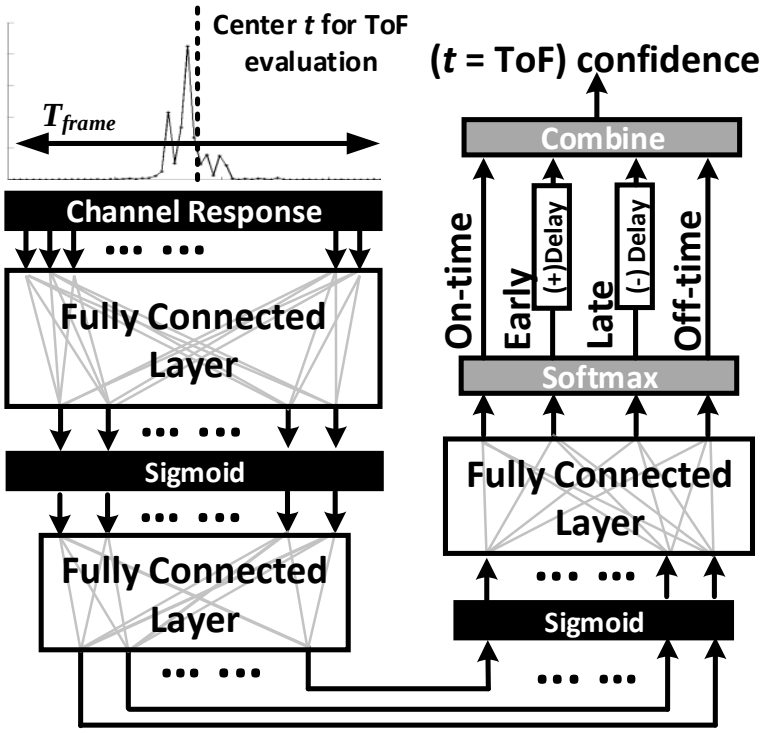


Figure 4.5: The proposed feedforward neural network structure

4.3.3 Neural Network based ToF Estimation

In contrast to the conventional UWB time domain ToF estimation where >1 GHz bandwidth is required to achieve cm-scale accuracy, we utilize a modest ≤80 MHz bandwidth OFDM signal and analyze the reflected signal in the frequency domain to reconstruct the time-domain channel impulse response. This ≤80 MHz constraint is from the 2.4 GHz ISM band restriction. Nyquist sampling rate (=1/BW for a complex signal) of 80 MHz bandwidth signal indicates that the time resolution is only 12.5 ns. This is equivalent to 3.75 meter resolution for the RF signal that travels at the speed of light c, which would severely limit the accuracy of the ToF based ranging.

The accuracy limitation of this relatively low signal bandwidth of RF-Echo is overcome by a neural network based ToF estimator employed at the anchor. The proposed

neural network has a fully connected feed-forward structure [41] with two hidden layers as shown in Figure 4.5. The neural network is trained with many (>500 k) multipath channel impulse response (CIR) training examples $h_{est}^{train}(t) = h_{A2T}^{train}(t) * h_{T2A}^{train}(t)$ that are synthesized (simulated) in Matlab. In other words, the neural network training *does not necessarily require real-world channel impulse response dataset* which is typically unavailable when RF-Echo is deployed in unknown environments. Extensive training dataset are generated using an ITU indoor channel model [47] with exponential delay profiles, randomly generated multipath taps, and random delay spreads to cover various NLOS channel scenarios. Based on the simulated dataset, feed-forward network weights are trained using a back-propagation method [41]. The neural network output is the confidence value that is (statistically) maximized when the input channel impulse response is well-aligned with the *representative shape* of the training dataset waveforms that are all centered at the ground-truth round-trip ToF. The training dataset $h_{est}^{train}(t)$ and the CIR estimation $h_{est}(t)$ signals are the interpolated (by a factor of $\geq 10\times$) version of the discrete time channel impulse response sampled at Nyquist rate. For neural network training and evaluation, we use the dB representation of the signal amplitude $20log_{10}(|h_{est}^{train}(t)|)$ and $20log_{10}(|h_{est}(t)|)$, respectively.

The training signal $h_{est}^{train}(t)$ is trimmed for the time span $t \in [2\tau_0 - \frac{T_{frame}}{2}, 2\tau_0 + \frac{T_{frame}}{2}]$, which is centered around the ground-truth round-trip ToF $2\tau_0$. T_{frame} is the training signal window size as shown in Figure 4.5 and 4.6. Note that the training signal window size is much shorter than the entire CIR time span because the neural network is only trained for the *CIR shape around the shortest ToF point*. For ToF estimation, the estimated channel impulse response $h_{est}(t)$ is fed into the trained neural network in a sliding window fashion as shown in Figure 4.6. When the sliding window position is τ, the $h_{est}(t)$ input window span is $t \in [2\tau - \frac{T_{frame}}{2}, 2\tau + \frac{T_{frame}}{2}]$ and the neural network evaluates if this windowed signal resembles the training dataset.

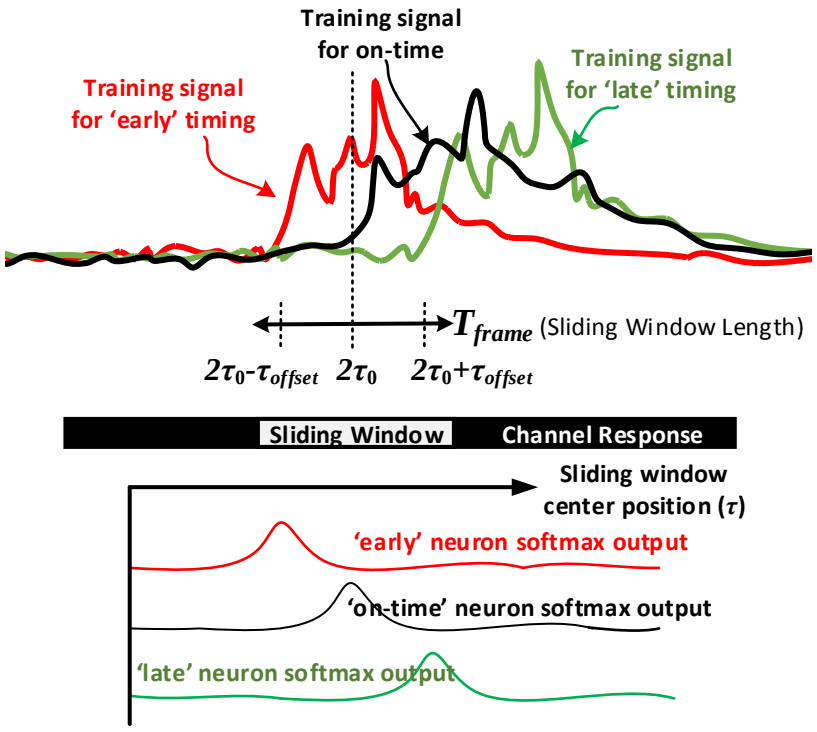


Figure 4.6: The proposed bootstrap aggregating method

The neural network output is (statistically) maximized when τ is the same as the ground-truth ToF $2\tau_0$, as illustrated in Figure 4.6.

To further improve the accuracy of the neural network based ToF estimation, we apply the *bootstrap aggregating* method [41] [17]. The idea is to train the neural network with several different models separately, then have all the models vote on the output to accurately estimate ToF from the $h_{est}(t)$ signal. In our proposed solution, we train the neural network not only with the training signal that is centered around the ground-truth $2\tau_0$ (i.e., *on-time* dataset) but also with other (independently generated) training dataset with a time offset τ_{offset} in ToF. The training dataset with the *early* and *late* offset has the signal span of $[2\tau_0 - \tau_{offset} - \frac{T_{frame}}{2}, 2\tau_0 - \tau_{offset} + \frac{T_{frame}}{2}]$ and $[2\tau_0 + \tau_{offset} - \frac{T_{frame}}{2}, 2\tau_0 + \tau_{offset} + \frac{T_{frame}}{2}]$ respectively as depicted in Figure 4.6. As the sliding window position τ of the neural network input $h_{est}(t)$ changes from

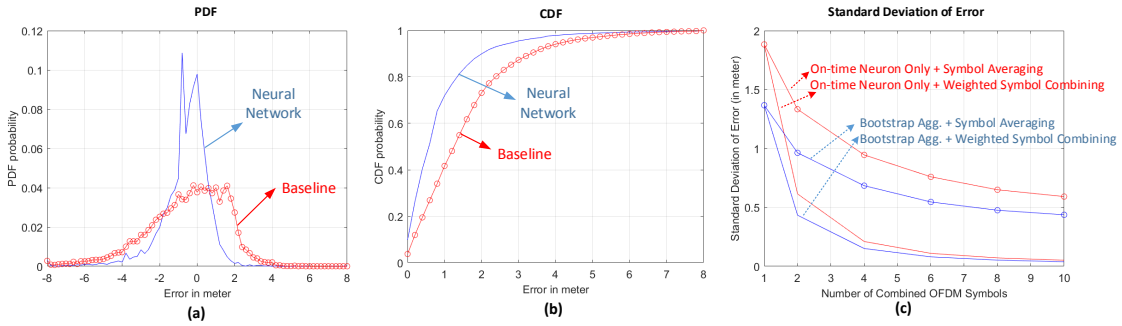


Figure 4.7: Ranging accuracy simulated in Matlab with 50ns delay spread multipath channels: (a) Probability density function (PDF) of errors; (b) Cumulative density function (CDF) of errors; (c) Standard deviation of errors from multiple symbol combining and bootstrap aggregation

0 to the maximum ToF, the neuron trained with *early* offset would generate a high confidence output first. As the slide window position τ passes by $2\tau_0$ and $2\tau_0 + \tau_{offset}$, we expect to observe a high confidence output sequentially from the *on-time* trained neuron and then from the *late* offset neuron. By combining these three confidence outputs with proper time delays, the accuracy of ToF estimate significantly improves compared to the case with *on-time* training dataset only.

Figure 4.7 shows the accuracy improvement from the proposed neural network algorithm compared to a hand-designed baseline algorithm. In the baseline algorithm, ToF is estimated by the timing when the power of the sample exceeds a dynamically set threshold level that is proportional to the first peak level in the channel impulse response. The threshold of the baseline algorithm is optimized over an extensive dataset for fair comparison. The Matlab simulation results in Figure 4.7 (a) and (b) confirm that, in a challenging 50m NLOS scenario, the neural network algorithm (error standard deviation $e_{std} = 1.45$m) outperforms the baseline ($e_{std} = 2.09$m). This result is from the single 20μs long OFDM symbol based ranging. The ranging accuracy of the neural network algorithm is further improved by the confidence-weighted symbol combining technique discussed in the next section.

4.3.4 Symbol Combining

The operating range target of RF-Echo is up to 100 m, which exceeds the typical operating range of popular ISM band communication standards such as WiFi. The operating range is constrained by the FCC regulation that limits the RF power transmission to be under 4W EIRP for 2.4 GHz ISM band and $\leq$5000μV/m @ 3 m for the 900 MHz returning path. Our tag ASIC maximum transmit power is limited to 0 dBm (1 mW). Although the 80 MHz bandwidth is significantly lower than that of UWB radios, it is still 4$\times$ wider than the legacy WiFi specification. Enhancing SNR for 80 MHz operation is critical to achieve $\approx$100 m range in indoor scenarios.

For RF-Echo, the complicated band-stitching technique [86] [82] can be replaced by a simple coherent signal combining of multiple OFDM symbols to enhance SNR. Although the tag and anchor are unsynchronized, a coherent channel estimation process is realized at the anchor by the *self-phase aligned processing*. That is, both transmit and receive signals are sampled using the *same local anchor clock* while the reflection delay of the tag is deterministic and constant. The frequency domain channel estimation from the i-th OFDM symbol can be represented by $\mathbf{H_{est,i}} = \mathbf{H_{est}} + \mathbf{n_i}$ where $\mathbf{H_{est}}$ is the true channel response and $\mathbf{n_i}$ is the noise vector in frequency domain. As long as the channel is stationary for multiple consecutive OFDM symbols, combining K channel estimations from consecutive OFDM symbols would increase the effective SNR by a factor of K because channel estimation from multiple measurement would add constructively (due to the self-phase aligned coherent channel estimation) while the independent noises are combined incoherently; $\sum_{i=1}^{K} \mathbf{H_{est,i}} = K\mathbf{H_{est}} + \sum_{i=1}^{K} \mathbf{n_i}$. That is, $\| K\mathbf{H_{est}} \|_2^2 = K^2 \| \mathbf{H_{est}} \|_2^2$ while $\mathrm{E}\left\{ \| \sum_{i=1}^{K} \mathbf{n_i} \|_2^2 \right\} = K\mathrm{E}\{\| \mathbf{n_i} \|_2^2\}$. The OFDM symbol duration is in the order of 10s of μs. Therefore, combining $\leq$10 OFDM symbols per localization fix does not incur unacceptable delay, while it provides up to 10dB SNR improvement.

It is also possible to combine multiple ToF estimates from the neural network out-

put. A naive way of combining multiple ToF estimates is to use arithmetic averaging of estimated distances. The proposed neural network approach allows combining multiple ToF estimates by weighted combination using the confidence output of the final neuron. Since the activation function of the final layer of the neural network is the soft-max function, we can interpret the neural network output as the confidence weight associated with each ToF estimate. The simulation results in Figure 4.7 (c) show the comparison between arithmetic averaging and the weighted combining. It also shows the performance gain of the proposed bootstrap aggregation (using early, on-time and late neurons) compared to the conventional case where only on-time neuron is used. The standard deviation of 1D ranging error (e_{std}) is reduced (Matlab simulation results) from 1.45m to <0.085m by applying the confidence weighted combining of ≥6 OFDM symbols (20μs each) in a 50ns delay spread NLOS channel. The actual measurement data using the fabricated IC is presented in Section 4.5.

4.3.5 Multilateration for 2D / 3D localization

The 2D or 3D coordinate of the tag is obtained by the multilateration process [16, 20, 99, 21], which combines 1D ranging results from at least three anchors. It is the same process used by GPS geolocation. Given the distance estimate $\hat{d}_j$ from the j-th anchor to the tag, the tag location coordinate estimate $\mathbf{p}^*$ can be obtained by solving the optimization problem (4.7) [16] where $\mathbf{p_j^{anchor}}$ is the known coordinate of the j-th anchor, and J is the number of anchors. The optimization problem can be generalized to 2D or 3D coordinate localization cases with at least three anchors.

$$\mathbf{p}^* = \underset{\mathbf{p}}{\operatorname{argmin}} \sum_{j=1}^{J} \left(\| \mathbf{p_j^{anchor}} - \mathbf{p} \|_2 - \hat{d}_j \right)^2 \tag{4.7}$$

The optimization problem (4.7) is non-convex. However, it can be efficiently solved by algorithms summarized in [20, 99, 21]. Closed form solutions are also available

[16]. The accuracy of the multilateration is directly affected by the reliability of 1D ranging performed at each individual anchor.

4.4 Implementation

The proposed active reflector tag ASIC is fabricated in a CMOS 180nm process technology. Figure 4.8 (a) and (b) show the schematic of the proposed tag IC. It consists of a transformer-based differential low-noise amplifier (LNA), frequency down-conversion circuits, variable gain control units (VGA), and a class-AB power amplifier (PA). Figure 4.8 (c) shows the fabricated chip micrograph with each component indicated. The tag IC supports a gain dynamic range of 60 dB to adjust to the received signal strength at different distances. The frequency down conversion improves the pathloss of the return path (i.e., 900 MHz reflection rather than 2.4 GHz), which lessens the transmit burden at the low power reflector, while also solving the TX/RX self-interference issue for full duplex operation. The proposed asymmetric reflective architecture simplifies tag design by shifting all signal processing complexity to the anchor and eliminating the need for time synchronization between the anchor and the tag. The transmit power is also asymmetric between the anchor and tag. Given a gain setting at the tag, the anchor can adjust its transmit power so that the returning signal power from the tag at 900 MHz is under the FCC mask.

The tag IC is designed to support a >10 dB peak-to-average-power ratio for an 80 MHz bandwidth OFDM signal with 15 – 60 dB of variable total gain. The transformer-based input matched LNA performs inherent single-ended to differential conversion, providing the doubled-balanced mixer input. This architecture is suitable for compact input matching for the 80 MHz bandwidth target [28]. To minimize the power consumption and dimension on the tag, we eliminate the usage of a crystal oscillator and the phase-locked loop (PLL) for generating the shifting frequency (f_{shift}). Instead, it uses an LC-based free-running voltage controlled oscillator (VCO) as the

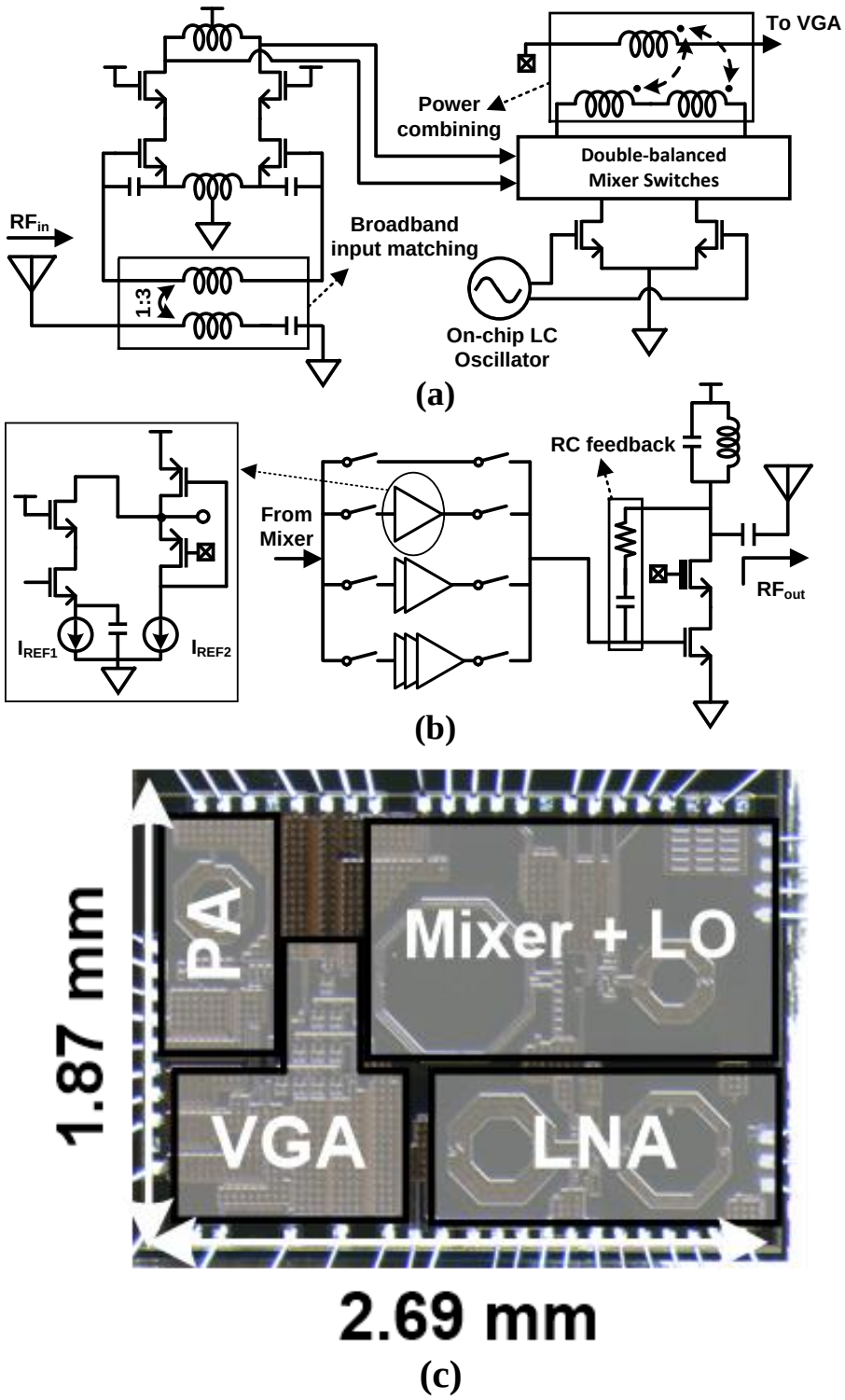


Figure 4.8: The active reflector ASIC (a) LNA and mixer circuit schematic; (b) VGA and PA circuit schematic; (c) Chip die photo (fabricated in 180nm CMOS technology)

local oscillator (LO) and a current-commuting mixer [80] with transformer load as shown in Figure 4.8. PLL-less LO generation enables low power design of the tag but it is inevitable to have an inherent carrier frequency offset (CFO) that is slowly drifting over time from the target frequency. We tackle this issue using the CFO estimation/compensation technique described in Section 4.3. The pilot tone does not have to be inserted for every OFDM symbol as the CFO drifts slowly (at least in the order of millisecond) over time.

The transformer at the mixer output acts as a filter and a power combiner. The mixer is designed to directly drive the PA in the bypass mode with sufficient linearity. The variable gain amplifier (VGA) provides a high dynamic range and consists of 4 gain paths: high gain, mid gain, low gain, and bypass. Because of the required peak gain (60 dB) at 900 MHz and the limited on-chip area, an active inductor is used to boost the gain. The last stage is a single-ended class-AB PA with RC feedback to increase the linearity and stability.

By eliminating the off-chip crystal oscillator and PLL, the cost, complexity, and power consumption of the tag IC is significantly reduced. The measured power consumption of the tag IC is 62.8 mW when it operates with the maximum (60 dB) gain for active full-duplex reflection. With a 30 μs long ranging symbol (10 μs pilot plus a 20 μs OFDM symbol), the tag energy consumption per 1D ranging translates to 1.8 μJ.

4.4.1 Anchor Design

For the anchor prototype (Figure 4.1), we use an USRP X310 [100] with an SBX-120 RF card [88] to enable the full duplex transmit and receive operation at the same time. The precise timing of the baseband OFDM transmit and receive signal sampling is controlled by a common 200 MHz main clock on the USRP FPGA. The global time stamp on the FPGA allows initiating both transmit and receive paths at

the same time for the self-aligned time synchronization. The maximum OFDM signal bandwidth supported by the anchor prototype is 100 MHz. The baseband OFDM waveform generation, OFDM signal reception, pilot insertion, carrier frequency offset tracking, and neural network based post-processing are all performed on a laptop running Ettus UHD RFNoC and Matlab software.

The 2D or 3D localization requires multiple anchors operating in a time multiplexed fashion. The accurate time synchronization among anchors, however, is not required as long as the ranging OFDM signal does not collide during the shared medium access. Each anchor can operate with a simple carrier sensing collision avoidance scheme for the medium access control. Accurate carrier frequency synchronization among anchors is also unnecessary. Any carrier frequency offset between an anchor and a tag will be resolved locally at each anchor. Without needs for accurate synchronization, anchors are rapidly deployable by simply pulling them into outlets. The 1D ranging between an anchor and a tag can be performed independently without interaction among each other. The 2D/3D localization coordinate of the target tag is established by sharing 1D ranging results among anchors and performing the multi-lateration process.

4.5 Evaluation

The measured tag sensitivity is -73 dBm when SNR is 10 dB at the anchor, which is sufficient for reconstructing the channel impulse response at 85 m LOS. The 1-dB compression point of the tag is -60 / -42 / -31 / -22 dBm for high / mid / low / bypass gain mode, respectively (Figure 4.9).

Figure 4.10 shows examples of the reconstructed impulse response $H_{est}(t)$ wirelessly captured in the field-trial with 80MHz bandwidth. Note that $H_{est}(t)$ is plotted as a function of distance (not time) by using the relationship $d/c = t$. Figure 4.10 (a) and (b) are channel instances in a university building for LOS and NLOS scenarios

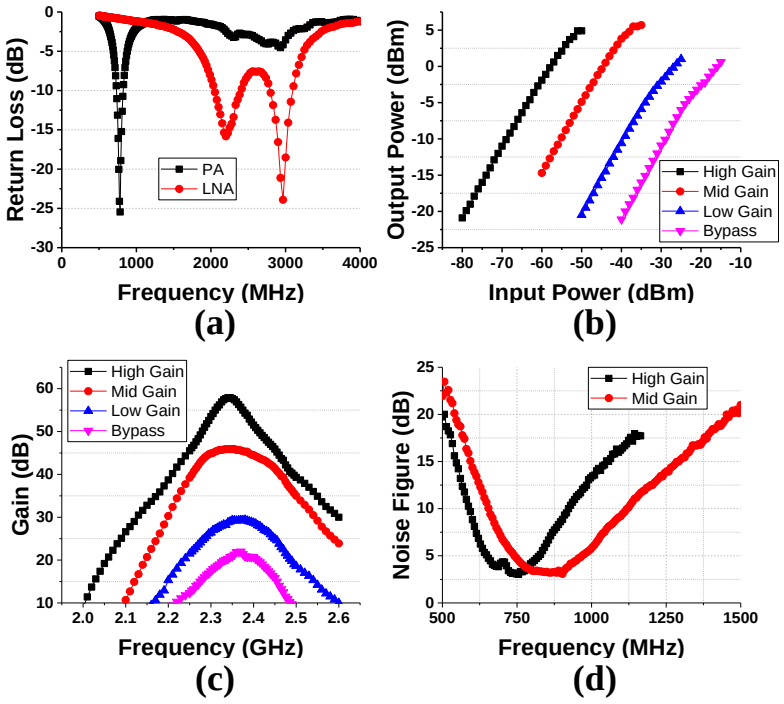
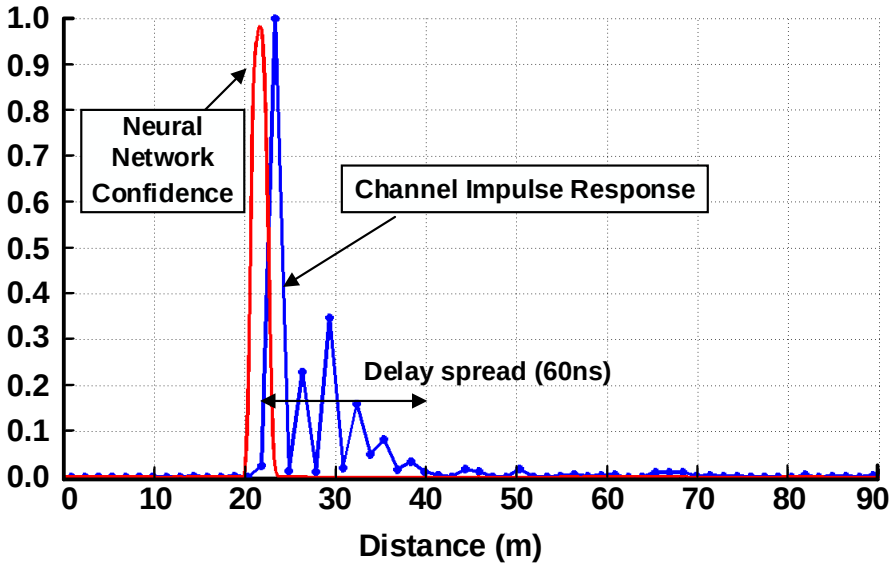


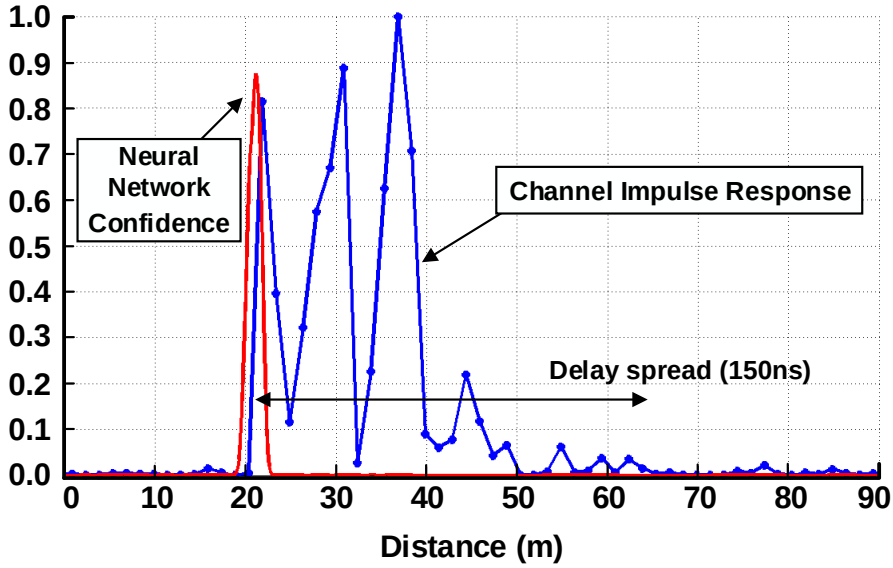
Figure 4.9: ASIC tag performance: (a) Impedance matching; (b) Different gain mode setting; (c) Frequency response; (d) Noise figure

at 21.75 and 21.3 m distances respectively. Notice the severe multipath delay spread in these channel impulse responses. It also shows the neural network confidence output that accurately estimates the ToF distance 21.7 m and 21.1 m at the maximum confidence of 0.97 and 0.87 (in the scale of 0.0 – 1.0) in LOS and NLOS scenarios.

Figure 4.11 summarizes the RF-Echo field-trial results for ≤85.6 m LOS and ≤39.3 m NLOS indoor 1D ranging conducted in a university campus building with testing setups shown in the same figure (top). The anchor has 30 dBm TX power and -90 dBm RX sensitivity. The operable ranging distance is limited by the tag IC reflection power ≤ 1mW (0dBm). The 1D ranging error histogram and the error standard deviation (e_{std}) of the same field-trials are presented in Figure 4.12 and 4.13, where the impact of neural network confidence-weighted symbol combining is shown. Each OFDM symbol is 20μs long with 1024 subcarriers.



(a) LOS



(b) NLOS

Figure 4.10: The anchor reconstructed channel impulse response and the neural network output confidence. For x-axis, time is converted to distance using $d/c = t$; (a) a LOS channel response; (b) a NLOS channel response

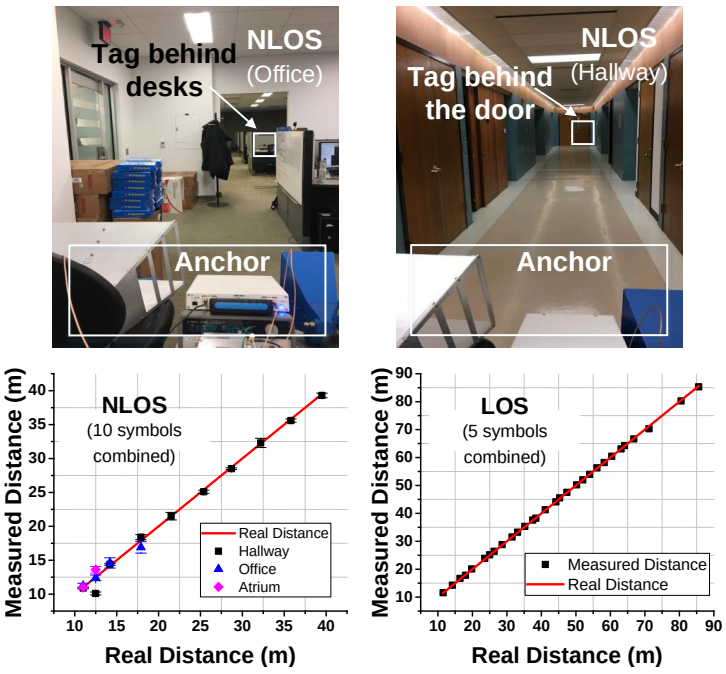


Figure 4.11: NLOS testing setups and the 1D LOS/NLOS ranging test results in various environments including Atrium, Office, and Hallway. The OFDM symbol length is 20 μs

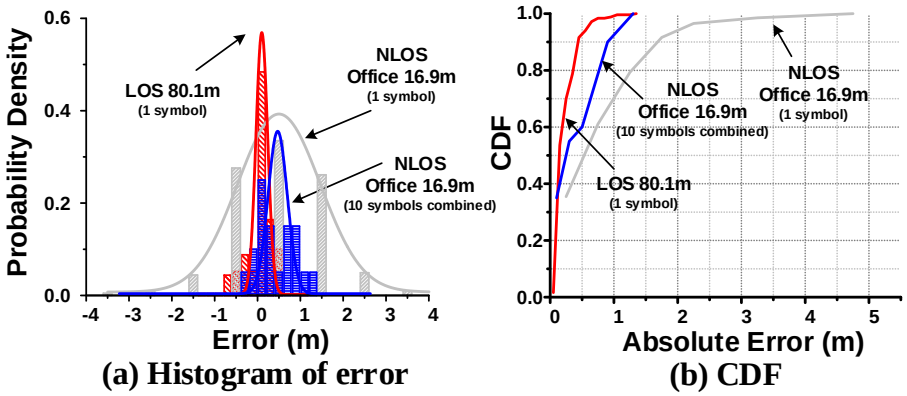


Figure 4.12: The 1D ranging error PDF and CDF for data points in Figure 4.11: (a) The error PDF with one or ten confidence-weighted OFDM symbols combining. Each symbol is 20μs long; (b) The CDF for same scenarios

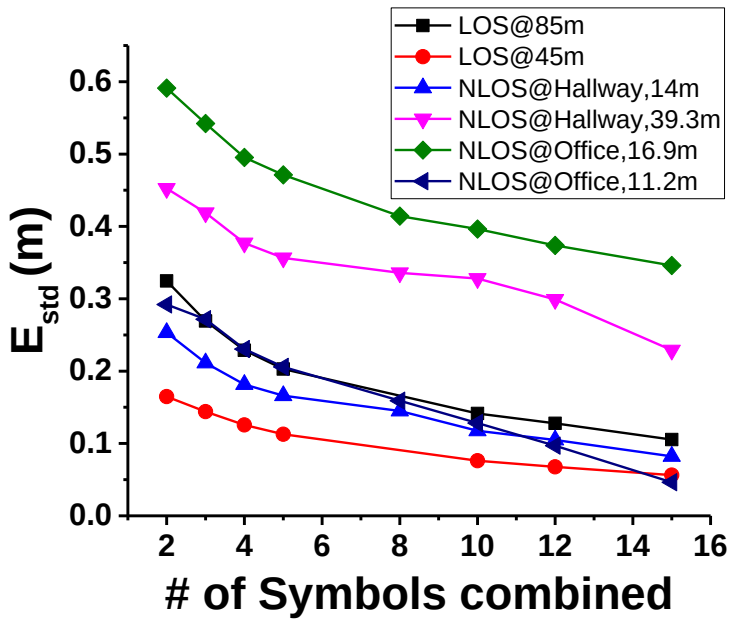


Figure 4.13: Error standard deviation as a function of the number of OFDM symbols combined

Figure 4.14 shows the 2D localization map obtained from a $30\times20\text{m}^2$ university campus building space. The error CDF results are also shown. Anchors are black stars labeled with A_1 – A_6. The red triangles are the ground-truth tag locations, and the blue dots are estimated tag locations. Each tag location uses 10 OFDM symbols combined per estimate, and each test point has 10 estimations. Note that only A_1 – A_4 anchors are used to locate the LOS trajectory marked in the blue line. Whereas only A_4 – A_6 anchors are used to perform the NLOS localization inside a large classroom. Walls in this building are made of thick concrete and bricks. The cluster of blue dots shows the error deviation of each estimation. The error of LOS trajectory is small and almost invisible except the location around T_{14} on the map. 90^{th} percentile LOS absolute error is $\leq$ 40cm. As the tag location extends in x-dimension, the angle difference from A_1 – A_4 anchors to the tag diminishes, making the accuracy at T_{14} worse in y-dimension. This artifact is known as the dilution of precision (DOP) in a GPS system [52]. NLOS localization capability (through thick

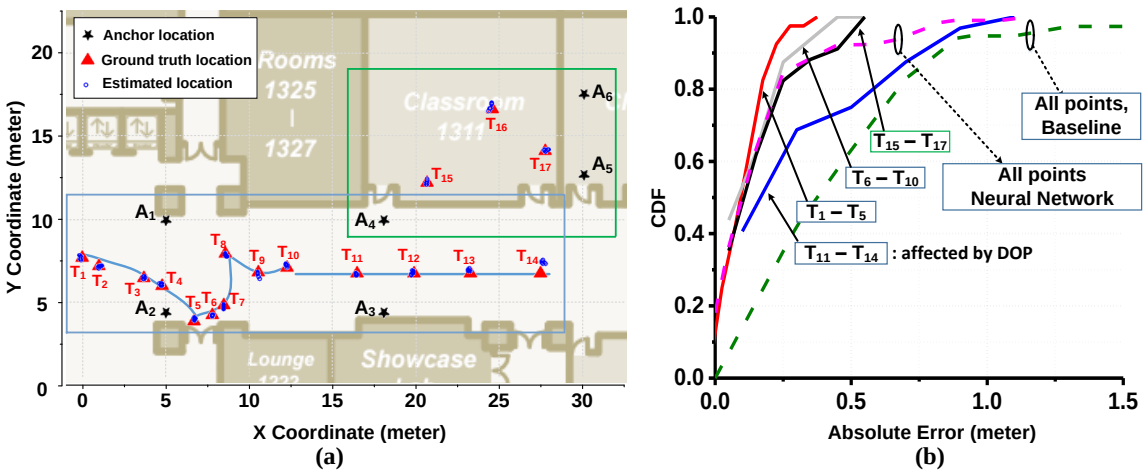


Figure 4.14: The 2D localization map in a 30×20 m^2 university building (a) Only A_1 – A_4 anchors are used to localize T_1 – T_{15} along the blue trajectory. Only A_4 – A_6 are used to localize the NLOS positions (T_{15} – T_{17}); (b) The CDF of the 2D localization error

concrete walls) is demonstrated via A_4 – A_6 anchors only to locate tags (T_{15} – T_{17}) in a large classroom. Note that A_4 is outside the classroom while A_5 and A_6 are in another classroom separated by a thick concrete wall. The error of this NLOS localization is small and unrecognizable on the map.

4.6 Related Work

One of the conventional approaches to perform RF signal based ranging is to use received signal strength indicator (RSSI) [113, 76, 87, 10]. The pathloss expression of RF signal propagation directly maps the RSSI to a distance using an inverse-square law. Due to simplicity of measuring RSSI, it has been widely adopted in WiFi or Bluetooth for ranging. Unfortunately, in NLOS or multipath-rich environments, signal fading results in large deviation in RSSI from the theoretical pathloss equation. The RSSI statistically follows a Rayleigh or log-normal distribution [79] in many practical multipath scenarios, which indicates large errors (at least a few meters) in ranging.

The angle-of-arrival (AoA) or direction-of-arrival (DoA) approach has been studied in the literature as an alternative localization method [75, 37, 27, 109]. The AoA approach performs coherent signal processing extracting the phase information of the received RF carrier signal at different antenna locations. The phase difference at different locations reveals the angle-of-arrival. Multiple AoA estimations obtained from three or more anchors provide the tag location through multilateration. Its performance, in theory, is insensitive to signal strength variation and potentially more robust than the RSSI-based method. However, employing multiple antenna arrays for AoA estimation increases the system cost, size, and complexity. Moreover, when severe multipaths exist and their signal strength is higher than or comparable to the LOS signal strength, AoA estimation could easily fail. This vulnerability to multipaths makes AoA-based methods inappropriate for many indoor localization applications. Recently, a novel synthetic aperture radar (SAR) localization system [57] is proposed to demonstrate feasibility of indoor localization in multipath environments using a commodity mobile device (a tablet PC). However, the mobile device in [57] requires accelerometer data with several seconds of motion. Its relatively low energy efficiency, high manufacturing cost per tag, and slow localization update rate limit its application for ultra-low cost, massively deployed low power tags.

With ToA / ToF based ranging capabilities, UWB radio technologies have been gaining interests since their usage in the 3.1 to 10.6 GHz band was approved by the FCC in 2002. DecaWave DW1000 [35] [34] is a commercial off-the-shelf 802.15.4a (UWB) compliant radio chipset that supports pairwise ranging between transceivers. The chipset's architecture and algorithm are not released in public. Unlike our solution, a stringent $\approx$10 ppm carrier frequency offset is required for system operation. The transceiver draws 393mW [35] of active power during transmit and advertises a ranging accuracy of 10 cm. Localization is performed in a packet basis with a maximum 6.8Mb/s data rate. At this data rate and a 512-byte (half of the maximum)

packet length, its energy per 1D ranging is 237μJ. The tag energy in RF-Echo is only 18μJ per 1D ranging with a conservative 10 OFDM symbols combining (including the pilot, 20μs per OFDM symbol).

Other ASIC solutions [43] [81] [96] published recently are all focusing on high-power and high-accuracy LOS applications such as radar or UWB ranging. [43] uses a time-extension method to avoid the high-speed ADC needed in the UWB ranging. Although [43] achieves decent accuracy without using a GHz-ADC, this solution requires strict timing synchronization between TX and RX, severely limiting the maximum operation range. [81] utilizes careful frequency planning and sub-sampling of the incoming signal to eliminate the need for high-speed ADC. However, this paper shares a common local oscillator (LO) between the TX and RX, bypassing the issue of synchronization. [96] realizes the phase domain successive-approximation radar (SAR) with a mm-wave frequency single-carrier. This approach requires a stringent TX-RX phase-locking (homodyne detection) and results in excessive power consumption of 457 mW with 4.38 mm^2 chip area.

WASP [86] is a relatively narrow band (125MHz) ToA-based system that reports up to 30 m indoor operation with 50 cm accuracy (with a tracking algorithm from a sequential measurement). Its COTS components based design utilizes high performance RF datapath whose power consumption is at least 2 Watts. Harmonium [54] introduces a compact (1.5cm^3) low-power (75mW) tag for UWB TDoA ranging with a unique frequency-stepped receiver architecture. However, its tight timing synchronization requirement between anchors (wire-connected to each other) limits its usability for large dimension operations. All evaluation in [54] was conducted in a rather small 4.6×7.2×2.7 m^3 room space.

Chronos [101] uses channel impulse response estimation available from commodity WiFi devices for indoor localization. It stitches multiple 802.11 WiFi bands to expand the effective signal bandwidth in order to achieve higher resolution and to

resolve the multipath profile using non-uniform Discrete Fourier Transform (NDFT). The proposed solution, however, assumes certain signal sparsity which might not be guaranteed in multipath-rich NLOS indoor environments. Unlike RF-Echo, Chronos requires a WiFi compliant chipset on a tag device, which would increase the tag manufacturing cost and power consumption compared to the RF-Echo tag. Its operation is based on 35 WiFi channel band stitching with 5MHz minimum spacing, which results in a relatively slow update rate of 84 ms per measurement and the theoretical limit of $\leq$60 meter ranging.

Table 4.1 summarizes comparison between our RF-Echo system and other ASIC / COTS based systems. RF-Echo's localization accuracy, tag power, energy efficiency, tag complexity (i.e., tag cost), localization update rate, and NLOS operable range all compare favorably to other prior arts summarized in Table 4.1.

4.7 Conclusion

In this section, we proposed RF-Echo, a new RF localization solution with unprecedented accuracy and energy efficiency for indoor applications. A newly fabricated active reflector ASIC is introduced to demonstrate the feasibility of low-power wireless tags that are small, low cost, and rapidly deployable without heavy infrastructure investment. The proposed approach uses OFDM signaling that effectively mitigates inter-carrier and inter-symbol interference which are common in wide bandwidth RF localization systems. Unlike conventional ToF based systems, our solution does not require strict timing and/or frequency synchronization among anchors and tags. Instead, each individual anchor uses a self-aligned timing and on-the-fly CFO tracking. This enables ultra-low cost design for the tag without a conventional PLL and clock reference crystal. The modest bandwidth of the OFDM signal allows the system to operate in 2.4 GHz and sub-1GHz bands in which the signal penetrates indoor walls better compared to the signal at a higher frequency for UWB systems. We

System	Technology	LOS Accuracy	NLOS Accuracy	Testing Environment Dimension	Tag Power	System Bandwidth	Signal Type	Time per Localization Fix	Energy per Localization
H. Han et al. [43]	65nm ASIC: Real time-sampling	1.9 mm	*N/A*	LOS: < 1m	70 mW @ 1m 320 mW @ 2.1m	500 MHz	Impulse	100 μs	32 μJ @ 2.1m
T. Redant et al. [81]	40nm ASIC: Equivalent time-sampling	4 mm	*N/A*	LOS: 3.6m	195 mW	2 GHz	Multi tones	20 μs	3.9 μJ @ 3.6m
Tang et al. [96]	65nm ASIC: Frequency sweep	4 mm	*N/A*	LOS: < 1m	457 mW	1.7 GHz	Sub-carrier SAR (Phase)	2 μs	0.9 μJ @ <1m
WiTrack [5]	FMCW ToF	31 cm (90%)	40 cm (90%)	LOS: 3-11m NLOS: $6 \times 5m^2$	No tag	1.69 GHz	FMCW	At least 2.5 ms	*N/A*
Harmonium [54]	UWB TDoA	31 cm (90%)	42 cm (90%)	LOS: $4.6 \times 7.2 \times 2.7m^3$ NLOS: $4.6 \times 7.2 \times 2.7m^3$	75 mW	3.5 GHz	Impulse	52 ms	3900 μJ
PolyPoint [55]	UWB ToF (DecaWave chipset)	140 cm (90%)	*N/A*	LOS: $20 \times 20m^2$	150 mW	*N/A*	Impulse	62 ms	9300 μJ
TimeDomain [2]	UWB Two-way ToF	2.1 cm	*N/A*	*N/A*	1.8 W	2.2 GHz	Impulse	6.6 ms	11880 μJ
Ubicarse [57]	SAR + Motion sensor	39 cm (median)	59 cm*** (median)	LOS: $15 \times 10m^2$ NLOS: $15 \times 10m^2$	*N/A*	*N/A*	WiFi	100 ms	*N/A*
PinIt [103]	RFID SAR	16 cm (90%)	16 cm (90%)	LOS: $6 \times 5 \times 2.2m^3$ NLOS: $6 \times 5 \times 2.2m^3$ (200 tags with 15 cm spaced)	Passive	6 MHz (UHF)	UHF RFID	5.4 s****	*N/A*
Tagoram [111]	RFID SAR	12 cm (median)	*N/A*	LOS: $1 \times 2m^2$	Passive	6 MHz (UHF)	UHF RFID	At least 33 ms	*N/A*
WASP [86]	Narrow band ToA	50 cm (85%)	50 cm (65%)	LOS: 10m NLOS: $15 \times 15m^2$	2-2.5 W	125 MHz	OFDM	100 ms	200000 - 250000 μJ
FILA [107]	802.11 RSSI + CSI*	45 cm (median)	180 cm (90%)	LOS: $5 \times 8m^2$ NLOS: $32.5 \times 10m^2$	1.6 W**	80 MHz	OFDM	16 ms	25600 μJ
Chronos [101]	802.11 WiFi + Band-stitching	14.1 cm (median)	20.7 cm (median)	LOS: $20 \times 20m^2$ NLOS: $20 \times 20m^2$	1.6 W**	20MHz $\times$ 35 overlapped ch.	OFDM	84 ms	134400 μJ
RF-Echo	**180nm ASIC: Active reflection + Neural network estimation**	**26 cm (90%)**	**46 cm (90%)**	**LOS:** $7 \times 90m^2$ **NLOS:** $30 \times 20m^2$	**62.8 mW**	**80 MHz**	**OFDM**	**20 μs per symbol**	**18 μJ (Pilot tone + 10 symbols)**

* CSI is Channel State Information on each subcarrier of 802.11 PHY layer
** Calculated based on Intel WiFi Link 5300 in RX mode [42]
*** Calculated based on reported x, y, z error
**** Including computational time

Table 4.1: Comparison of accuracy, dimension of field trial environment, tag power, update rate, and energy consumption per localization for a representative sampling of recently published indoor RF localization systems.

overcome the limitation of low signal bandwidth by using a neural network based ToF estimation technique. Power consumption of the active reflector tag is 62.8 mW. The anchor prototype is implemented on a USRP SDR platform. Field trials conducted in a university campus building confirm that the proposed system can operate up to 85 m distance in LOS scenarios and it can provide <40 cm standard deviation of error for 1D ranging in challenging indoor NLOS scenarios. Accurate multilateration field trail results (26 cm location error in LOS and 46 cm location error in NLOS, 90% CDF) are provided to demonstrate the usability of the proposed system for various applications including indoor navigation, public safety search and rescue operations.

CHAPTER V

Conclusions and Future Directions

5.1 Summary of Contributions

This dissertation focuses on millimeter-scale wireless communication systems and high energy efficiency RF sensing systems, expanding the potential applications of millimeter-scale wireless sensor nodes. It is challenging to develop such tiny form factor wireless systems due to the many physical constraints. In order to tackle these problems, this thesis discusses and analyzes trade-offs and then proposes novel solutions from different perspectives, including antenna-circuit co-design, new transceiver front-end architecture, custom-designed wireless communication protocols, the use of neural network estimation, and so on. The goal of this dissertation is to study the wireless communication and sensing system design trade-offs from every aspect and finally to obtain a holistic optimization.

Chapter II prototypes a 3x3x3 mm^3 crystal-less asymmetric radio system optimized for indoor NLOS communication. This work makes a significant contribution to enabling low-power wireless communication capabilities for ubiquitous IoT sensor nodes. The major contributions of this work include 1) the analysis and design of electrically small magnetic dipole and electric dipole antennas in sub-GHz frequency, especially considering the quality factor of impedance matching; 2) a new design concept and implementation of antenna-transceiver co-optimized architecture; 3) link loss

optimization that includes millimeter-scale antenna efficiency and ITU channel model for NLOS communication; 4) the implementation of a sensor-initiated bi-directional synchronization protocol and interference handling on a gateway device; and 5) system integration design and field trial testing with > 100 meter communication range in open space.

Chapter III proposes a new transceiver architecture with the entire radio system integrated in a 4x4x4 mm^3 form factor, which enables a low-power sensor-to-sensor communication network. The fabricated transceiver chip demonstrates good sensitivity(-94 dBm) with < 100 μW, and the integrated radio system can successfully conduct sensor-to-sensor communication. The major contributions of this work include 1) a new carrier frequency interlocking IF transceiver architecture; 2) the co-design of a millimeter-scale 3D magnetic antenna and reuse of the transceiver front-end; and 3) the use of a low-power system real-time clock to lock the radio frequency power oscillator to reduce the cost and complexity of the system design.

In Chapter IV, a low-complexity, low-cost, and high energy efficiency RF sensing system is demonstrated. This work has great impact by showing a rapid deployable indoor localization system with good accuracy for first responder rescue applications. The custom-designed low-cost ASIC tag proves that using a simplified all-analog design can significantly lower the energy consumption and system design complexity. The major contributions of this work include 1) a new RF localization system that uses active tag reflection, which extends the location distance greatly; 2) a new design aspect of low-cost tag devices; 3) adoption of a neural network time-of-flight estimation scheme that has better ranging accuracy than hand-designed algorithm; and 4) an indoor localization system capable of ranging up to 90 meter with 10s of centimeters error using a single tag as demonstrated by field-trial experiments.

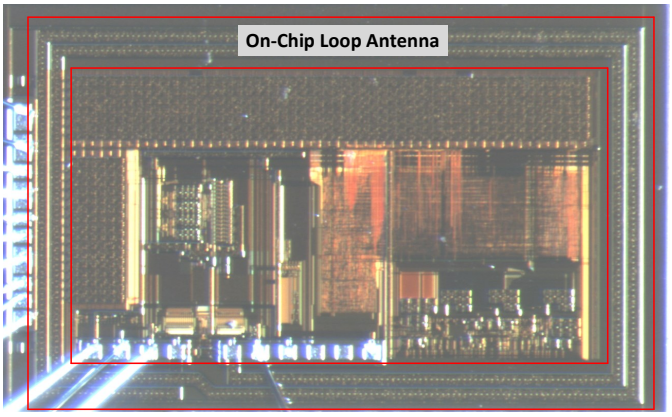


Figure 5.1: RF transceiver with on-chip loop antenna

5.2 Other Works

In Chapter II, we propose a 3D magnetic dipole antenna that is printed on a Rogers material and has a size of 3x3x2 mm^3. Though this dimension is useful in most IoT applications, it is still too large (thick) if we want to use a syringe needle to implant the sensor for some bio-sensing applications [90]. Therefore, we designed an on-chip antenna that can be integrated in silicon and made the entire radio fully on-chip with a dimension of less than 1x2 mm^2 as shown in Figure 5.1. The radio chip will be integrated with other layers including a battery in a cubic millimeter form factor as shown in Figure 5.2.

The radio working principle is similar to the system described in Chapter II. However, the on-chip antenna results in a lower efficiency and quality factor. In addition, there are no off-chip capacitors serving as energy buffers, limiting the radio duty cycle. As a result, the integrated system transmits with short pulses (300-500 ns), which increases the occupied bandwidth and degrades the link distance. The maximum measured distance of this system is approximately 5 centimeters, which is not sufficient if we want to readout multiple sensor nodes.

The major challenge in designing a cubic millimeter radio is the lack of a big capacitor capable of serving as an energy buffer. The on-chip capacitor only has a

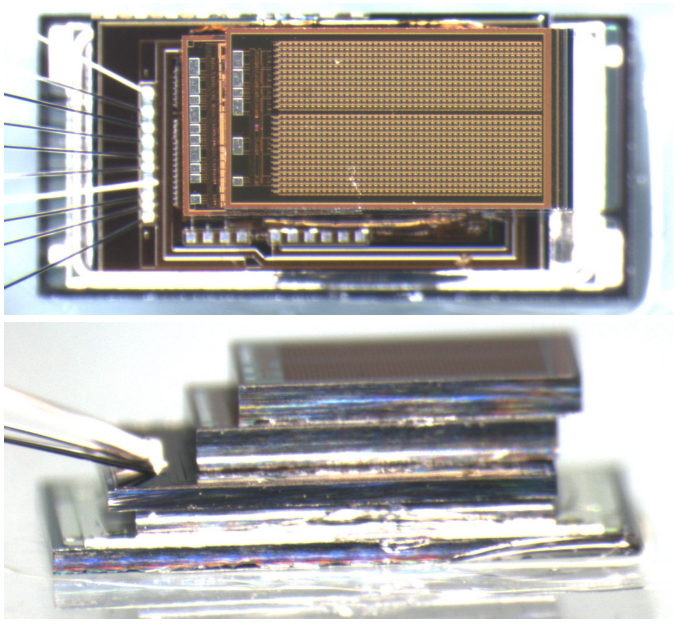


Figure 5.2: Top and side view of the system with radio chip, processor, decap, and mm-scale battery

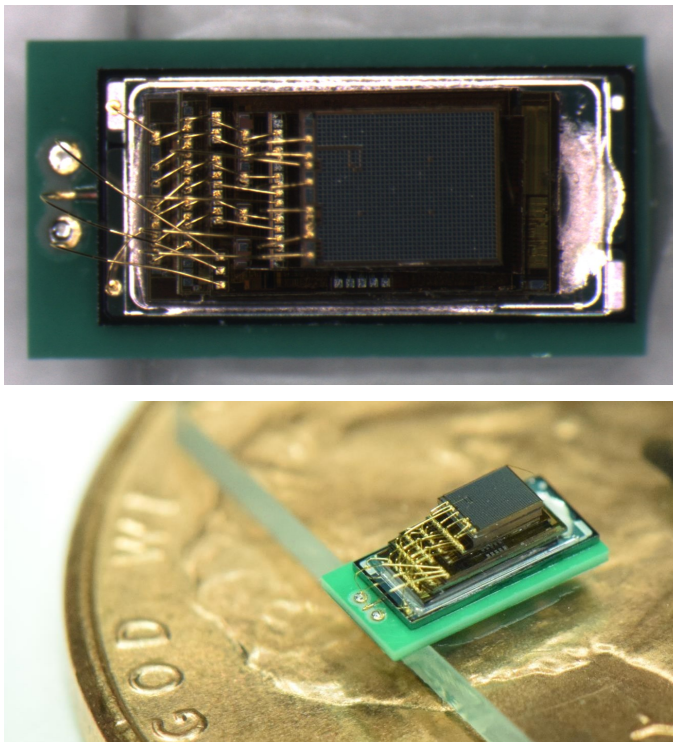


Figure 5.3: Top and side view of the proposed back-scatter system with radio chip, antenna, processor, solar cell, decap, and mm-scale battery

few nF capacity and can only provide energy for < 1 μs. Combining the low transmit energy and poor antenna efficiency, the maximum communication distance is thus limited. To enable a longer link distance while maintaining a small form factor, we proposed using a passive radio instead. There are lots of previous works focused on designing a passive radio using a back-scatter technique[44][53][95], especially in an RFID system. The back-scatter topology is a good candidate in millimeter-scale radio design since the carrier frequency is generated off-chip, and thus the sensor node can avoid high frequency generation, which is very power-hungry. However, the distance of traditional RFID communication systems is usually limited by the capability of delivering power to the radio. In our design, we retain a millimeter-scale battery to avoid this issue and propose a unique symmetrical back-scattering technique. The new system is shown in Figure 5.3. The initial testing has shown a $\sim$2 meter communication distance, which is a substantial improvement from the previous system. This work was led by my colleague Zhen Feng, and I served as a mentor for the initial idea formation, system design, and help in the system testing.

5.3 Future Directions

The work presented in this dissertation opens up more applications of millimeter-scale computing devices by leveraging new design methodology in wireless communication and sensing systems. The impact of this dissertation is significant in the era of the IoT, where devices are connected in daily life. However, many issues remain to be explored and solved in the future.

First, there is still no good wireless communication protocol to support and optimize the sensor-to-sensor mesh communication network, especially when using millimeter-scale low-power (sub-mW) devices as presented in Chapter III. Heavy duty-cycling the sensor node to save power will result in the loss of timing and frequency synchronization. There is some research on the synchronization of wireless

sensor nodes such as the Flooding Time Synchronization Protocol[66] and Gradient Time Synchronization Protocol[91], but those protocols did not consider the millimeter-scale hardware constraints.

Secondly, as presented in Chapter II and Chapter III, the maximum transmit power from a sensor node is less than -10 dBm with the proposed transmitter topology. The proposed transmitter topology will be limited by the VDD value and the antenna design. A better transmitter architecture that has high energy efficiency, and high output power is a potential research area.

Third, it will be interesting to explore the possibility of high-efficiency wireless power transfer or wireless harvesting in millimeter-scale devices. Since solar cells are limited in light intensity and area, they are not good candidates if we want to continue shrinking the system form factor or distribute the wireless sensors in some shadowed area. The existing wireless power transfer and RF harvesting technique suffer from low efficiency, which will cause tremendous energy wastes if they are adopted in the IoT market.

Last but not least, Chapter IV introduces neural network ToF estimation to increase the ranging resolution with limited wireless sensing bandwidth. The ISM bandwidth is very crowded and a precious resource, especially in this IoT era. A better neural network-based ToF estimation enhancement is worth investigating since the neural network-based super resolution algorithm has been widely used and studied in audio/image processing recently[110][19].

BIBLIOGRAPHY

BIBLIOGRAPHY

[1] Bluetooth Core Version 5.0 specification. https://www.bluetooth.com/specifications/bluetooth-core-specification.

[2] Time Domain PulsON 400 RCM. http://www.timedomain.com/p400.php and http://www.timedomain.com/datasheets/TD_DS_P410_RCM_FA.pdf.

[3] Z-Wave. http://www.z-wave.com/.

[4] Zigbee products. http://www.zigbee.org/zigbee-products-2/.

[5] Fadel Adib, Zachary Kabelac, Dina Katabi, and Robert C. Miller. 3d tracking via body radio reflections. In *Proceedings of the 11th USENIX Conference on Networked Systems Design and Implementation*, NSDI'14, pages 317–329, Berkeley, CA, USA, 2014. USENIX Association.

[6] Bryan Atwood, Brett Warneke, and Kristofer SJ Pister. Preliminary circuits for smart dust. In *Proceedings of the 2000 Southwest Symposium on Mixed-Signal Design, San Diego, California*, pages 87–92, 2000.

[7] Luigi Atzori, Antonio Iera, and Giacomo Morabito. The internet of things: A survey. *Computer networks*, 54(15):2787–2805, 2010.

[8] Suyoung Bang, Allan Wang, Bharan Giridhar, David Blaauw, and Dennis Sylvester. A fully integrated successive-approximation switched-capacitor dc-dc converter with 31mv output voltage resolution. In *Solid-State Circuits Conference Digest of Technical Papers (ISSCC), 2013 IEEE International*, pages 370–371. IEEE, 2013.

[9] Gordon Bell. Bell's law for the birth and death of computer classes: A theory of the computer's evolution. *IEEE Solid-State Circuits Society Newsletter*, 13(4):8–19, 2008.

[10] K. Benkic, M. Malajner, P. Planinsic, and Z. Cucej. Using rssi value for distance estimation in wireless sensor networks based on zigbee. In *2008 15th International Conference on Systems, Signals and Image Processing*, pages 303–306, June 2008.

[11] Best and Yaghjian. The lower bounds on q for lossy electric and magnetic dipole antennas. *IEEE Antennas and Wireless Propagation Letters*, 3:314–316, 2004.

[12] Best and Yaghjian. The lower bounds on q for lossy electric and magnetic dipole antennas. *IEEE Antennas and Wireless Propagation Letters*, 3:314–316, 2004.

[13] Dinesh Bharadia, Emily McMilin, and Sachin Katti. Full duplex radios. In *Proceedings of the ACM SIGCOMM 2013 Conference on SIGCOMM*, pages 375–386, New York, NY, USA, 2013. ACM.

[14] J. L. Bohorquez, A. P. Chandrakasan, and J. L. Dawson. A 350 μw cmos msk transmitter and 400 μw ook super-regenerative receiver for medical implant communications. *IEEE Journal of Solid-State Circuits*, 44(4):1248–1259, April 2009.

[15] Boston Consulting Group. The Internet of Things Connects Businesses to the Real World. `https://www.bcg.com/en-us/digital-bcg/internet-of-things.aspx`.

[16] Michael S Brandstein, John E Adcock, and Harvey F Silverman. A closed-form location estimator for use with room environment microphone arrays. *Speech and Audio Processing, IEEE Transactions on*, 5(1):45–50, 1997.

[17] Leo Breiman. Bagging predictors. *Mach. Learn.*, 24(2):123–140, August 1996.

[18] Graham M Brooker. Understanding millimetre wave fmcw radars.

[19] Joan Bruna, Pablo Sprechmann, and Yann LeCun. Super-resolution with deep convolutional sufficient statistics. *CoRR*, abs/1511.05666, 2015.

[20] Ralph Bucher and D Misra. A synthesizable VHDL model of the exact solution for three-dimensional hyperbolic positioning system. *Vlsi Design*, 15(2):507–520, 2002.

[21] YT Chan and KC Ho. A simple and efficient estimator for hyperbolic location. *Signal Processing, IEEE Transactions on*, 42(8):1905–1915, 1994.

[22] Ting Chia Chang, Max L. Wang, Jayant Charthad, Marcus J. Weber, and Amin Arbabian. 27.7 a 30.5mm3 fully packaged implantable device with duplex ultrasonic data and power links achieving 95kb/s with ¡104 ber at 8.5cm depth. *2017 IEEE International Solid-State Circuits Conference (ISSCC)*, pages 460–461, 2017.

[23] J. Charthad, N. Dolatsha, A. Rekhi, and A. Arbabian. System-level analysis of far-field radio frequency power delivery for mm-sized sensor nodes. *IEEE Transactions on Circuits and Systems I: Regular Papers*, 63(2):300–311, Feb 2016.

[24] G. Chen, M. Fojtik, D. Kim, D. Fick, J. Park, M. Seok, M. T. Chen, Z. Foo, D. Sylvester, and D. Blaauw. Millimeter-scale nearly perpetual sensor system with stacked battery and solar cells. In *2010 IEEE International Solid-State Circuits Conference - (ISSCC)*, pages 288–289, Feb 2010.

[25] Gregory Chen, Matthew Fojtik, Daeyeon Kim, David Fick, Junsun Park, Mingoo Seok, Mao-Ter Chen, Zhiyoong Foo, Dennis Sylvester, and David Blaauw. Millimeter-scale nearly perpetual sensor system with stacked battery and solar cells. In *Solid-State Circuits Conference Digest of Technical Papers (ISSCC), 2010 IEEE International*, pages 288–289. IEEE, 2010.

[26] Gregory Chen, Hassan Ghaed, Razi-ul Haque, Michael Wieckowski, Yejoong Kim, Gyouho Kim, David Fick, Daeyeon Kim, Mingoo Seok, Kensall Wise, et al. A cubic-millimeter energy-autonomous wireless intraocular pressure monitor. In *Solid-State Circuits Conference Digest of Technical Papers (ISSCC), 2011 IEEE International*, pages 310–312. IEEE, 2011.

[27] H. C. Chen, T. H. Lin, H. T. Kung, C. K. Lin, and Y. Gwon. Determining rf angle of arrival using cots antenna arrays: A field evaluation. In *MILCOM 2012 - 2012 IEEE Military Communications Conference*, pages 1–6, Oct 2012.

[28] H. S. Chen, H. Y. Tsai, L. X. Chuo, Y. K. Tsai, and L. H. Lu. A 5.2-ghz full-integrated rf front-end by t/r switch, lna, and pa co-design with 3.2-db nf and +25.9-dbm output power. In *2015 IEEE Asian Solid-State Circuits Conference (A-SSCC)*, pages 1–4, Nov 2015.

[29] Y. Chen, N. Chiotellis, L. X. Chuo, C. Pfeiffer, Y. Shi, R. G. Dreslinski, A. Grbic, T. Mudge, D. D. Wentzloff, D. Blaauw, and H. S. Kim. Energy-autonomous wireless communication for millimeter-scale internet-of-things sensor nodes. *IEEE Journal on Selected Areas in Communications*, 34(12):3962–3977, Dec 2016.

[30] M. Choi, T. Jang, S. Bang, Y. Shi, D. Blaauw, and D. Sylvester. A 110 nw resistive frequency locked on-chip oscillator with 34.3 ppm/^{o}c temperature stability for system-on-chip designs. *IEEE Journal of Solid-State Circuits*, 51(9):2106–2118, Sept 2016.

[31] L. X. Chuo, Y. Shi, Z. Luo, N. Chiotellis, Z. Foo, G. Kim, Y. Kim, A. Grbic, D. Wentzloff, H. S. Kim, and D. Blaauw. 7.4 a 915mhz asymmetric radio using q-enhanced amplifier for a fully integrated 3x3x3mm^3 wireless sensor node with 20m non-line-of-sight communication. In *2017 IEEE International Solid-State Circuits Conference (ISSCC)*, pages 132–133, Feb 2017.

[32] Li-Xuan Chuo, Yao Shi, Zhihong Luo, Nikolaos Chiotellis, Zhiyoong Foo, Gyouho Kim, Yejoong Kim, Anthony Grbic, David Wentzloff, Hun-Seok Kim, et al. 7.4 a 915mhz asymmetric radio using q-enhanced amplifier for a fully integrated 3× 3× 3mm 3 wireless sensor node with 20m non-line-of-sight communication. In *Solid-State Circuits Conference (ISSCC), 2017 IEEE International*, pages 132–133. IEEE, 2017.

[33] Federal Communications Commission et al. Understanding the fcc regulations for low-power, non-licensed transmitters. *Office of Engineering and Technology*, 34, 1993.

[34] DecaWave. Application note: APS007. http://www.decawave.com/sites/default/files/resources/aps007_wired_sync_rtls_with_the_dw1000.pdf.

[35] DecaWave. ScenSor DW1000. http://www.decawave.com/.

[36] Ming Ding, Xiaoyan Wang, Peng Zhang, Yuming He, Stefano Traferro, Kenichi Shibata, Minyoung Song, Hannu Korpela, Keisuke Ueda, Yao-Hong Liu, et al. A 0.8 v 0.8 mm 2 bluetooth 5/ble digital-intensive transceiver with a 2.3 mw phase-tracking rx utilizing a hybrid loop filter for interference resilience in 40nm cmos. In *Solid-State Circuits Conference-(ISSCC), 2018 IEEE International*, pages 446–448. IEEE, 2018.

[37] E. Elnahrawy, J. Austen-Francisco, and R. P. Ma. Adding angle of arrival modality to basic rss location management techniques. In *2007 2nd International Symposium on Wireless Pervasive Computing*, Feb 2007.

[38] Dave Evans. The internet of everything. *Cisco Internet Business Solutions Group (TBSG), Cisco Systems, Inc., San Jose, CA, USA, White Paper*, 2012.

[39] Matthew Fojtik, Daeyeon Kim, Gregory Chen, Yu-Shiang Lin, David Fick, Junsun Park, Mingoo Seok, Mao-Ter Chen, Zhiyoong Foo, David Blaauw, et al. A millimeter-scale energy-autonomous sensor system with stacked battery and solar cells. *IEEE Journal of Solid-State Circuits*, 48(3):801–813, 2013.

[40] S. Gezici, Zhi Tian, G. B. Giannakis, H. Kobayashi, A. F. Molisch, H. V. Poor, and Z. Sahinoglu. Localization via ultra-wideband radios: a look at positioning aspects for future sensor networks. *IEEE Signal Processing Magazine*, 22(4):70–84, July 2005.

[41] Ian Goodfellow, Yoshua Bengio, and Aaron Courville. *Deep Learning*. MIT Press, 2016.

[42] Daniel Halperin, Ben Greenstein, Anmol Sheth, and David Wetherall. Demystifying 802.11n power consumption. In *Proceedings of the 2010 International Conference on Power Aware Computing and Systems*, HotPower'10, pages 1–, Berkeley, CA, USA, 2010. USENIX Association.

[43] H. G. Han, B. G. Yu, and T. W. Kim. 19.6 a 1.9mm-precision 20gs/s real-time sampling receiver using time-extension method for indoor localization. In *2015 IEEE International Solid-State Circuits Conference - (ISSCC) Digest of Technical Papers*, pages 1–3, Feb 2015.

[44] Mehrdad Hessar, Ali Najafi, and Shyamnath Gollakota. Netscatter: Enabling large-scale backscatter networks. In *16th USENIX Symposium on Networked Systems Design and Implementation (NSDI 19)*, Boston, MA, 2019. USENIX Association.

[45] John S Ho, Alexander J Yeh, Evgenios Neofytou, Sanghoek Kim, Yuji Tanabe, Bhagat Patlolla, Ramin E Beygui, and Ada SY Poon. Wireless power transfer to deep-tissue microimplants. *Proceedings of the National Academy of Sciences*, 111(22):7974–7979, 2014.

[46] Yoe H. Hwang J., Shin C. Study on an agricultural environment monitoring server system using wireless sensor networks. *Sensors (Basel, Switzerland)*, 10:11189–211, 2010.

[47] ITU. Propagation data and prediction methods for the planning of indoor radiocommunication systems and radio local area networks in the frequency range 300 MHz to 100 GHz. `https://www.itu.int/rec/R-REC-P.1238/en`.

[48] Vikram Iyer, Rajalakshmi Nandakumar, Anran Wang, Sawyer B. Fuller, and Shyamnath Gollakota. Living iot: A flying wireless platform on live insects. In *The 25th Annual International Conference on Mobile Computing and Networking*, MobiCom '19, October 2019.

[49] Seokhyeon Jeong, Yu Chen, Taekwang Jang, Julius Ming-Lin Tsai, David Blaauw, Hun-Seok Kim, and Dennis Sylvester. Always-on 12-nw acoustic sensing and object recognition microsystem for unattended ground sensor nodes. *IEEE Journal of Solid-State Circuits*, 53(1):261–274, 2018.

[50] Wanyeong Jung, Sechang Oh, Suyoung Bang, Yoonmyung Lee, Dennis Sylvester, and David Blaauw. 23.3 a 3nw fully integrated energy harvester based on self-oscillating switched-capacitor dc-dc converter. In *Solid-State Circuits Conference Digest of Technical Papers (ISSCC), 2014 IEEE International*, pages 398–399. IEEE, 2014.

[51] J. Kang, P. Y. Chiang, and A. Natarajan. 21.6 a 1.2cm2 2.4ghz self-oscillating rectifier-antenna achieving 34.5dbm sensitivity for wirelessly powered sensors. In *2016 IEEE International Solid-State Circuits Conference (ISSCC)*, pages 374–375, Jan 2016.

[52] Elliott Kaplan and Christopher Hegarty. *Understanding GPS: principles and applications*. Artech house, 2005.

[53] Bryce Kellogg, Vamsi Talla, Joshua R. Smith, and Shyamnath Gollakot. Passive wi-fi: Bringing low power to wi-fi transmissions. *GetMobile: Mobile Comp. and Comm.*, 20(3):38–41, January 2017.

[54] B. Kempke, P. Pannuto, and P. Dutta. Harmonium: Asymmetric, band-stitched uwb for fast, accurate, and robust indoor localization. In *2016 15th ACM/IEEE International Conference on Information Processing in Sensor Networks (IPSN)*, pages 1–12, April 2016.

[55] Benjamin Kempke, Pat Pannuto, and Prabal Dutta. Polypoint: Guiding indoor quadrotors with ultra-wideband localization. In *Proceedings of the 2Nd International Workshop on Hot Topics in Wireless*, HotWireless '15, pages 16–20, New York, NY, USA, 2015. ACM.

[56] Hyeongseok Kim, Nikolaos Chiotellis, Elnaz Ansari, Muhammad Faisal, Taekwang Jang, Anthony Grbic, Hun-Seok Kim, David Blaauw, and David Wentzloff. A receiver/antenna co-design for a 1.5 mj per fix fully-integrated 10× 10× 6mm 3 gps logger. In *Custom Integrated Circuits Conference (CICC), 2018 IEEE*, pages 1–4. IEEE, 2018.

[57] Swarun Kumar, Stephanie Gil, Dina Katabi, and Daniela Rus. Accurate indoor localization with zero start-up cost. In *Proceedings of the 20th Annual International Conference on Mobile Computing and Networking*, MobiCom '14, pages 483–494, New York, NY, USA, 2014. ACM.

[58] Ye-sheng Kuo, Pat Pannuto, Gyouho Kim, Zhiyoong Foo, Inhee Lee, Ben Kempke, Prabal Dutta, David Blaauw, and Yoonmyung Lee. Mbus: A 17.5 pj/bit/chip portable interconnect bus for millimeter-scale sensor systems with 8 nw standby power. In *Custom Integrated Circuits Conference (CICC), 2014 IEEE Proceedings of the*, pages 1–4. IEEE, 2014.

[59] Rodger Lea. Smart cities: An overview of the technology trends driving smart cities. *IEEE Advancing Technology for Humanity*, 03 2017.

[60] E. A. Lee, B. Hartmann, J. Kubiatowicz, T. Simunic Rosing, J. Wawrzynek, D. Wessel, J. Rabaey, K. Pister, A. Sangiovanni-Vincentelli, S. A. Seshia, D. Blaauw, P. Dutta, K. Fu, C. Guestrin, B. Taskar, R. Jafari, D. Jones, V. Kumar, R. Mangharam, G. J. Pappas, R. M. Murray, and A. Rowe. The swarm at the edge of the cloud. *IEEE Design Test*, 31(3):8–20, June 2014.

[61] Y. Lee, S. Bang, I. Lee, Y. Kim, G. Kim, M. H. Ghaed, P. Pannuto, P. Dutta, D. Sylvester, and D. Blaauw. A modular 1 mm^3 die-stacked sensing platform with low power i^2c inter-die communication and multi-modal energy harvesting. *IEEE Journal of Solid-State Circuits*, 48(1):229–243, Jan 2013.

[62] Yoonmyung Lee, Bharan Giridhar, Zhiyoong Foo, Dennis Sylvester, and David Blaauw. A 660pw multi-stage temperature-compensated timer for ultra-low-power wireless sensor node synchronization. In *Solid-State Circuits Conference Digest of Technical Papers (ISSCC), 2011 IEEE International*, pages 46–48. IEEE, 2011.

[63] Yoonmyung Lee, Gyouho Kim, Suyoung Bang, Yejoong Kim, Inhee Lee, Prabal Dutta, Dennis Sylvester, and David Blaauw. A modular 1mm 3 die-stacked sensing platform with optical communication and multi-modal energy harvesting. In *Solid-State Circuits Conference Digest of Technical Papers (ISSCC), 2012 IEEE International*, pages 402–404. IEEE, 2012.

[64] Z. Li, W. Dehaene, and G. Gielen. A 3-tier uwb-based indoor localization system for ultra-low-power sensor networks. *IEEE Transactions on Wireless Communications*, 8(6):2813–2818, June 2009.

[65] Nadim Maluf. All you wanted to know about batteries but were afraid to ask – 64. on moore's law and snail's law.

[66] Miklós Maróti, Branislav Kusy, Gyula Simon, and Ákos Lédeczi. The flooding time synchronization protocol. In *Proceedings of the 2Nd International Conference on Embedded Networked Sensor Systems*, SenSys '04, pages 39–49, New York, NY, USA, 2004. ACM.

[67] J. Masuch and M. Delgado-Restituto. A 1.1-mw-rx−81.4-dbm sensitivity cmos transceiver for bluetooth low energy. *IEEE Transactions on Microwave Theory and Techniques*, 61(4):1660–1673, April 2013.

[68] Patrick Mercier and Anantha P. Chandrakasan. *Ultra-Low-Power Short-Range Radios*. 01 2015.

[69] Patrick P Mercier, Andrew C Lysaght, Saurav Bandyopadhyay, Anantha P Chandrakasan, and Konstantina M Stankovic. Energy extraction from the biologic battery in the inner ear. *Nature biotechnology*, 30(12):1240, 2012.

[70] D. Micheli, A. Delfini, F. Santoni, F. Volpini, and M. Marchetti. Measurement of electromagnetic field attenuation by building walls in the mobile phone and satellite navigation frequency bands. *IEEE Antennas and Wireless Propagation Letters*, 14:698–702, 2015.

[71] Gordon E. Moore. Cramming more components onto integrated circuits, reprinted from electronics, volume 38, number 8, april 19, 1965, pp.114 ff. *IEEE Solid-State Circuits Newsletter*, 20:33–35, 2006.

[72] Rikky Muller, Hanh-Phuc Le, Wen Li, Peter Ledochowitsch, Simone Gambini, Toni Bjorninen, Aaron Koralek, Jose M Carmena, Michel M Maharbiz, Elad Alon, et al. 24.1 a miniaturized 64-channel 225μw wireless electrocorticographic neural sensor. In *Solid-State Circuits Conference Digest of Technical Papers (ISSCC), 2014 IEEE International*, pages 412–413. IEEE, 2014.

[73] Richard van Nee and Ramjee Prasad. *OFDM for Wireless Multimedia Communications*. Artech House, Inc., Norwood, MA, USA, 1st edition, 2000.

[74] Sechang Oh, Yao Shi, Gyouho Kim, Yejoong Kim, Taewook Kang, Seokhyeon Jeong, Dennis Sylvester, and David Blaauw. A 2.5 nj duty-cycled bridge-to-digital converter integrated in a 13mm 3 pressure-sensing system. In *Solid-State Circuits Conference-(ISSCC), 2018 IEEE International*, pages 328–330. IEEE, 2018.

[75] Rong. P and M. L. Sichitiu. Angle of arrival localization for wireless sensor networks. In *2006 3rd Annual IEEE Communications Society on Sensor and Ad Hoc Communications and Networks*, volume 1, pages 374–382, Sept 2006.

[76] Charalampos Papamanthou, Franco P. Preparata, and Roberto Tamassia. Algorithmic aspects of wireless sensor networks. chapter Algorithms for Location Estimation Based on RSSI Sampling, pages 72–86. Springer-Verlag, Berlin, Heidelberg, 2008.

[77] N. Pletcher, Simone Gambini, and J. M. Rabaey. A 52 μw wake-up receiver with -72 dbm sensitivity using an uncertain-if architecture. *IEEE Journal of Solid-State Circuits*, 44:269–280, 2009.

[78] J. Prummel, M. Papamichail, J. Willms, R. Todi, W. Aartsen, W. Kruiskamp, J. Haanstra, E. Opbroek, S. Rievers, P. Seesink, J. van Gorsel, H. Woering, and C. Smit. A 10 mw bluetooth low-energy transceiver with on-chip matching. *IEEE Journal of Solid-State Circuits*, 50(12):3077–3088, Dec 2015.

[79] Theodore Rappaport. *Wireless Communications: Principles and Practice*. Prentice Hall PTR, Upper Saddle River, NJ, USA, 2nd edition, 2001.

[80] Behzad Razavi. *RF Microelectronics*. Prentice-Hall, Inc., Upper Saddle River, NJ, USA, 1998.

[81] T. Redant, T. Ayhan, N. De Clercq, M. Verhelst, P. Reynaert, and W. Dehaene. 20.1 a 40nm cmos receiver for 60ghz discrete-carrier indoor localization achieving mm-precision at 4m range. In *2014 IEEE International Solid-State Circuits Conference Digest of Technical Papers (ISSCC)*, pages 342–343, Feb 2014.

[82] E. Saberinia and A. H. Tewfik. Enhanced localization in wireless personal area networks. In *Global Telecommunications Conference, 2004. GLOBECOM '04. IEEE*, volume 4, pages 2429–2434 Vol.4, Nov 2004.

[83] K. R. Sadagopan, J. Kang, S. Jain, Y. Ramadass, and A. Natarajan. A 365nw -61.5 dbm sensitivity, 1.875 cm^2 2.4 ghz wake-up receiver with rectifier-antenna co-design for passive gain. In *2017 IEEE Radio Frequency Integrated Circuits Symposium (RFIC)*, pages 180–183, June 2017.

[84] C. Salazar, A. Cathelin, A. Kaiser, and J. Rabaey. A 2.4 ghz interferer-resilient wake-up receiver using a dual-if multi-stage n-path architecture. *IEEE Journal of Solid-State Circuits*, 51(9):2091–2105, Sept 2016.

[85] C. Salazar, A. Kaiser, A. Cathelin, and J. Rabaey. 13.5 a 97dbm-sensitivity interferer-resilient 2.4ghz wake-up receiver using dual-if multi-n-path architecture in 65nm cmos. In *2015 IEEE International Solid-State Circuits Conference - (ISSCC) Digest of Technical Papers*, pages 1–3, Feb 2015.

[86] Thuraiappah Sathyan, David Humphrey, and Mark Hedley. WASP: A system and algorithms for accurate radio localization using low-cost hardware. *IEEE Transactions on Systems, Man, and Cybernetics – Part C*, 41(2), March 2011.

[87] M. Saxena, P. Gupta, and B. N. Jain. Experimental analysis of rssi-based location estimation in wireless sensor networks. In *Communication Systems Software and Middleware and Workshops, 2008. COMSWARE 2008. 3rd International Conference on*, pages 503–510, Jan 2008.

[88] SBX 120 Daughterboard, Ettus Research LLC. . `https://www.ettus.com/product/details/SBX120`.

[89] P Series. Propagation data and prediction methods for the planning of indoor radiocommunication systems and radio local area networks in the frequency range 900 mhz to 100 ghz. *Recommendation ITU-R*, pages 1238–7, 2012.

[90] Y. Shi, M. Choi, Z. Li, Z. Luo, G. Kim, Z. Foo, H. S. Kim, D. D. Wentzloff, and D. Blaauw. A 10 mm^3 inductive coupling radio for syringe-implantable smart sensor nodes. *IEEE Journal of Solid-State Circuits*, 51(11):2570–2583, Nov 2016.

[91] P. Sommer and R. Wattenhofer. Gradient clock synchronization in wireless sensor networks. In *2009 International Conference on Information Processing in Sensor Networks*, pages 37–48, April 2009.

[92] A. G. Stove. Linear fmcw radar techniques. *IEE Proceedings F - Radar and Signal Processing*, 139(5):343–350, Oct 1992.

[93] M. Tabesh, N. Dolatsha, A. Arbabian, and A. M. Niknejad. A power-harvesting pad-less millimeter-sized radio. *IEEE Journal of Solid-State Circuits*, 50(4):962–977, April 2015.

[94] Maryam Tabesh, Nemat Dolatsha, Amin Arbabian, and Ali M Niknejad. A power-harvesting pad-less millimeter-sized radio. *IEEE Journal of Solid-State Circuits*, 50(4):962–977, 2015.

[95] Vamsi Talla, Mehrdad Hessar, Bryce Kellogg, Ali Najafi, Joshua R. Smith, and Shyamnath Gollakota. Lora backscatter: Enabling the vision of ubiquitous connectivity. *Proc. ACM Interact. Mob. Wearable Ubiquitous Technol.*, 1(3):105:1–105:24, September 2017.

[96] A. Tang, G. Virbila, D. Murphy, F. Hsiao, Y. H. Wang, Q. J. Gu, Z. Xu, Y. Wu, M. Zhu, and M. C. F. Chang. A 144ghz 0.76cm-resolution sub-carrier sar phase radar for 3d imaging in 65nm cmos. In *2012 IEEE International Solid-State Circuits Conference*, pages 264–266, Feb 2012.

[97] Langdon S.L. Murphy K.L. Walton W.A. Taylor C.D., Gutierrez S.J. Measurement of rf propagation into concrete structures over the frequency range

100 mhz to 3 ghz. In *Wireless Personal Communications*, volume 377, pages 131–144, 1997.

[98] A. S. Teran, J. Wong, W. Lim, G. Kim, Y. Lee, D. Blaauw, and J. D. Phillips. Algaas photovoltaics for indoor energy harvesting in mm-scale wireless sensor nodes. *IEEE Transactions on Electron Devices*, 62(7):2170–2175, July 2015.

[99] Derek Z Thai, Matthew Trinkle, Ahmad Hashemi-Sakhtsari, and Tim Pattison. Speaker localisation using time difference of arrival. Technical report, DTIC Document, 2008.

[100] Universal Software Radio Peripheral (USRP), Ettus Research LLC. `https://www.ettus.com/product/`.

[101] Deepak Vasisht, Swarun Kumar, and Dina Katabi. Decimeter-level localization with a single wifi access point. In *13th USENIX Symposium on Networked Systems Design and Implementation (NSDI 16)*, pages 165–178, Santa Clara, CA, 2016. USENIX Assoc.

[102] M. Verhelst, N. Van Helleputte, G. Gielen, and W. Dehaene. A reconfigurable, 0.13um cmos 110pj/pulse, fully integrated ir-uwb receiver for communication and sub-cm ranging. In *2009 IEEE International Solid-State Circuits Conference - Digest of Technical Papers*, pages 250–251,251a, Feb 2009.

[103] Jue Wang and Dina Katabi. Dude, where's my card?: Rfid positioning that works with multipath and non-line of sight. In *Proceedings of the ACM SIGCOMM 2013 Conference on SIGCOMM*, pages 51–62, New York, NY, USA, 2013. ACM.

[104] Brett Warneke, Matt Last, Brian Liebowitz, and Kristofer SJ Pister. Smart dust: Communicating with a cubic-millimeter computer. *Computer*, 34(1):44–51, 2001.

[105] Brett A Warneke and Kristofer SJ Pister. An ultra-low energy microcontroller for smart dust wireless sensor networks. In *Solid-State Circuits Conference, 2004. Digest of Technical Papers. ISSCC. 2004 IEEE International*, pages 316–317. IEEE, 2004.

[106] Wolfgang Arden and Michel Brillout and Patrick Cogez and Mart Graef and Bert Huizing and Reinhard Mahnkopf. More-than-Moore white paper. `http://www.itrs2.net/uploads/4/9/7/7/49775221/irc-itrs-mtm-v2_3.pdf`.

[107] K. Wu, Jiang Xiao, Youwen Yi, Min Gao, and L. M. Ni. Fila: Fine-grained indoor localization. In *2012 Proceedings IEEE INFOCOM*, pages 2210–2218, March 2012.

[108] Xiao Wu, Yao Shi, Supreet Jeloka, Kaiyuan Yang, Inhee Lee, Yoonmyung Lee, Dennis Sylvester, and David Blaauw. A 20-pw discontinuous switched-capacitor

energy harvester for smart sensor applications. *IEEE Journal of Solid-State Circuits*, 52(4):972–984, 2017.

[109] Jie Xiong and Kyle Jamieson. Arraytrack: A fine-grained indoor location system. In *Proceedings of the 10th USENIX Conference on Networked Systems Design and Implementation*, nsdi'13, pages 71–84, Berkeley, CA, USA, 2013. USENIX Association.

[110] J. Yang, J. Wright, T. S. Huang, and Y. Ma. Image super-resolution via sparse representation. *IEEE Transactions on Image Processing*, 19(11):2861–2873, Nov 2010.

[111] Lei Yang, Yekui Chen, Xiang-Yang Li, Chaowei Xiao, Mo Li, and Yunhao Liu. Tagoram: Real-time tracking of mobile rfid tags to high precision using cots devices. In *Proceedings of the 20th Annual International Conference on Mobile Computing and Networking*, MobiCom '14, pages 237–248, New York, NY, USA, 2014. ACM.

[112] Min-Shueh Yuan, Chao-Chieh Li, Chia-Chun Liao, Yu-Tso Lin, Chih-Hsien Chang, and Robert Bogdan Staszewski. A 0.45v sub-mw all-digital pll in 16nm finfet for bluetooth low-energy (ble) modulation and instantaneous channel hopping using 32.768khz reference. *2018 IEEE International Solid - State Circuits Conference - (ISSCC)*, pages 448–450, 2018.

[113] Giovanni Zanca, Francesco Zorzi, Andrea Zanella, and Michele Zorzi. Experimental comparison of rssi-based localization algorithms for indoor wireless sensor networks. In *Proceedings of the Workshop on Real-world Wireless Sensor Networks*, REALWSN '08, pages 1–5, New York, NY, USA, 2008. ACM.

[114] Y. Zheng, M. A. Arasu, K. W. Wong, Y. J. The, A. P. H. Suan, D. D. Tran, W. G. Yeoh, and D. L. Kwong. A 0.18um cmos 802.15.4a uwb transceiver for communication and localization. In *2008 IEEE International Solid-State Circuits Conference - Digest of Technical Papers*, pages 118–600, Feb 2008.